



City Research Online

City, University of London Institutional Repository

Citation: Cavaglià, A. (2015). Nonsemilinear one-dimensional PDEs: analysis of PT deformed models and numerical study of compactons. (Doctoral thesis, City University London)

This is the accepted version of the paper.

This version of the publication may differ from the final published version.

Permanent repository link: <https://openaccess.city.ac.uk/id/eprint/13074/>

Link to published version:

Copyright: City Research Online aims to make research outputs of City, University of London available to a wider audience. Copyright and Moral Rights remain with the author(s) and/or copyright holders. URLs from City Research Online may be freely distributed and linked to.

Reuse: Copies of full items can be used for personal research or study, educational, or not-for-profit purposes without prior permission or charge. Provided that the authors, title and full bibliographic details are credited, a hyperlink and/or URL is given for the original metadata page and the content is not changed in any way.

City Research Online:

<http://openaccess.city.ac.uk/>

publications@city.ac.uk

Nonsemilinear one-dimensional PDEs: analysis of \mathcal{PT} deformed models and numerical study of compactons

Andrea Cavaglià

Department of Mathematics

School of Mathematics, Computer Science and Engineering

City University London

A thesis submitted for the degree of

Doctor of Philosophy in Mathematical Physics

January 2015

Declaration

The work presented in this thesis is based on investigations believed to be original and carried out mainly at the Centre for Mathematical Science, City University London while in candidature for a research degree. A large part of this work was made in collaboration with Prof. Andreas Fring. This work has not been presented elsewhere for a degree, diploma, or similar qualification at any university or similar institution. I have clearly stated my contributions, in jointly-authored works, as well as referenced the contributions of others to the best of my knowledge. Powers of discretion are granted to the University Librarian to allow the thesis to be copied in whole or in part without further reference to the author. This permission covers only single copies made for study purposes, subject to normal conditions of acknowledgement.

Acknowledgements

First of all, I would like to thank my supervisor Andreas Fring for introducing me to the topics of this research, for collaboration on the papers discussed in this Thesis and for giving me constant advice and encouragement throughout these years. I thank City University for a Research Fellowship, and all members of the Mathematics Department for their kindness and professionalism. I am grateful to the examiners of my thesis, Vincent Caudrelier and Andy Hone, for their very insightful suggestions, and for being particularly kind in arranging an early date for the exam. It is a pleasure to remember my fellow students during these years. In particular, thanks to Yogi Valani whose advice was really precious for the design of the code used for the numerical studies presented in the thesis, and to Cheng Zhang, Emanuele Levi, Sanjib Dey, and Zoe Gumm for all our innumerable discussions which have certainly influenced my work. Thanks to Roberto Tateo for all his important encouragement. Finally, thanks to my brother Giovanni and to my parents for their love and support.

Abstract

This thesis is based on the work done during my PhD studies and is roughly divided in two independent parts. The first part consists of Chapters 1 and 2 and is based on the two papers Cavaglià *et al.* [2011] and Cavaglià & Fring [2012], concerning the complex \mathcal{PT} -symmetric deformations of the KdV equation and of the inviscid Burgers equation, respectively. The second part of the thesis, comprising Chapters 3 and 4, contains a review and original numerical studies on the properties of certain quasilinear dispersive PDEs in one dimension with compacton solutions.

The subjects treated in the two parts of this work are quite different, however a common theme, emphasised in the title of the thesis, is the occurrence of nonsemilinear PDEs. Such equations are characterised by the fact that the highest derivative enters the equation in a nonlinear fashion, and arise in the modeling of strongly nonlinear natural phenomena such as the breaking of waves, the formation of shocks and crests or the creation of liquid drops. Typically, nonsemilinear equations are associated to the development of singularities and non-analytic solutions.

Many of the complex deformations considered in the first two chapters are nonsemilinear as a result of the \mathcal{PT} deformation. This is also a crucial feature of the compacton-supporting equations considered in the second part of this work.

This thesis is organized as follows.

Chapter 1 contains an introduction to the field of \mathcal{PT} -symmetric quantum and classical mechanics, motivating the study of \mathcal{PT} -symmetric

deformations of classical systems. Then, we review the contents of Cavaglià *et al.* [2011] where we explore travelling waves in two family of complex models obtained as \mathcal{PT} -symmetric deformations of the KdV equation. We also illustrate with many examples the connection between the periodicity of orbits and their invariance under \mathcal{PT} -symmetry.

Chapter 2 is based on the paper Cavaglià & Fring [2012] on the \mathcal{PT} -symmetric deformation of the inviscid Burgers equation introduced in Bender & Feinberg [2008]. The main original contribution of this chapter is to characterise precisely how the deformation affects the gradient catastrophe. We also point out some incorrect conclusions of the paper Bender & Feinberg [2008].

Chapter 3 contains a review on the properties of nonsemilinear dispersive PDEs in one space dimension, concentrating on the compacton solutions discovered in Rosenau & Hyman [1993]. After an introduction, we present some original numerical studies on the K(2, 2) and K(4, 4) equations. The emphasis is on illustrating the different type of phenomena exhibited by the solutions to these models. These numerical experiments confirm previous results on the properties of compacton-compacton collisions. Besides, we make some original observations, showing the development of a singularity in an initially smooth solution.

In **Chapter 4**, we consider an integrable compacton equation introduced by Rosenau in Rosenau [1996]. This equation has been previously studied numerically in an unpublished work by Hyman and Rosenau cited in Rosenau [2006]. We present an independent numerical study, confirming the claim of Rosenau [2006] that travelling compacton equations to this equation do not contribute to the initial value problem. Besides, we analyse the local conservation laws of this equation and show that most of them are violated by any solution having a compact, dynamically evolving support. We confirm numer-

ically that such solutions, which had not been described before, do indeed exist.

Finally, in **Chapter 5** we present our conclusions and discuss open problems related to this work.

Contents

Contents	vi
List of Figures	ix
1 \mathcal{PT}-symmetric deformations of nonlinear wave equations	1
1.1 Complex extensions of dynamical systems	1
1.2 A brief introduction to \mathcal{PT} -symmetric quantum mechanics	2
1.2.1 Physical applications	5
1.2.2 Comparison of quantum/classical behaviour	6
1.2.3 \mathcal{PT} symmetric deformations of nonlinear wave equations	8
1.3 The KdV equation: complex extension of travelling waves and \mathcal{PT} -symmetric deformations	9
1.3.1 The KdV equation and its \mathcal{PT} -symmetric deformations	9
1.3.2 Complex extension of travelling waves	13
1.3.3 The undeformed equation	16
1.3.3.1 Rational solutions	16
1.3.3.2 Trigonometric solutions	17
1.3.3.3 Elliptic solutions	23
1.3.4 Deformations of the KdV equation I: the \mathcal{PT}_+ -symmetric deformation	26
1.3.4.1 Rational solutions	29
1.3.4.2 Trigonometric solutions	31
1.3.4.3 Elliptic solutions	35
1.3.5 Deformations of the KdV equation II: the \mathcal{PT}_- -symmetric deformation	36

1.3.5.1	An example with $\epsilon = 4$	37
1.4	Complex deformations of soliton solutions	39
1.5	Summary of the results of this chapter	41
2	\mathcal{PT}-symmetric deformation of the inviscid Burgers equation	43
2.1	The undeformed case	44
2.1.1	Inviscid Burgers equation, characteristics and gradient catastrophe	44
2.1.2	Singularities as branch points	45
2.1.3	Shocks and weak solutions	48
2.2	Deformed case ($\epsilon > 1$)	49
2.2.1	Singularities	50
2.3	Summary of the results of this chapter	60
3	Numerical study of the Rosenau-Hyman compacton equations	61
3.1	Solutions with compact support in degenerate equations	62
3.2	The porous medium equation	63
3.2.0.1	Heuristic derivation of the edge equation	66
3.3	The equations of Rosenau and Hyman and compactons	68
3.3.1	Compacton solutions	69
3.3.1.1	Compactons as weak solutions	70
3.3.2	Interactions of compactons	73
3.3.2.1	Other general properties	75
3.4	Numerical study of the $K(2, 2)$ and $K(4, 4)$ equations	77
3.4.1	General description of the numerical method	78
3.4.2	Numerical experiments: the $K(2, 2)$ equation	80
3.4.3	Numerical experiments: the $K(4, 4)$ equation	89
3.5	Summary of the results of this chapter	94
4	Numerical study of stability for an integrable compacton equation	97
4.1	Integrable quasi-linear equations, hodograph transformations and the Lagrange map	98
4.2	An asymptotically stationary compacton equation	103

4.2.1	Special solutions	105
4.2.2	A heuristic argument for the instability of travelling compactons	108
4.2.2.1	A family of deformations	109
4.2.3	Conservation laws and behaviour at the edge of the support	111
4.3	Numerical study	116
4.3.1	Decomposition of positive initial data	117
4.3.2	Comparison with other equations with $\delta \neq 0$	121
4.4	Summary of the results of this chapter	123
5	Conclusions	126
A	Classification of two-dimensional stationary points	129
B	Details on the numerical schemes used to integrate compacton equations	131
C	Study of the compactly-supported travelling solutions of the equations (4.27)	135
C.1	Case $v > 0$	136
C.2	Case $v < 0$	140
References		143

List of Figures

1.1	The first excited energy levels of the Hamiltonians (1.2) as a function of the deformation parameter, where $N := \epsilon + 2$. The plot is taken from Bender & Boettcher [1998].	3
1.2	Complex rational solutions of the KdV equation: in the left panel \mathcal{PT} -symmetric solutions for $c = 1$, $\beta = 2$, $\gamma = 3$ and $A = 1/2$; in the right panel, we have taken $c = 1$, $\beta = 2 + i2$, $\gamma = 3$ and consequently $A = (1 - i)/4$	17
1.3	Left panel: \mathcal{PT}_+ -symmetric solitary wave solutions of the KdV equation with $c = 1$, $\beta = 3/10$, $\gamma = -3$, $A = 4$ and $B = 2$. Right panel: complex periodic \mathcal{PT}_+ -symmetric solutions of the KdV equation with $c = 1$, $\beta = 3/10$, $\gamma = 3$, $A = 4$, $B = 2$. The period is $T = 2\sqrt{15}\pi$	20
1.4	Complex trigonometric solutions of the KdV equation with “spontaneously broken” \mathcal{PT} -symmetry. $c = 1$, $\beta = 3/10$, $\gamma = 3$, $A = 4 + i/2$ and $B = 2 - i$, meaning that this family of orbits break the \mathcal{PT}_+ -symmetry of the equation. All orbits of this type are in the present case open.	21
1.5	Detail of a trigonometric solution of the complexified KdV equation with broken \mathcal{PT} -symmetry. Here we have taken $c = 1$, $\beta = 3/10$, $\gamma = 3 + i/2$, $A = 4$, $B = 2$. The point $u = 4$ behaves like a <i>focus</i> . This solution is characterised by $\text{Im}(\zeta_0) = 6$	22

1.6	Two solutions of the non \mathcal{PT} -symmetric complex KdV equation, where the parameters have been finely tuned in order to obtain a solitary wave solution (left panel), or a periodic solution (right panel). The choice of parameters is: Left: $c = 1, \beta = (16 - 4i)/17, \gamma = -3, A = 4 + i, B = -5 - 5/4i$; Right: $c = 1, \beta = (-8 + 2i)/17, \gamma = -3$ and $A = 4 + i, B = -14 - 7/2i$	23
1.7	\mathcal{PT} -symmetric complex elliptic solutions of the KdV equation with $A = 1, B = 3, C = 6, c = 1, \beta = 3/10, \gamma = -3$ for different values of $\text{Im}\zeta_0$	24
1.8	Spontaneously broken \mathcal{PT} -symmetric complex elliptic solution of the KdV equation for $\text{Im}\zeta_0 = 6$ with $A = 4, B = 5 - i/2, C = 1 + i/2, c = 1, \beta = 3/10$ and $\gamma = 3$. The left panel shows the trajectory for $-64 \leq \zeta \leq 18$ solid (red) and $18 < \zeta \leq 200$ dashed (black). In the right panel: $-200 < \zeta < 1400$. Notice that this is a single, space-filling trajectory.	25
1.9	Broken \mathcal{PT} -symmetric complex elliptic solutions of the KdV equation for $\text{Im}\zeta_0 = 6$: in the left panel, $A = 1, B = 3, C = 6, c = 1, \beta = 3/10$ and $\gamma = 3 + 2i$ for $-200 \leq \zeta \leq 200$; in the right panel, $A = 1, B = 2 + 3i, C = 6, c = 1, \beta = 3/10 - i/10$ and $\gamma = 3$ for $-200 \leq \zeta \leq 200$	26
1.10	Complex \mathcal{PT} -symmetric rational solutions of the deformed KdV equation with $c = 1, \beta = 2$ and $\gamma = 3$ for the deformed model $\mathcal{H}_{-1/2}^+$, corresponding to the behaviour (1.54) with $k = 1/2$ and $\alpha = 6$	28
1.11	Complex \mathcal{PT} -symmetric rational solutions of the deformed KdV equation with $c = 1, \beta = 2$ and $\gamma = 3$ for \mathcal{H}_{-3}^+ , corresponding to the behaviour (1.54) with $k = 1/2$ and $\alpha = -3/2$	29

- 1.12 Contour plot showing different \mathcal{PT} -symmetric rational solutions of the $\mathcal{H}_{1/3}^+$ equation, with $c = 1$, $\beta = 2$ and $\gamma = 3$, corresponding to equation (1.54) with $k = 1/2$ and $\alpha = 9/4$. The system is defined on a four-sheet covering of the complex u -plane: in the left and right panel, we show the shape of orbits on the first two sheets. On the remaining two sheets, the picture would be the same, with the orbits being travelled in the opposite direction. 30
- 1.13 In the left panel are shown four different orbits (all of them characterised by $\text{Im}(\zeta_0) = 1$) of the \mathcal{H}_6^+ model with $c = 1$, $\beta = 2$ and $\gamma = 3$, corresponding to (1.54) with $k = 1/2$ and $\alpha = 3/7$. Each orbit makes a turn around the point $u = A$ and is deflected by an angle which approaches asymptotically $\frac{7}{4}\pi$. Notice that these four orbits live on different Riemann sheets, so that there are no intersections. In the right panel, we break \mathcal{PT} -symmetry by taking $c = 1$, $\beta = 2 + 2i$ and $\gamma = 3$, leading to $k = 1/4(1 - i)$, and the same value of α . Clearly this simply amounts to a rotation. 31
- 1.14 The network of separatrix curves for different solutions of the $\mathcal{H}_{\frac{1}{2}}^+$ model for $c = 1$, $\beta = 3/10$, $\gamma = 3$. The critical points A and B are chosen as: (*top left*) $A = 4$, $B = 2$; (*top right*): $A = 4 + \frac{i}{200000}$, $B = 2 - \frac{i}{100000}$; (*bottom left*): $A = 4 + \frac{i}{50}$, $B = 2 - \frac{i}{25}$; (*bottom right*): $A = 4 + i$, $B = 2 - 2i$. Notice that the topology of the network corresponding to the first solution (the \mathcal{PT} -symmetric case) differs from the other three and does not allow the existence of orbits connecting A and B 33
- 1.15 Complex \mathcal{PT} -symmetric trigonometric/hyperbolic solutions of the deformed KdV equation with $A = 4, B = 2, c = 1, \beta = 2$ and $\gamma = 3$ for $\mathcal{H}_{-1/2}^+$ 34
- 1.16 Trigonometric/hyperbolic solutions of the deformed KdV equation $\mathcal{H}_{-1/2}^+$ with spontaneously broken \mathcal{PT} -symmetry. The relevant parameters are: $A = 4 + i, B = 2 - 2i, c = 1, \beta = 3/10$ and $\gamma = 3$. 34

1.17 Complex \mathcal{PT} -symmetric trigonometric/hyperbolic solutions of the \mathcal{H}_{-2}^+ deformation with $c = 1$, $\beta = 2$ and $\gamma = 3$. In the left panel, the solution is symmetric with $A = 4$, $B = 2$. In the right panel, it is spontaneously broken, with $A = 4 + i/2$, $B = 2 - i$	35
1.18 \mathcal{PT} -symmetric solutions for \mathcal{H}_4^- : (a) Star node at the origin for $c = 1$, $\beta = 2$, $\gamma = 1$; (b) centre at the origin for $c = 1$, $\beta = 1$, $\gamma = -1$. In both cases there are four turning points at $u = \pm B$, $\pm iB$, with $B = (15/2)^{1/4}$	37
1.19 Broken \mathcal{PT} -symmetry for the \mathcal{H}_4^- model: these solutions spiral around a focus at $u = 0$, accompanied by four turning points at $u = \pm B$, $\pm iB$, with $B = (15/2)^{1/4}$. The parameters were chosen as $c = 1$, $\beta = 2$, $\gamma = 1 + i3$	38
1.20 Complex spontaneously broken one-soliton solution of the KdV-equation with $\beta = 6$, $\gamma = 1 + i/2$, $p_1 = 2$, $\phi = i0.8$ and $\Delta_t = -\pi/2$ for different times $t = -\pi/2$ solid (blue), $t = -1$ dashed (red), $t = 0$ dasheddot (orange), $t = 0.7$ dotted (green), and $t = \pi/2$ dasheddotdot (black).	40
1.21 \mathcal{PT} -symmetric two-soliton solutions of the KdV equation for $\beta = 6$, $\gamma = 1$, $p_1 = 1.2$, $p_2 = 2.2$, $\phi_1 = i0.1$ and $\phi_2 = i0.2$. Left panel: $t = -2$ solid (blue), $t = -0.2$ dashed (red), $t = 0.2$ dotted (black); right panel: $t = 0.3$ dotted (black), $t = 0.8$ dashed (red), $t = 2.0$ solid (blue).	41
1.22 Broken \mathcal{PT} -symmetric two-soliton solutions of the KdV equation for $\beta = 6$, $\gamma = 1 + i\pi/8$, $p = 2(2/3)^{1/3}$, $p_2 = 2$, $\phi_1 = i0.1$ and $\phi_2 = i0.2$. Left panel: $t = -4$ solid (blue), $t = -3.5$ dashed (red), $t = -2$ dotted (black); right panel: $t = 0.7$ solid (blue), $t = 2$ dashed (red), $t = 8$ dotted (black). Notice that for this choice of parameters we have $2\Delta_t^1 = 3\Delta_t^2 = 6$. We see that both solitons have almost regained their original shape passing from $t = 2$ to $t = 8$, but for a slight discrepancy due to the well known time delay occurring in soliton scattering.	41

- 2.1 Snapshots of the solution $w(x, t)$ to the inviscid Burgers equation with initial condition $w(x, 0) = \frac{1}{1+x^2}$. The solid lines correspond to $t = 0$, $t = 0.8$ and $t = t_s = \frac{8}{3\sqrt{3}} \simeq 1.5396$ (the crest of the wave moves rightwards for increasing times). The dotted multi-valued profile corresponds to $t = t_s + 1$ 46
- 2.2 Trajectories traced in the complex x -plane by the square root branch points of the solution of (2.1) with initial condition $w(x, 0) = \frac{1}{1+x^2}$. There are four distinct trajectories, all traced for t in the interval $t \in [0.0001, 1.75]$. We observe that two singularities emerge from each of the two poles $x = \pm i$ at $t = 0^+$. One pair of complex conjugate singularities moves off in the in the complex plane, while the other two singularities reach the real axis simultaneously at $t = t_s = \frac{8}{3\sqrt{3}}$. They remain confined to the real axis for $t > t_s$. 47
- 2.3 In the left panel, trajectories traced in the complex x -plane by the square-root branch points of the $\epsilon = 2$ solution with $u_0(x) = \frac{1}{1+x^2}$. In the right panel, we consider the $\epsilon = 2.2$ deformation with the same initial condition (in this case, we are showing only some of the singularities, the ones corresponding to the principal branch in the definition of $W_0^{(\epsilon)}$). In both plots the trajectories are shown for $t \in [10^{-6}, 0.36]$; the arrow of time is such that the square-root branch points move out of the poles at $x = \pm i$ as t increases from $t = 0^+$ 52
- 2.4 Trajectories of square root branch points in the complex x -plane, for the $\epsilon = 3$ (left) and $\epsilon = 5$ deformation (right), where the initial condition was chosen again as $u_0(x) = \frac{1}{1+x^2}$. In both plots the trajectories correspond to $t \in [10^{-6}, 0.4]$, and move out of the poles at $x = \pm i$ as time progresses. One can see that, since the solution is real, singularities arrive on the real axis in pairs and afterwards remain confined there. 53

- 2.5 *Left panel:* space-time plot of (2.1) with initial condition $w_0(x) = W_0^{(3)}(x)$ defined by (2.17) with $\epsilon = 3$, $u_0(x) = \frac{1}{1+x^2}$, for $0 < t < t_s$. *Right panel:* the corresponding solution of the $\epsilon = 3$ -deformed model, in the same time interval. One can see that, as $t \rightarrow t_s^-$, $w_x^{(\epsilon)} \rightarrow \infty$, while for u this appears as $u_{xx} \rightarrow \infty$ 54
- 2.6 Left: solution of the $\epsilon = 2$ -deformed inviscid Burgers equation for $u_0(x) = \frac{1}{1+x^2}$ at times $t = 0$ (blue, dashed), $t = 0.1$ (purple, dotted) and at the singularity time $t = t_s \sim 0.191$ (red, solid). Right: solution of the $\epsilon = 5/2$ -model with the same initial condition, shown for $t = 0$ (blue, dashed), $t = 0.1$ (purple, dotted) and $t = t_s \sim 0.176$ (red, solid). The black dots mark the places where $u_{xx} \rightarrow \infty$ 55
- 2.7 Left: solution of the $\epsilon = 3$ -model with $u_0(x) = \frac{1}{1+x^2}$, shown for $t = 0$ (blue, dashed), $t = 0.1$ (purple, dotted) and $t = t_s \sim 0.312$ (red, solid). Right: solution of the $\epsilon = 5$ -model with the same initial condition, shown for $t = 0$ (blue, dashed), $t = 0.1$ (purple, dotted) and $t = t_s \sim 0.395$ (red, solid). The black dots mark the places where $u_{xx} \rightarrow \infty$ 55
- 2.8 Solution of the $\epsilon = 3$ equation with $u_0(x) = \frac{1}{1+x^2}$ at the time of appearance of the second singularity $t = t_{s,2} \sim 0.64 > t_{s,1} \sim 0.31$. The vertical line marks the location $x_{s,2} \sim -1.2$. Notice that, around $x_{s,1} \sim 0.08$, the solution has branched into a multi-valued profile with a self-intersection. 57
- 2.9 These two figures illustrate the mechanism of formation of a self-crossing profile in real solutions of the deformed equation after the breaking time. A multivalued profile of the undeformed equation (*left*) is transformed into a self-intersecting profile for $\tilde{u} = iu^{\frac{\epsilon}{\epsilon-1}}$ (*right*) according to (2.28). The vertical line in the left plot preserves the area shaded by the graph of $\tilde{w} = (w^{(\epsilon)}(x,t))^{\frac{1}{\epsilon-1}}$. It corresponds to a self-intersection for the graph of \tilde{u} since $0 = \left(\int_{s_1}^{s_2} - \int_{s_2}^{s_3} + \int_{s_3}^{s_4} \right) \tilde{w}(x(s), t) \left| \frac{dx}{ds} \right| ds = \tilde{u}(x(s_4), t) - \tilde{u}(x(s_1), t)$ 58

LIST OF FIGURES

2.10	Snapshots of the solution of the $\epsilon = 3$ deformation with initial condition $u(x, 0) = \frac{x}{1+x^2}$, shown at time $t = 0$ (red, dotted), $t = 1.5$ (blue, dashed) and $t = t_{\text{shock}} = \frac{1}{3}$ (solid, black).	59
3.1	The Barenblatt solution (3.7) of the porous medium equation with $m = 3$, with the parameter choice $\beta = 1$, shown at times $t = 1$, $t = 2$, $t = 3$, $t = 4$, $t = 5$. The support of the solution spreads as time increases.	64
3.2	The shapes of compacton solutions to the K(2, 2) equation (blue, dotted), to the K(3, 3) equation (purple, dashed), and to the K(4, 4) equation (black, solid). In all cases we took $c = 1$. The behaviour of these three solutions close to the endpoints e_{\pm} of the support is $u_{2,2} \sim x - e_{\pm} ^2$, $u_{3,3} \sim x - e_{\pm} $, and $u_{4,4} \sim x - e_{\pm} ^{\frac{2}{3}}$, respectively.	71
3.3	Numerical solution of the K(2, 2) equation showing the scattering among two compactons of speeds $c_1 = 1$ and $c_2 = 3$. This simulation was performed with $\eta_2 = 0$ and $\eta_4 = 10^{-3}$	81
3.4	Detail of the ripple left by the collision of two compactons, for the same data shown in Figure 3.3. The compacton on the right of the picture is the $c = 1$ compacton after its emergence from the interaction.	82
3.5	K(2, 2) equation: evolution of the initial condition $u(x, 0) = \cos^4(\frac{x}{6})\chi_{[-3\pi, 3\pi]}(x)$. The data in the plot were obtained by adding the viscosity $\eta_2 = 0$ and $\eta_4 = 10^{-3}$	84
3.6	K(2, 2) equation: decomposition of very narrow initial data $u(x, 0) = \cos^4(\frac{3x}{4})\chi_{[-\frac{2}{3}\pi, \frac{2}{3}\pi]}(x)$, showing a sequence of shocks formed close to the left endpoint of the support. The simulation was done with added dissipation $\eta_4 = 10^{-3}$	85
3.7	Evolution of the same data as in Figure 3.6, for larger times.	85
3.8	Illustration of the steepening at the right edge of the support for the same data as in Figure 3.5.	86
3.9	K(2, 2) equation: evolution of the initial condition $u(x, 0) = \sin(\frac{\pi x}{3}) + 1.1$. The profile crosses the critical line $u = 0$ around time 0.036, developing a shock discontinuity for later times.	88

3.10	Detail of the approach to singularity for the same solution to the $K(2, 2)$ equation as in Figure 3.9. Dots (black) represent the numerical solution obtained without adding any dissipative term, while the continuous (light-blue) line was obtained with $\eta_4 = 10^{-3}$ (the two curves are almost indistinguishable in the plot).	89
3.11	$K(4, 4)$ equation: collision among two compactons with speeds $c_1 = 2$ and $c_2 = 1$. This simulation was obtained with added viscosity $\eta_2 = 0$ and $\eta_4 = 3 \times 10^{-5}$	90
3.12	The figure shows two later snapshots of the evolution of the same data as in Figure 3.11, showing the separation of the $c = 1$ compacton from the residual left at the site of the interaction (notice that the faster, $c = 2$ compacton has been removed and is not visible in the plot).	91
3.13	$K(4, 4)$ equation: decomposition of the compactly supported initial data $u(x, 0) = \cos(\frac{\pi x}{20})\chi_{[-10,10]}(x)$. Data obtained with added dissipation $\eta_4 = 10^{-4}$	92
3.14	Initial phase of the decomposition of the profile $u(x, 0) = \cos^4(\frac{\pi x}{20})\chi_{[-10,10]}(x)$, showing in detail the spiky oscillations formed close to the left edge of the support. As compared to the data in Figure 3.13, the oscillations are more pronounced, but appear to have the same shape. These data were obtained with $\eta_2 = 0$ and $\eta_4 = 10^{-4}$	93
3.15	$K(4, 4)$ equation: evolution of the smooth positive profile $u(x, 0) = 1.1 + \sin(\frac{\pi x}{10})$. It is shown how this profile approaches the line $u = 0$ forming a number of singular spikes. Data obtained with $\eta_2 = \eta_4 = 0$	94
4.1	Numerical solution of the equation (4.10) with initial condition $u(x, 0) = 1.1 + \sin(\frac{\pi}{3}x)$. The solution approaches the line $u = 0$ forming spikes with the shape (4.15).	105
4.2	Snapshots of an asymptotically stationary two-compacton solution. The two constituent solitons in the related solution to MKdV have momenta $k_1 = 2, k_2 = 1$	106

LIST OF FIGURES

4.3	Decomposition of the initial condition $u(x, 0) = \cos(\frac{\pi}{4}(x-2))\chi_{[0,4]}(x)$. The solution develops a moving interface expanding leftwards and approaches a stationary compacton solution (4.20) as $t \rightarrow \infty$	118
4.4	Decomposition of the initial condition $u(x, 0) = \cos(\frac{\pi}{8}(x-4))\chi_{[0,8]}(x)$. The solution appears to approach a train of two stationary compacton solutions for large times.	119
4.5	Space-time trajectories of the maximum of the solution (blue, dotted line) and of the left edge point of the support (black, dashed line) for the solution represented in Figure 4.3. The trajectory traced by the edge point matches precisely the prediction of (4.50) (represented by red crosses).	120
4.6	Numerical solution of the integrable $\delta = 0$ equation with initial condition $u(x, 0) = 2 \cos^2((x - 2)\frac{\pi}{12})\chi_{[-4,8]}(x)$	121
4.7	Numerical solution of the deformed $\delta = 1/4$ equation with initial condition $u(x, 0) = 2 \cos^2((x - 2)\frac{\pi}{12})\chi_{[-4,8]}(x)$. The structure emerging on the right fits very well with the shape of a stationary compacton solution.	122
4.8	Numerical solution of the deformed $\delta = \frac{3}{4}$ equation with initial condition $u(x, 0) = 2 \cos^2((x - 2)\frac{\pi}{12})\chi_{[-4,8]}(x)$. The structure emerging from the right is a travelling compacton solution with speed approximately $c \sim 0.60$	123
C.1	Depiction of the orbits of equation (C.10) with $c = -1$, $U > 0$ for different values of δ . <i>Left:</i> $\delta = 1.5$, <i>Right:</i> $\delta = 0$	138
C.2	The orbits of (C.10) with $c = -1$, $U < 0$, for different values of δ . <i>Left:</i> $\delta = 1.5$, <i>Right:</i> $\delta = 0$. The black dashed curve on the left is the stable compacton orbit obtained as a limit of a family of periodic orbits.	141

Chapter 1

\mathcal{PT} -symmetric deformations of nonlinear wave equations

1.1 Complex extensions of dynamical systems

In this chapter we consider complex deformations of classical systems, motivated by the analogy with \mathcal{PT} -symmetric quantum mechanics.

Complex extensions of classical systems have been considered in different contexts, often revealing that crucial aspects of the dynamics of a real system can be best understood as images of simpler phenomena happening in a larger complex domain. For example, the connection between the integrability of a dynamical system and its analytic properties when extended to complex time, first discovered in the seminal work of Kovalevskaya Kowalevski [1889], is at the heart of the celebrated Painlevé conjecture Ablowitz *et al.* [1978]. More recently, complex-time dynamical systems have been considered in the attempt to understand the fundamental mechanisms underlying chaos, see for example Calogero *et al.* [2005].

From another perspective, a great interest in complex classical systems has also arisen in conjunction with the study \mathcal{PT} -symmetric quantum mechanics initiated in Bender & Boettcher [1998]; Bender *et al.* [1999]. In these works, it was discovered that non-Hermitian \mathcal{PT} -symmetric complex deformations of quantum Hamiltonians may still have a real spectrum, unless the symmetry is broken on the quantum level. Complex classical \mathcal{PT} -symmetric systems were considered initially in the attempt to find parallels with the quantum behaviour. Later, these

investigations gave rise to an independent field of research into the often surprising properties of these models, even when considered purely at the classical level. This chapter is based on the work Cavaglià *et al.* [2011], and deals with the study of complex travelling wave solutions to the KdV equations and its \mathcal{PT} -symmetric deformations.

1.2 A brief introduction to \mathcal{PT} -symmetric quantum mechanics

The field of \mathcal{PT} -symmetric quantum mechanics stems from the discovery that some quantum one-dimensional Hamiltonians, despite not being manifestly Hermitian with respect to the standard $L^2(\mathbb{R})$ metric, may still admit a purely real spectrum, bounded from below Bender & Boettcher [1998]. Bender and Boettcher quote as a main source of inspiration an unpublished work by Bessis and Zinn-Justin, who conjectured that the complex cubic oscillator

$$H_1 = p^2 + i x^3, \tag{1.1}$$

relevant to describe the Yang-Lee edge singularity in statistical mechanics Fisher [1978], may have a real spectrum. Bender and Boettcher investigated numerically the family of complex anharmonic oscillators

$$H_\epsilon = p^2 + x^2(ix)^\epsilon, \tag{1.2}$$

which reduces to the standard harmonic oscillator for $\epsilon = 0$ and to (1.1) for $\epsilon = 1$ and is not Hermitian for all $\epsilon > 0$. They found that the energy levels E_n , defined by the eigenvalue problem¹

$$H\psi_n(x) \equiv -\partial_{xx}\psi_n(x) + (ix)^\epsilon\psi_n(x) = E_n\psi_n(x), \quad \psi_n \in L^2(\mathbb{R}_\epsilon), \tag{1.3}$$

were all *real* for every value $\epsilon \geq 0$. Notice that, in (1.3), the boundary conditions are defined on a complex path \mathbb{R}_ϵ . The need to deform the problem away from

¹ The eigenvalue problem is obtained by making the standard replacement $p \rightarrow -i\partial_x$ in the Hamiltonian and viewing it as a linear operator.

1. \mathcal{PT} deformations of KdV travelling waves

the real axis is due to the fact that solutions to (1.3) can have exponentially decaying asymptotics only inside sectors of the complex plane (the *Stokes sectors*) that rotate with ϵ . In order to define a continuous deformation of the harmonic oscillator spectrum, the contour \mathbb{R}_ϵ is defined to lie asymptotically within a pair of wedges given by $|\arg(x) - \theta_\epsilon| < \Delta_\epsilon$ and $|\arg(x) - \pi + \theta_\epsilon| < \Delta_\epsilon$, where

$$\Delta_\epsilon = \frac{\pi}{\epsilon + 4}, \quad \theta_\epsilon = -\pi + \frac{\epsilon}{2\epsilon + 8}\pi. \quad (1.4)$$

The reader is invited to consult Bender & Boettcher [1998], Bender [2007] and Bender & Turbiner [1993] for more details.

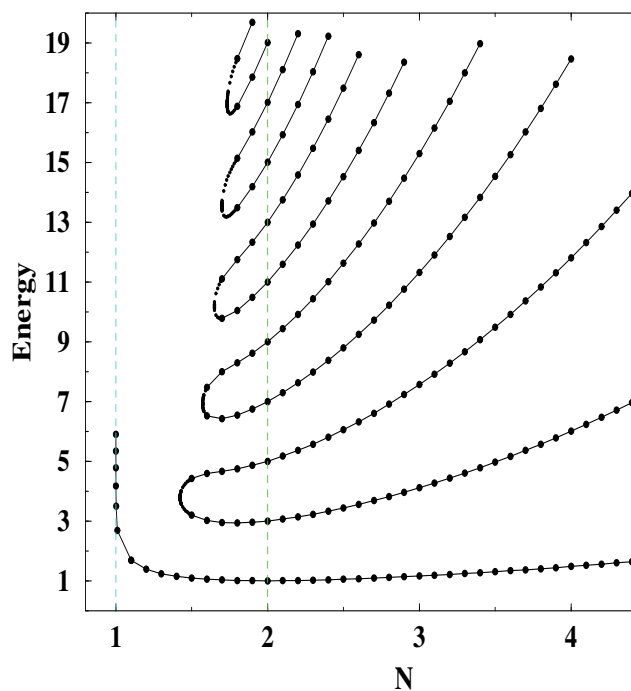


Figure 1.1: The first excited energy levels of the Hamiltonians (1.2) as a function of the deformation parameter, where $N := \epsilon + 2$. The plot is taken from Bender & Boettcher [1998].

1. \mathcal{PT} deformations of KdV travelling waves

The pattern of the first energy levels is reproduced from Bender & Boettcher [1998] in Figure 1.1. There are three distinct regions, with the harmonic oscillator lying at the boundary of two of them. The spectrum is entirely real for $\epsilon \geq 0$. Secondly, for $-1 < \epsilon < 0$ only a *finite* number of eigenvalues are real, while the rest of the spectrum is composed of pairs of complex conjugate energy levels. Finally, the spectrum becomes entirely complex for $\epsilon \leq -1$. After the numerical studies of Bender & Boettcher [1998], these results were established in Dorey *et al.* [2001] using integrable model tools and the ODE/IM correspondence Dorey *et al.* [2007].

In Figure 1.1, one can see very clearly some of the transitions from real to complex eigenvalues in the region $-1 < \epsilon < 0$, where several pairs of eigenvalues can be seen merging and then disappearing. This signals that they coalesce and then move into the complex plane developing two opposite imaginary parts. The critical point ϵ_c at which the two energy levels merge is known as an *exceptional point*: a point in the parameter space at which the spectrum becomes degenerate, through the coalescence of (typically) two eigenvectors Berry [1994]; Heiss [2012].

Bender and Boettcher understood that the reality properties described above are intimately related to the presence of an anti-linear symmetry of the Hamiltonians (1.2): \mathcal{PT} -symmetry. A \mathcal{PT} transformation is the combination of space reflection (\mathcal{P}) and time reversal (\mathcal{T}), acting on functions of the position x and momentum p as follows:

$$\mathcal{P} : f(x, p) \rightarrow f(-x, -p), \quad \mathcal{T} : f(x, p) \rightarrow (f(x, -p))^*, \quad (1.5)$$

so that

$$\mathcal{PT} : f(x, p) \rightarrow (f(-x, p))^* \equiv f(x, p)^{\mathcal{PT}} \quad (1.6)$$

It is easy to verify that all the Hamiltonians in (1.2) are left invariant by (1.6). In the previous expressions, $*$ denotes complex conjugation, and is a crucial element of the construction. It implies that, quantum mechanically, \mathcal{PT} is an *anti-linear* symmetry. Another important feature is that \mathcal{PT} is an *involution*, namely

$$\mathcal{PTPT} = \text{Id}, \quad (1.7)$$

1. \mathcal{PT} deformations of KdV travelling waves

where Id denotes the identity transformation. The important consequences of these facts were already pointed out in Wigner [1960] for a general anti-linear and involutive symmetry¹. For simplicity, let us restrict to the case when the spectrum is discrete, as is the case for the models (1.2). Then, if $\psi_n(x)$ is the eigenvector associated to the energy level E_n , one has

$$(H \cdot \psi_n(x))^{\mathcal{PT}} = (E_n \psi_n(x))^{\mathcal{PT}} = E_n^* \psi_n^{\mathcal{PT}}(x) \quad (1.8)$$

and on the other hand

$$(H \cdot \psi_n(x))^{\mathcal{PT}} = H^{\mathcal{PT}} \cdot \psi_n^{\mathcal{PT}}(x) = H \cdot \psi_n^{\mathcal{PT}}(x). \quad (1.9)$$

This shows that $\psi_n^{\mathcal{PT}}(x)$ is in turn an eigenvector, associated to the complex conjugate eigenvalue E_n^* . Then, the spectrum is entirely real provided not only the Hamiltonian, but also the eigenvectors are invariant under the anti-linear symmetry, namely if

$$\psi_n^{\mathcal{PT}}(x) = \alpha \psi_n(x), \quad (1.10)$$

where $\alpha \in \mathbb{C}$. If the property (1.10) holds for all eigenvectors, one says that the model is in a phase of *unbroken* \mathcal{PT} -symmetry, while in the phase of *spontaneously broken* symmetry some eigenvalues can exist in complex conjugate pairs.

1.2.1 Physical applications

Non-Hermitian Hamiltonians with generic complex spectra have been used to describe dissipative effects in open quantum systems long before the discoveries discussed above Moiseyev [2011]. In that context, the spectrum is in general genuinely complex, and the imaginary part of the energy levels measures the effects of dissipation. The discovery that non-Hermitian Hamiltonians possessing an anti-linear symmetry may have an entirely real spectrum suggests that they define quantum theories with a unitary evolution and no dissipation. In

¹ In fact the properties we are discussing are true in the presence of any anti-linear involutive symmetry of the Hamiltonian. The term \mathcal{PT} -symmetry is however used for historical reasons even when the symmetry has another interpretation.

1. \mathcal{PT} deformations of KdV travelling waves

some cases, it is possible to prove that such Hamiltonians are in fact Hermitian Hamiltonians in disguise, sometimes called pseudo- or quasi-Hermitian Dieudonné [1961]; Mostafazadeh [2002]; Scholtz *et al.* [1992], provided one redefines the inner product appropriately.

However, there are several examples in which the redefinition of the metric is not possible and the system, despite having a real spectrum, is not equivalent to any Hermitian counterpart and can show genuinely new features ¹. So far, the most interesting applications of the ideas of \mathcal{PT} -symmetric quantum mechanics in physics moreover lie at the interface between dissipative and “Hermitian” behavior and revolve around the \mathcal{PT} -symmetry breaking phase transition. The merging of pairs of eigenvalues at exceptional points can describe new classes of physical phenomena (see for example Fagotti *et al.* [2011]; Günther *et al.* [2007]; Uzdin *et al.* [2011] and Berry [1994]; Heiss [2012] for a general review on the applications of exceptional points). A transition with similar characteristics appears also in the study of the localization/delocalization transition of magnetic flux lines in type-II superconductors Hatano & Nelson [1996]. More recently, the \mathcal{PT} -symmetry breaking transition has been realized experimentally in optic waveguides Klaiman *et al.* [2008]; Kottos [2010]; Rüter *et al.* [2010].

1.2.2 Comparison of quantum/classical behaviour

Bender, Boettcher and Meisinger discovered in Bender *et al.* [1999] that the \mathcal{PT} -symmetry breaking transition has a surprising classical counterpart. Namely, they studied the *classical* trajectories of particles governed by the Hamiltonians (1.2), and obeying the resulting equations of motion:

$$E = \dot{x}^2 + x^2(ix)^\epsilon, \quad (1.11)$$

where \dot{x} denotes differentiation with respect to time: $\dot{x} \equiv \frac{d}{dt}x$. Notice that, while we will always consider the time variable t to be real, for $\epsilon \neq 0$ we are forced to extend the coordinate x in the complex domain. In Bender *et al.* [1999], the

¹Surprisingly, it has been shown that this is the case even for the anharmonic oscillators discussed above Siegl & Krejčířik [2012].

1. \mathcal{PT} deformations of KdV travelling waves

constant of motion E was taken to be real: $E \in \mathbb{R}^1$. This ensures the preservation of \mathcal{PT} -symmetry at the classical level, meaning that the orbits of the system are symmetric when reflected across the imaginary axis.

Bender, Boettcher and Meisinger discovered that

- For $\epsilon \geq 0$ all the solutions to (1.11) follow closed periodic orbits, and almost all the orbits are \mathcal{PT} symmetric ².
- For $\epsilon < 0$ all the the orbits are open and spiral to infinity in an infinite amount of time. None of these orbits is \mathcal{PT} -symmetric.

The fact that the boundary of these two classically well distinct regions is the same as for the two quantum phases is very suggestive. Analogies between classical and quantum behaviour were also observed in other, more general models. For example, the same two statements above were found to hold for a family of potentials with an added centrifugal term in Millican-Slater [2004]. However there are also examples of models in which such correlations were not observed Dey & Fring [2013]; Mandal & Mahajan [2013].

Moreover, the behaviour of the solutions to these differential equations is surprisingly rich and was investigated in detail in many other works such as Bender *et al.* [2006] and Bender & Darg [2007]. In particular, despite the fact that all the trajectories for $\epsilon > 0$ are periodic, they show a very rich topological variety due to the fact that the motion takes place on a Riemann surface rather than on the complex plane. In fact, the velocity field defined by

$$\dot{x} = \sqrt{E - x^2(ix)^\epsilon} \tag{1.12}$$

has a branch point at $x = 0$, which for irrational values of ϵ connects an infinite number of sheets. The topology of the trajectories can be very intricate, because, when projected on a single copy of the complex plane, an orbit exploring different Riemann sheets will normally show many self-intersections. Besides, (1.12) has

¹ In fact, $E \in \mathbb{R}$ is then an inessential parameter which can be rescaled at will simply by redefining x or t , so that we can take $E = 1$.

² Isolated examples of non \mathcal{PT} -symmetric periodic orbits were noticed in Bender & Darg [2007]. In Bender *et al.* [2006], the authors also speculate that there may isolated examples of open orbits in this region.

1. \mathcal{PT} deformations of KdV travelling waves

square root branch points at every point x_{tp} such that the argument of the square root is null:

$$E - x_{\text{tp}}^2 (ix_{\text{tp}})^\epsilon = 0. \quad (1.13)$$

Such points, where the velocity of the particle is zero while its acceleration is nonzero, are known as *turning points* of the dynamical system. In the present case there are in general infinitely many turning points, living on different Riemann sheets. Turning points play an important role in organizing the phase portrait of the system as the orbits can be naturally classified in families of topologically equivalent orbits, with trajectories of the same family encircling the same set of turning points. In Bender *et al.* [2006], Bender & Darg [2007], the topology of orbits connecting a generic pair of turning points was shown to undergo several transitions as ϵ is varied. In Bender & Jones [2011], these observations were related to the reality properties of the spectrum of a related quantum problem, obtained by imposing boundary conditions in a pair of Stokes sectors different from the one described in (1.4). Further analogies between quantum mechanics and complex classical mechanics were proposed in other works (see for instance Bender *et al.* [2010a,b]).

A slightly different problem was considered in Anderson *et al.* [2011]; Bender *et al.* [2008]. In these works, the authors investigated the classical orbits of some anharmonic oscillator Hamiltonians (such as (1.11) for $\epsilon \in \mathbb{N}$) allowing the integration constant E to be complex. For nonreal values of E , the orbits are no longer \mathcal{PT} symmetric, and were shown to be in general open and space filling. We will rediscover these observations below (in particular in Section 1.3.3.3), as some of the same potential problems arise from the reduction of the KdV equation and its deformations.

1.2.3 \mathcal{PT} symmetric deformations of nonlinear wave equations

The extremely interesting phenomena described above have sparked a vast research activity on the classical properties of complex \mathcal{PT} -symmetric systems. New

directions of research have included dynamical systems in more than one dimension such as the Lorenz system of ODEs Bender *et al.* [2009], many-body systems such as Calogero-Moser models Fring & Znojil [2008], Fring & Smith [2010] and PDEs Fring [2007], Bender *et al.* [2007], Assis & Fring [2009b], Assis & Fring [2009a], Bender & Feinberg [2008]. In particular, the authors of these works consider parametric families of \mathcal{PT} -symmetric deformations of a given system. An interesting question, inspired by the simple case of the anharmonic potentials, is whether it is still possible to recognize a classical \mathcal{PT} -symmetry breaking transition: a sudden change in the topological properties of the orbits such as the change from open to closed orbits, associated to a loss of their symmetry.

In the rest of this chapter and in the next, we will explore the deformations of two well-known nonlinear wave models: the Korteweg-de Vries (KdV) equation and the inviscid Burgers equation, respectively.

1.3 The KdV equation: complex extension of travelling waves and \mathcal{PT} -symmetric deformations

1.3.1 The KdV equation and its \mathcal{PT} -symmetric deformations

The KdV equation reads

$$u_t + \beta uu_x + \gamma u_{xxx} = 0. \quad (1.14)$$

This equation famously arises as an asymptotic description of small-amplitude waves in shallow water Korteweg & de Vries [1895], as well as in other physical contexts (see Ablowitz & Segur [1981] for a survey). In physical applications, the constants β , γ are normally real and could be simply eliminated by a redefinition of x , t and u . Here, however, in the spirit of the complex extension of classical physics motivated above, we will also consider complex values for these coefficients, and in general consider complex solutions.

1. \mathcal{PT} deformations of KdV travelling waves

Notice that the complex KdV equation has been considered before, and is physically relevant in the theory of water waves Levi [1994]; Levi & Sanielevici [1996], where it reduces to the standard, real KdV equation in a specific limit of almost horizontal flow.

In this thesis we only scratch the surface of the properties of the KdV equation, and in particular do not discuss its beautiful integrability properties. Moreover, we will restrict our analysis only to a very limited class of solutions, namely travelling wave solutions and two-soliton solutions (for the discussion of more general solutions to the complex KdV equation, see Birnir [1986], Bona & Weissler [2009] and references therein). Beside considering complex extensions of these solutions, we will also consider how they are modified by some \mathcal{PT} -symmetric deformations of the KdV equation. The relevant definition of \mathcal{PT} -symmetry will be given below. The KdV equation (1.14) can be written in the Hamiltonian form (see Olver [2000])

$$u_t = \mathcal{J} \frac{\delta}{\delta u} H_{\text{KdV}}, \quad (1.15)$$

where the skew-adjoint operator $\mathcal{J} = \partial_x$ defines the relevant symplectic structure, $\frac{\delta}{\delta u}$ denotes functional differentiation and the Hamiltonian H_{KdV} is

$$H_{\text{KdV}} = \int_{-\infty}^{\infty} \mathcal{H}_{\text{KdV}} dx, \quad (1.16)$$

with

$$\mathcal{H}_{\text{KdV}} = -\frac{\beta}{6} u^3 + \frac{\gamma}{2} u_x^2 \quad . \quad (1.17)$$

The Hamiltonian H_{KdV} , which has the physical interpretation of the energy of the solution, is one of the infinitely many conserved quantities of this integrable equation. We mention (as we will use these notions in Section 4.2.3) that the KdV equation also admits a second Hamiltonian formulation, with a different definition both of the symplectic structure and of the Hamiltonian density. As discovered in Magri [1978], the presence of two compatible Hamiltonian formulations (see Magri [1978] for the precise definition) is one of the ways to prove the existence of infinitely many symmetries.

1. \mathcal{PT} deformations of KdV travelling waves

\mathcal{PT} -symmetry Let us now discuss \mathcal{PT} -symmetry. The equation is invariant under a simultaneous flip of space and time $x \mapsto -x$, $t \mapsto -t$, provided the field transforms simply as $u(x, t) \mapsto u(-x, -t)$ ¹. Adding complex conjugation to our definition, the equation is \mathcal{PT} -symmetric provided it has real coefficients. Since we will shortly discuss a second possible realisation of an anti-linear symmetry, let us denote the symmetry we have just described as \mathcal{PT}_+ . Therefore the system is invariant under

$$\mathcal{PT}_+ : x \mapsto -x, t \mapsto -t, i \mapsto -i, u \mapsto u \quad \text{for } \beta, \gamma \in \mathbb{R}. \quad (1.18)$$

A solution is \mathcal{PT}_+ -symmetric if $u(x, t) = u^*(-x, -t)$. It is particularly interesting to study examples of solutions which are not \mathcal{PT}_+ -symmetric although $\beta, \gamma \in \mathbb{R}$; in the spirit of Section 1.2.2, such solutions are a classical example of *spontaneous symmetry breaking*, and are expected to be qualitatively different from symmetric solutions.

Besides the definition (1.18), one could regard the equation as \mathcal{PT} -symmetric (with another definition of the symmetry that we will indicate as \mathcal{PT}_-) also if $i\beta, \gamma \in \mathbb{R}$. In this case, in fact, the equation is invariant under

$$\mathcal{PT}_- : x \mapsto -x, t \mapsto -t, i \mapsto -i, u \mapsto -u \quad \text{for } i\beta, \gamma \in \mathbb{R}, \quad (1.19)$$

and \mathcal{PT}_- -symmetric solutions are characterised by $u(x, t) = -u^*(-x, -t)$.

Deformations It is simple to construct a \mathcal{PT} -symmetry preserving deformation of a given model by generalizing (1.3). Namely, any quantity $\phi(x, t)$ transforming as $\mathcal{PT} : \phi(x, t) \mapsto -\phi(x, t)$ under the symmetry can be deformed as $\phi(x, t) \mapsto -i[i\phi(x, t)]^\epsilon$. The new quantity will remain anti- \mathcal{PT} -symmetric with the crucial difference that the overall minus sign is generated from the antilinear nature of the \mathcal{PT} -operator, i.e. $i \mapsto -i$, rather than from $\phi(x, t) \mapsto -\phi(x, t)$. The undeformed case is recovered for $\epsilon = 1$ ². The paper Bender *et al.* [2007] was the first to

¹ This rule is in accordance with the physical picture, where $u(x, t)$ represents the elevation of the wave in the vertical direction.

² Notice that this definition is slightly different from (1.3), where the undeformed model is obtained for $\epsilon = 0$. This is simply due to different conventions in the literature.

1. \mathcal{PT} deformations of KdV travelling waves

consider a complex deformation of the KdV model, obtained by applying the recipe discussed above to the convective term of the equation:

$$u_t + \beta(-i)u(iu_x)^\epsilon + \gamma u_{xxx} = 0, \quad \beta, \gamma \in \mathbb{R}. \quad (1.20)$$

Another possibility, as proposed in Fring [2007], is to deform directly the Hamiltonian density appearing in (1.15) (while leaving unchanged ¹ the operator $\mathcal{J} = \partial_x$). The resulting deformed equation was shown to have at least an advantage over (1.20), namely the existence of two conserved quantities, energy and momentum (in contrast, the models (1.20) for $\epsilon > 1$ are not Hamiltonian) ².

For the two possibilities (1.18), (1.19) to define \mathcal{PT} , there are two possible rules for the deformation. We denote them as

$$\delta_\epsilon^+ : u_x \mapsto u_{x,\epsilon} := -i(iu_x)^\epsilon \quad \text{or} \quad \delta_\epsilon^- : u \mapsto u_\epsilon := -i(iu)^\epsilon. \quad (1.21)$$

Accordingly we define the deformed models by the following Hamiltonian densities

$$\mathcal{H}_\epsilon^+ = -\frac{\beta}{6}u^3 - \frac{\gamma}{1+\epsilon}(iu_x)^{\epsilon+1}, \quad \text{or} \quad \mathcal{H}_\epsilon^- = \frac{\beta}{(1+\epsilon)(2+\epsilon)}(iu)^{\epsilon+2} + \frac{\gamma}{2}u_x^2, \quad (1.22)$$

with corresponding equations of motion

$$u_t = \partial_x \frac{\delta}{\delta u} \mathcal{H}_\epsilon^+ \rightarrow u_t + \beta u u_x + \gamma u_{xxx,\epsilon} = 0 \quad (1.23)$$

$$u_t = \partial_x \frac{\delta}{\delta u} \mathcal{H}_\epsilon^- \rightarrow u_t + (-i)\beta(iu)^\epsilon u_x + \gamma u_{xxx} = 0, \quad (1.24)$$

respectively. The models related to \mathcal{H}_ϵ^+ were studied in Fring [2007]. The second family \mathcal{H}_ϵ^- was introduced in Cavaglià *et al.* [2011] and correspond to complex versions of the generalized KdV equations. For the higher deformed derivatives we use here the notation $u_{xx,\epsilon} := \partial_x u_{x,\epsilon}$, $u_{xxx,\epsilon} := \partial_x^2 u_{x,\epsilon}, \dots, u_{nx,\epsilon} := \partial_x^{n-1} u_{x,\epsilon}$, which means we only deform the first derivative and keep acting on it with ∂_x to define the higher order derivatives.

¹Deforming \mathcal{J} would give rise to other possible rules of deformations, which will not be considered in this work.

² Consequently, travelling wave solutions of (1.20) are more difficult to study, since in general they are described by a second order ODE (while a first order ODE is sufficient for the models of Fring [2007]).

Finally, let us mention that, as pointed out in Bender *et al.* [2007], many important integrable wave equations are \mathcal{PT} -symmetric. However, integrability is a very fragile property and we expect that it will not be preserved under the deformation.

1.3.2 Complex extension of travelling waves

Travelling wave solutions are obtained from (1.14) by making the assumption $u(x, t) := u(x - ct)$, where c denotes the speed of the wave. This leads to an ordinary differential equation, describing the possible profiles of translational waves. We denote the independent variable of this ODE as $\zeta = x - ct$. Then, after two integrations and introducing the integration constants κ_1 and $\kappa_2 \in \mathbb{C}$, we find the first order equation:

$$\dot{u}^2 = \frac{2}{\gamma} \left(\kappa_2 + \kappa_1 u + \frac{c}{2} u^2 - \frac{\beta}{6} u^3 \right). \quad (1.25)$$

Normally, these integration constants would be fixed by imposing suitable boundary conditions on the solution. A typical requirement is that u and its derivatives are asymptotically vanishing, namely

$$\lim_{\zeta \rightarrow \pm\infty} u(\zeta) = \lim_{\zeta \rightarrow \pm\infty} \dot{u}(\zeta) = 0 \quad (1.26)$$

or periodic, namely

$$u(\zeta + T) = u(\zeta) \quad (1.27)$$

for some real period T . Since we are interested in generic complex solutions to the KdV equation, we will be more general and regard κ_1 and κ_2 as free complex parameters. We will see shortly that most solutions will be open orbits.

We are particularly interested to examine whether there are orbits that break the \mathcal{PT}_+ or \mathcal{PT}_- -symmetry of the model. One possibility to achieve this is clearly to take generic complex values for the constants κ_1 and κ_2 . These parameters are simply related to the three zeros of the polynomial appearing in the rhs of (1.25).

1. \mathcal{PT} deformations of KdV travelling waves

In the following, we will denote this polynomial as

$$\frac{2}{\gamma} \left(\kappa_2 + \kappa_1 u + \frac{c}{2} u^2 - \frac{\beta}{6} u^3 \right) := \lambda P(u), \quad \lambda = -\frac{\beta}{3\gamma}, \quad (1.28)$$

and

$$P(u) := (u - A)(u - B)(u - C). \quad (1.29)$$

The zeros A , B and C satisfy the constraint

$$A + B + C = \frac{3c}{\beta}, \quad (1.30)$$

and the positions of two of them (say, A and C) can be chosen freely by taking

$$\kappa_1 = \frac{1}{6} [\beta(A^2 + AC + C^2) - 3c(A - C)], \quad (1.31)$$

$$\kappa_2 = \frac{AC}{6} [3c - \beta(A + C)]. \quad (1.32)$$

After a further integration, (1.25) can therefore be rewritten as

$$\pm \sqrt{\lambda} (\zeta - \zeta_0) = \int du \frac{1}{\sqrt{P(u)}}, \quad (1.33)$$

which gives rise in general to an elliptic function. Notice the similarity with (1.11): in fact, equation (1.28) is simply the equation for the motion of a single particle in a potential $P(u)$, and in the following we adopt this language referring to u as the velocity field. Notice that the zeros of the polynomial A , B , C correspond to turning points.

In Table 1.1, we summarise the possible choices of parameters preserving either of the definitions of \mathcal{PT} -symmetry we have given.

	β	γ	A	κ_1	κ_2	symmetry of orbits
\mathcal{PT}_+ :	$\in \mathbb{R}$	$\in \mathbb{R}$	$\in \mathbb{R}$	$\in \mathbb{R}$	$\in \mathbb{R}$	reflection w.r.t. real axis
\mathcal{PT}_- :	$\in i\mathbb{R}$	$\in \mathbb{R}$	$\in i\mathbb{R}$	$\in i\mathbb{R}$	$\in \mathbb{R}$	reflection w.r.t. imaginary axis

Table 1.1: \mathcal{PT} -symmetric choices of the parameters.

1. \mathcal{PT} deformations of KdV travelling waves

Deformation of travelling waves In the deformed case, we still obtain two first-order potential systems of the form $\dot{u}^2 = V(u)$. After a brief calculation, one in fact finds, for the two deformations considered above:

- for the $\mathcal{H}_\varepsilon^+$ model,

$$\dot{u}^2 = V_{+, \varepsilon}(u) \equiv \left(i^{\varepsilon-1} \frac{\beta(1+\varepsilon)}{6\gamma\varepsilon} P(u) \right)^{\frac{2}{1+\varepsilon}}, \quad (1.34)$$

where $P(u)$ is the same third order polynomial introduced in (1.28) ;

- for the $\mathcal{H}_\varepsilon^-$ model,

$$\dot{u}^2 = V_{-, \varepsilon}(u) \equiv \frac{2}{\gamma} \left(\kappa_2 + \kappa_1 u + \frac{c}{2} u^2 - \beta \frac{i^\varepsilon}{(1+\varepsilon)(2+\varepsilon)} u^{2+\varepsilon} \right). \quad (1.35)$$

Some preliminary observations:

- We see that, for the deformation $\mathcal{H}_\varepsilon^+$, the potential has three zeros at the same locations A, B, C as for the undeformed equation, specified by (1.30-1.32). As we will see shortly, due to their different algebraic nature these zeros are not turning points and their local characteristics depend on ε . See Section 1.3.4.
- For the second family of models, the number of zeros of the potential changes with ε . For $\varepsilon = n \in \mathbb{N}$, there are exactly n zeros, while for generic $\varepsilon \in \mathbb{R}$ there are infinitely many. In fact, for irrational values of ε , $V_\varepsilon^-(u)$ has an infinite-order branch point at $u = 0$ and the zeros are distributed on infinitely many Riemann sheets. These zeros still behave as turning points, as in the undeformed case, and there is no other type of singularity. This second deformation therefore will generate orbits similar to those of the anharmonic oscillator potentials of Section 1.2, with a dense “forest of turning points”¹ for large values of ε . In this work, we concentrate more on the first type of deformation; however, some examples will be studied in Section 1.3.5.

¹quoting Bender *et al.* [2006]

We make a last comment before starting to consider some solutions in detail. In (1.25, 1.34, 1.35), the velocity \dot{u} is defined modulo a sign. This means that every solution has a partner solution which simply retraces the same orbit backwards. For this reason, in the plots presented in the rest of the chapter we simply depict different “orbits”: each corresponds to two solutions.

1.3.3 The undeformed equation

In the undeformed case, it is easy to find the solution explicitly, as (1.33) can be solved in terms of an elliptic function. The solution is even simpler when some of the roots coincide. Let us present in order the different possibilities.

1.3.3.1 Rational solutions

Rational solutions are obtained with the factorisation

$$P(u) = (u - A)^3, \quad (1.36)$$

which can be realised with the following choice of integration constants:

$$\lambda = -\frac{\beta}{3\gamma}, \quad \kappa_1 = -\frac{c^2}{2\beta}, \quad \kappa_2 = \frac{c^3}{6\beta^2} \quad \text{and} \quad A = \frac{c}{\beta}. \quad (1.37)$$

From the previous equations, we see that, given a \mathcal{PT}_\pm -symmetric choice of β and γ , it is not possible to break the symmetry “spontaneously” with the value of A . Moreover, breaking the symmetry of the equation by taking generic complex values of γ , β simply amounts to a rotation of the solutions in the complex u -plane.

We can easily find the solution explicitly by computing the integral (1.33):

$$u(\zeta) = \frac{c}{\beta} - \frac{12\gamma}{\beta(\zeta - \zeta_0)^2}. \quad (1.38)$$

When viewed in the two-dimensional complex plane, this equation is the rational parametrisation of a cardioid. A complete family of complex solutions, filling the complex u -plane and symmetric with respect to the line $\arg(u) = \arg(\frac{\gamma}{\beta})$, is obtained by changing ζ_0 .

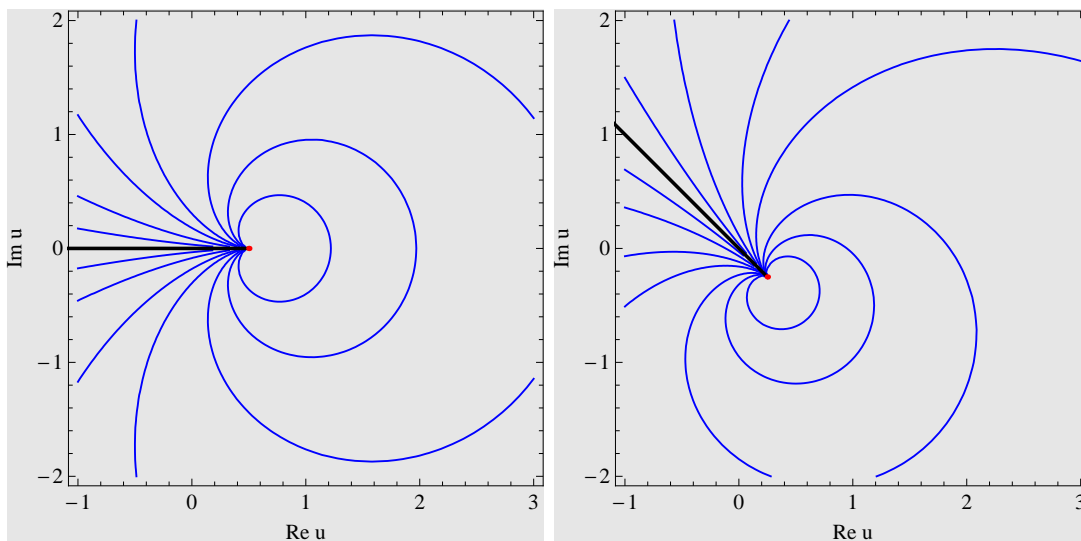


Figure 1.2: Complex rational solutions of the KdV equation: in the left panel \mathcal{PT} -symmetric solutions for $c = 1$, $\beta = 2$, $\gamma = 3$ and $A = 1/2$; in the right panel, we have taken $c = 1$, $\beta = 2 + i2$, $\gamma = 3$ and consequently $A = (1 - i)/4$.

Two examples are shown in Figure 1.2, where we have traced in black the square-root branch cut of the velocity \dot{u} . On the second Riemann sheet, the orbits are the same but they are travelled in the opposite direction. Let us make a comment on the nature of the point $u = A$. This point cannot be reached in any finite amount of time, and is an accumulation point for all the orbits. Moreover, orbits can only approach this point along the direction of the line $\arg(u) = \arg(\frac{\gamma}{\beta})$. This is a particular case of the general behaviour of orbits around algebraic zeros, see Section 1.3.4.

1.3.3.2 Trigonometric solutions

Now let us consider the factorization $P(u) = (u - A)^2(u - B)$, which can be obtained by taking

$$\lambda = -\frac{\beta}{3\gamma}, \quad \kappa_1 = \frac{A}{2}(\beta A - 2c), \quad \kappa_2 = \frac{A^2}{6}(3c - 2\beta A) \quad \text{and} \quad B = \frac{3c}{\beta} - 2A. \quad (1.39)$$

1. \mathcal{PT} deformations of KdV travelling waves

The general solution in this case is

$$u(\zeta) = A + (B - A) \cosh^{-2} \left[\frac{1}{2} \sqrt{A - B} \sqrt{\lambda} (\zeta - \zeta_0) \right]. \quad (1.40)$$

The phase portrait of these solutions can already show an interesting variety depending on the value of the parameters. It is interesting to classify the different possible behaviours of the orbits around the double zero $u = A$. This is clearly no longer a turning point. Instead, this point is characterised by the vanishing of both \dot{u} and \ddot{u} (and therefore of all higher derivatives), meaning that the equation admits the constant solution $u(\zeta) = A$. This is therefore a *stationary point*. For each of the two signs of the square root, the equation

$$\dot{u} = \pm \lambda (u - A) \sqrt{u - B} \quad (1.41)$$

now defines a smooth dynamical system in the neighborhood of $u = A$, which can be studied locally with the standard tools for two-dimensional real systems. It is convenient to separate u into its real and imaginary part, $u = u^R + iu^I$, $u^R, u^I \in \mathbb{R}$, so that (1.41) becomes:

$$\dot{u}^R = +\text{Re} \left[\sqrt{\lambda} \sqrt{P(u^R + iu^I)} \right] \quad \text{and} \quad \dot{u}^I = +\text{Im} \left[\sqrt{\lambda} \sqrt{P(u^R + iu^I)} \right], \quad (1.42)$$

where we have restricted to the $+$ sign in (1.41), since on the second sheet the orbits are the same, but simply travelled in the opposite direction. According to the classic classification reviewed in Appendix A, the behaviour of the solutions around $u = A$ is determined by the eigenvalues of the Jacobian matrix, which here is simply

$$J^{(A)} = \left(\begin{array}{cc} \frac{\partial \text{Re}[\sqrt{V(u)}]}{\partial u^R} & \frac{\partial \text{Re}[\sqrt{V(u)}]}{\partial u^I} \\ \frac{\partial \text{Im}[\sqrt{V(u)}]}{\partial u^R} & \frac{\partial \text{Im}[\sqrt{V(u)}]}{\partial u^I} \end{array} \right) \Bigg|_{u=A} = \left(\begin{array}{cc} \text{Re} \left[\frac{d}{du} \sqrt{V(u)} \right] & -\text{Im} \left[\frac{d}{du} \sqrt{V(u)} \right] \\ \text{Im} \left[\frac{d}{du} \sqrt{V(u)} \right] & \text{Re} \left[\frac{d}{du} \sqrt{V(u)} \right] \end{array} \right) \Bigg|_{u=A} \quad (1.43)$$

with $\sqrt{V(u)} = \sqrt{\lambda} \sqrt{P(u)}$. We denote the eigenvalues of $J^{(A)}$ by j_1, j_2 . They can be simply computed as

$$j_1 = \frac{d}{du} \sqrt{V(u)} \Big|_{u=A} = \sqrt{\lambda(A - B)}, \quad j_2 = (j_1)^*, \quad (1.44)$$

1. \mathcal{PT} deformations of KdV travelling waves

(a) (stable or unstable) <i>star node</i> ,	when $j_i \in \mathbb{R}$.
(b) <i>centre</i> ,	when $j_i \in i\mathbb{R}$.
(c) (stable or unstable) <i>focus</i> ,	in all other cases ($j_i \notin \mathbb{R}, \notin i\mathbb{R}$).

Table 1.2: Small classification of the possible behaviour around the fixed point $u = A$.

(with $\lambda = -\frac{\beta}{3\gamma}$). We see that, while in a generic two-dimensional dynamical system there is no restriction on the eigenvalues, in the present case they are related by complex conjugation as a consequence of the Cauchy-Riemann equation satisfied by the real and imaginary parts of $\sqrt{V(u)}$.

The possible behaviour at $u = A$ is therefore restricted to the cases listed in Table 1.2. Let us consider them in order.

Case (a): solitary wave solutions When the choice of the parameters A, B is such that $j_i \in \mathbb{R}$, all the orbits (apart from a single orbit connecting the fixed point to infinity, without passing through the turning point $u = B$ ¹) approach asymptotically $u = A$ for $\zeta \rightarrow \pm\infty$. They are natural complex extensions of the celebrated *solitary wave solutions*, or one-soliton solutions.

A \mathcal{PT}_+ -symmetric example is shown in Figure 1.3, left panel. Notice that relations (1.39) imply that, if the parameters β, γ are chosen in a \mathcal{PT}_\pm -symmetric way according to Table 1.1, solitary wave solutions cannot break the symmetry: otherwise it would not be possible to have $j_1 \in \mathbb{R}$. However, asymptotically constant solutions exist also if the symmetry is missing from the start (when γ and β are generically complex), as for example shown in Figure 1.4 below.

Case (b): complex periodic solutions Solutions obtained for $j_i \in i\mathbb{R}$ correspond to complex periodic orbits. These solutions have no real counterpart because in order to have periodic motion on the real axis one would need to have at least two turning points (this case will be presented below in 1.3.3.3). The phase portrait corresponding to complex periodic trigonometric solutions is presented in a \mathcal{PT}_+ -symmetric example in Figure 1.3, right panel. Looking at (1.40), we see that the period of these trigonometric solutions is given by $T = \frac{2\pi i}{\sqrt{\lambda(A-B)}} = \frac{2\pi i}{j_1}$.

¹ This escaping orbit corresponds to the choice of $\text{Im}(\zeta_0) = 2n\pi, n \in \mathbb{Z}$.

1. \mathcal{PT} deformations of KdV travelling waves

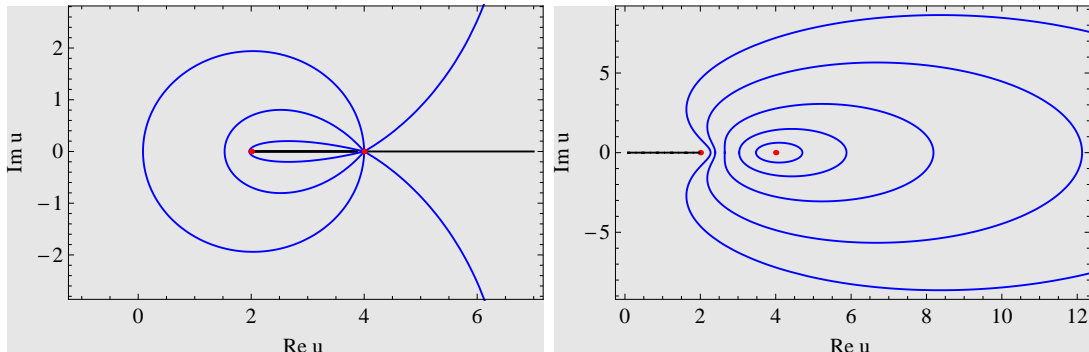


Figure 1.3: Left panel: \mathcal{PT}_+ -symmetric solitary wave solutions of the KdV equation with $c = 1$, $\beta = 3/10$, $\gamma = -3$, $A = 4$ and $B = 2$. Right panel: complex periodic \mathcal{PT}_+ -symmetric solutions of the KdV equation with $c = 1$, $\beta = 3/10$, $\gamma = 3$, $A = 4$, $B = 2$. The period is $T = 2\sqrt{15}\pi$.

We notice that this expression is the same for all orbits. In fact, this is a general feature of complex dynamical systems, which was noticed in Bender *et al.* [1999] in the case of the differential equations (1.12). The period of a closed orbit can be computed by a contour integral $\oint_{C_A} \frac{du}{\dot{u}}$, where C_A denotes the closed orbit under consideration, encircling the point $u = A$. Provided \dot{u} is an analytic function, this quantity can be computed by integrating over any loop enclosing the point $u = A$; therefore, the period is the same for all topologically equivalent orbits. In the present case the period can be re-obtained by using the theorem of residues:

$$T = \oint_{C_A} \frac{du}{\dot{u}} = \oint_{C_A} \frac{du}{\sqrt{\lambda(u-B)}(u-A)} = \frac{2\pi i}{\sqrt{\lambda(A-B)}}. \quad (1.45)$$

With the same strategy, we can compute the energy (1.16) over one period:

$$E_T = \oint_{\Gamma} \mathcal{H}[u(\zeta)] \frac{du}{u_\zeta} = \oint_{\Gamma} \frac{\mathcal{H}[u]}{\sqrt{\lambda}\sqrt{u-B}(u-A)} du = -\pi \sqrt{\frac{\beta\gamma}{3}} \frac{A^3}{\sqrt{A-B}}. \quad (1.46)$$

Also in this case, there is a single orbit escaping at infinity, identified by the choice $\text{Im}(\zeta_0) = 2n\pi$. The orbit passes through the turning point.

Case (c): open orbits Finally, when j_i is neither real nor imaginary, all solutions obtained with $\text{Im}(\zeta_0) \neq 2n\pi$, $n \in \mathbb{Z}^1$ are open orbits spiralling indefinitely around the point A . Depending on the choice of Riemann section, these orbits fall into the fixed point or spiral out of it, corresponding to a stable or unstable focus, respectively. We depict an example in Figure 1.4. Notice that this type of behaviour is associated to orbits breaking \mathcal{PT} -symmetry. Such orbits correspond to taking generic complex values for A , and are accompanied by \mathcal{PT} -symmetric conjugate orbits corresponding to the choice A^* .

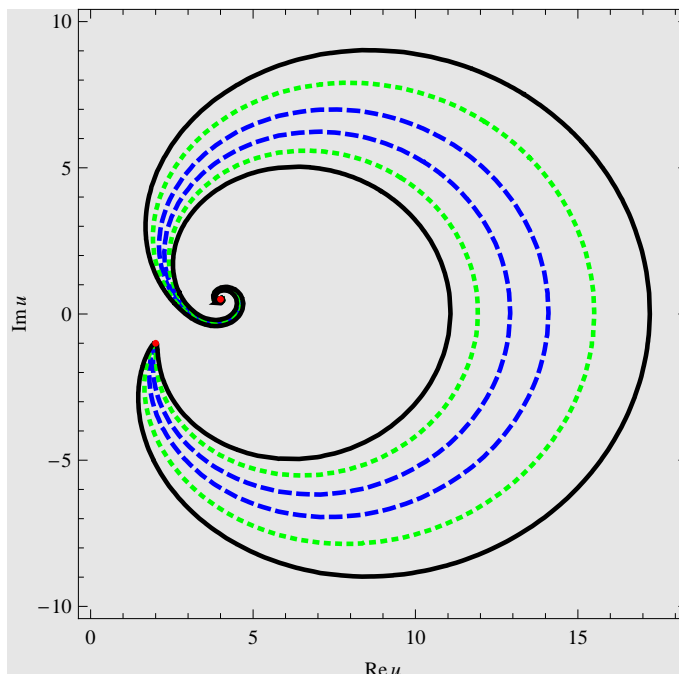


Figure 1.4: Complex trigonometric solutions of the KdV equation with “spontaneously broken” \mathcal{PT} -symmetry. $c = 1$, $\beta = 3/10$, $\gamma = 3$, $A = 4 + i/2$ and $B = 2 - i$, meaning that this family of orbits break the \mathcal{PT}_+ -symmetry of the equation. All orbits of this type are in the present case open.

Relation with \mathcal{PT} -symmetry breaking In summary, we have found that \mathcal{PT} -symmetric orbits are always either periodic or correspond to solitary waves. Orbits that break the symmetry spontaneously are very different, in particular

¹ Again, the latter case corresponds to a single orbit escaping to infinity.

they are always open. This is very reminiscent, in spirit, of the findings of Bender *et al.* [1999] that we have summarised in Section 1.2.2.

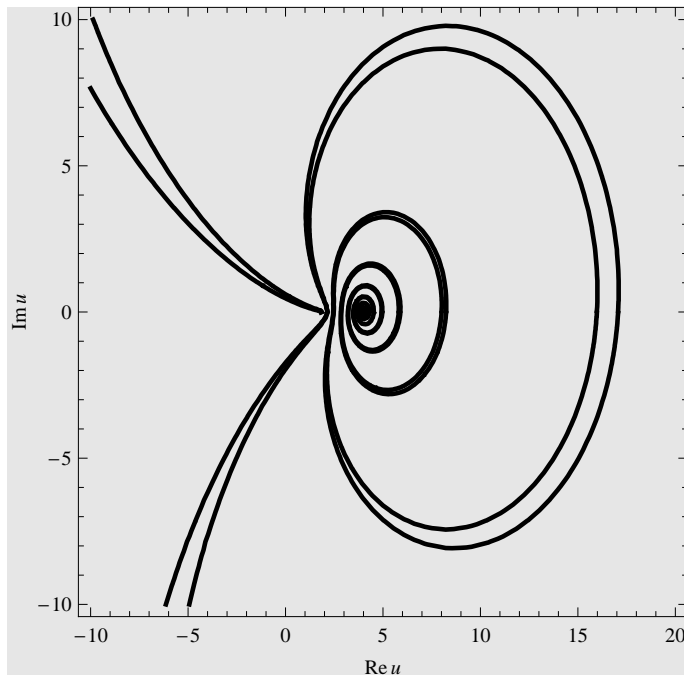


Figure 1.5: Detail of a trigonometric solution of the complexified KdV equation with broken \mathcal{PT} -symmetry. Here we have taken $c = 1$, $\beta = 3/10$, $\gamma = 3 + i/2$, $A = 4$, $B = 2$. The point $u = 4$ behaves like a *focus*. This solution is characterised by $\text{Im}(\zeta_0) = 6$.

When, on the other hand, the symmetry is *explicitly* broken, namely we take generic complex values for β , γ , solutions are almost always open, with the fixed point behaving like a focus (see Figure 1.5 for a detail). However, there are still examples of periodic or asymptotically constant orbits. They are associated to a subset of all possible choices for A , obtained by imposing the condition

$$\text{Re}\left(\sqrt{\lambda\left(3A_* + \frac{3c}{\beta}\right)}\right) = 0 \quad \text{or} \quad \text{Im}\left(\sqrt{\lambda\left(3A_* + \frac{3c}{\beta}\right)}\right) = 0. \quad (1.47)$$

Two examples are shown in Figure 1.6. The centre is unstable against perturbations. In fact, by varying the parameter A in a neighbourhood of A_* , one can have a transition between an unstable focus and a stable focus passing through the centre.

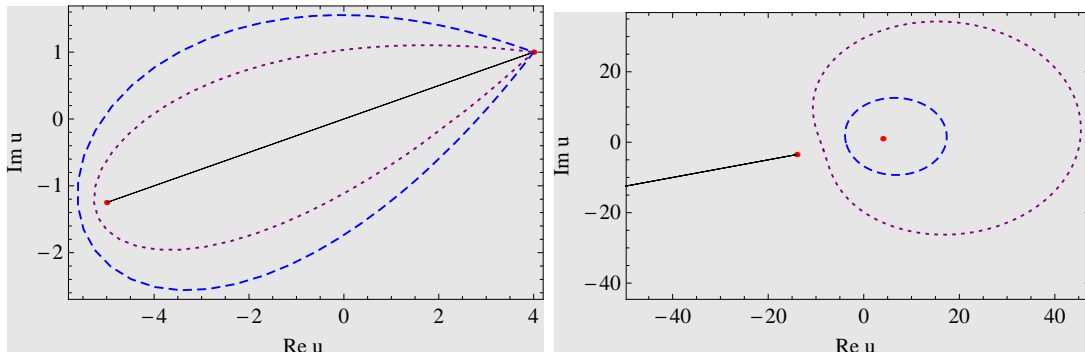


Figure 1.6: Two solutions of the non \mathcal{PT} -symmetric complex KdV equation, where the parameters have been finely tuned in order to obtain a solitary wave solution (left panel), or a periodic solution (right panel). The choice of parameters is: Left: $c = 1$, $\beta = (16 - 4i)/17$, $\gamma = -3$, $A = 4 + i$, $B = -5 - 5/4i$; Right: $c = 1$, $\beta = (-8 + 2i)/17$, $\gamma = -3$ and $A = 4 + i$, $B = -14 - 7/2i$.

1.3.3.3 Elliptic solutions

Finally, let us consider the general case of a potential $P(u) = (u-A)(u-B)(u-C)$ with three distinct turning points (the relation between A , B , C and the other parameters is given in (1.32)). In this case the solution reads:

$$u(\zeta) = A + \frac{(B-A)}{\text{sn}^2\left(\frac{1}{2}\sqrt{B-A}\sqrt{\lambda}(\zeta - \zeta_0) \middle| \frac{A-C}{A-B}\right)}, \quad (1.48)$$

where $\text{sn}(z|m)$ is Jacobi elliptic function.

In the \mathcal{PT} -symmetric situation, this corresponds to the celebrated *cnoidal solution* of KdV equation, playing an important role in the initial value problem over a periodic domain. This solution is real and periodic, oscillating between two turning points. In Figure 1.7, we present the natural extension of the cnoidal solution to the complex plane, where it is accompanied by a family of complex periodic orbits. Apart from a single real orbit running on the positive real axis between $u = C$ and $u = +\infty$, all orbits again share the same period, given by

$$\omega_1 = \frac{8}{\sqrt{B-A}\sqrt{\lambda}} K\left(\frac{A-C}{A-B}\right) \quad (1.49)$$

where $K(m)$ denotes the complete elliptic integral of the first kind.

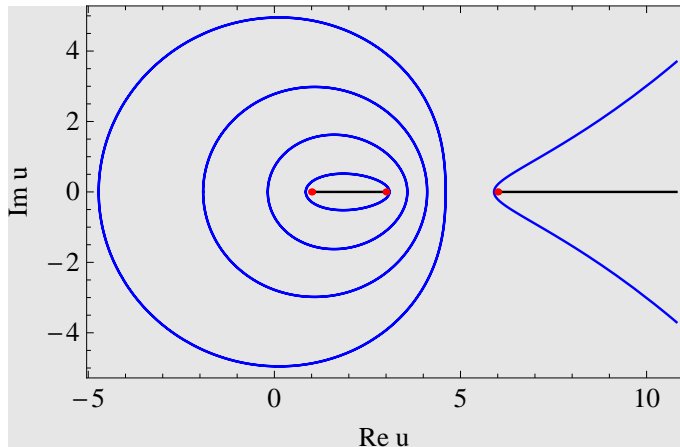


Figure 1.7: \mathcal{PT} -symmetric complex elliptic solutions of the KdV equation with $A = 1$, $B = 3$, $C = 6$, $c = 1$, $\beta = 3/10$, $\gamma = -3$ for different values of $\text{Im}\zeta_0$.

Being an elliptic function, the solution is in fact doubly periodic. The second period, which in the example shown in Figure 1.7 would be purely imaginary, is given by

$$\omega_2 = i \frac{16}{\sqrt{B - A\sqrt{\lambda}}} K \left(\frac{C - B}{A - B} \right). \quad (1.50)$$

When the symmetry is broken, we observe quite interesting trajectories which densely fill each of the two sheets covering the complex u -plane. An example is plotted in Figure 1.8. The trajectory appears to repeat indefinitely the same manoeuvre around the turning points.

A simple explanation of the space-filling character of these orbits is that, when the symmetry is broken, the two periods ω_1 , ω_2 become genuinely complex. When the imaginary parts of the two periods are not commensurable, the problem is equivalent to motion on a torus with two incommensurable frequencies: it is a classic result that this quasi-periodic motion is dense on the torus (see for example Arnol'd [1989]). As noticed in Anderson *et al.* [2011]¹, there are still *sparse* examples of periodic orbits with a broken symmetry. These more complicated

¹ Bender et al were considering simple potential systems. For an illustration of some of these orbits, see Anderson *et al.* [2011], where also quartic potentials and more general non-elliptic cases were considered. Some general polynomial potentials similar to theirs will be seen to arise from the deformations discussed below.

1. \mathcal{PT} deformations of KdV travelling waves

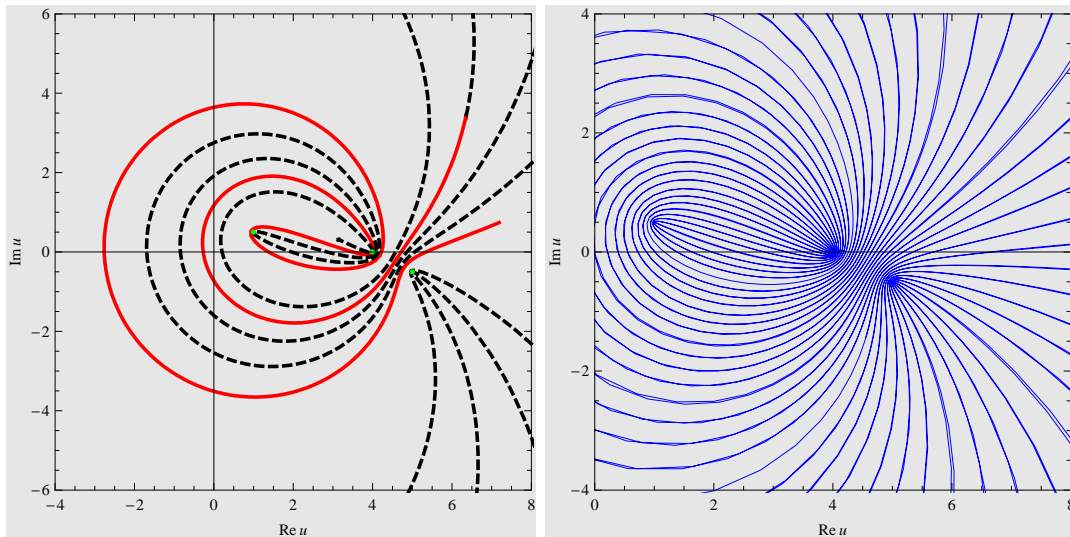


Figure 1.8: Spontaneously broken \mathcal{PT} -symmetric complex elliptic solution of the KdV equation for $\text{Im}\zeta_0 = 6$ with $A = 4$, $B = 5 - i/2$, $C = 1 + i/2$, $c = 1$, $\beta = 3/10$ and $\gamma = 3$. The left panel shows the trajectory for $-64 \leq \zeta \leq 18$ solid (red) and $18 < \zeta \leq 200$ dashed (black). In the right panel: $-200 < \zeta < 1400$. Notice that this is a single, space-filling trajectory.

periodic solutions are obtained when the two elementary periods, despite being both complex, happen to have imaginary parts commensurate to each other, in the sense that there exist two integers $m, n \in \mathbb{Z}$ such that $n\omega_1 + m\omega_2 \in \mathbb{R}$. This can also be rewritten as (see Anderson *et al.* [2011])

$$\text{Im}(m\omega_1 + n\omega_2) = 0 \rightarrow \frac{m}{n} = -\frac{\text{Im}\omega_1}{\text{Im}\omega_2}. \quad (1.51)$$

It is important to remark that, similar to what was seen in the case of trigonometric solutions, these special orbits exist only for a lower-dimensional subset of the parameter set, and, for a generic choice of parameters, we again see a strong connection between the periodicity of the orbits and \mathcal{PT} -symmetry.

Finally we may also break the \mathcal{PT} -symmetry completely by complexifying the parameters of the model β or/and γ . This situation appears totally analogous to the case of spontaneous symmetry breaking. We show an example in 1.9.

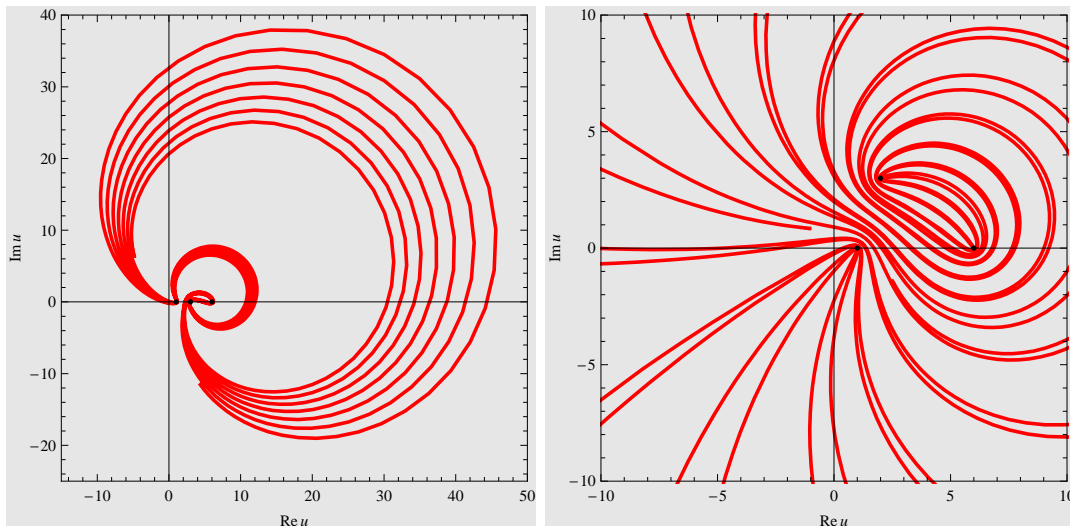


Figure 1.9: Broken \mathcal{PT} -symmetric complex elliptic solutions of the KdV equation for $\text{Im}\zeta_0 = 6$: in the left panel, $A = 1$, $B = 3$, $C = 6$, $c = 1$, $\beta = 3/10$ and $\gamma = 3 + 2i$ for $-200 \leq \zeta \leq 200$; in the right panel, $A = 1$, $B = 2 + 3i$, $C = 6$, $c = 1$, $\beta = 3/10 - i/10$ and $\gamma = 3$ for $-200 \leq \zeta \leq 200$.

1.3.4 Deformations of the KdV equation I: the \mathcal{PT}_+ -symmetric deformation

Let us come to the first type of deformation. Before presenting some examples, let us make a general comment. From (1.34), we have

$$\zeta - \zeta_0 = \exp \left[\frac{i\pi}{2(\varepsilon + 1)}(\varepsilon - 1) \right] \int du \frac{1}{[\lambda_\varepsilon P(u)]^{\frac{1}{1+\varepsilon}}}. \quad (1.52)$$

In general, the best we can do is computing the integral in terms of a complicated function $F(u)$, such that

$$\zeta - \zeta_0 = F(u). \quad (1.53)$$

While this relation is in general not invertible, we can easily obtain the orbits numerically by plotting them as lines of constant $\text{Im}(\zeta_0)$. The following plots were obtained simply as contour plots of $\text{Im}(F(u))$ in *Mathematica*.

1. \mathcal{PT} deformations of KdV travelling waves

Behaviour at general algebraic points As we have anticipated, this deformation leaves unchanged the position of the three zeros of the potential A , B , C , but changes their characteristics depending on the value of ϵ . The qualitative behaviour of the solutions of (1.34) around one of these roots (which we denote generically as k) can be understood by considering the simple model equation

$$\dot{u} = b(u - k)^\alpha, \quad (1.54)$$

where

$$\alpha = \frac{\sigma}{\epsilon + 1}, \quad (1.55)$$

and $\sigma \in \{1, 2, 3\}$ is the order of the zero of $P(u)$ at $u = k$. The solution of (1.54) in general lives on an infinitely-sheeted Riemann surface, with a branch point at $u = k$. Obviously we expect the behaviour to change abruptly depending on whether $\alpha > 1$ or $\alpha < 1$. Notice that the ‘‘regular case’’ $\alpha = 1$ stands alone: the possible behaviours for $\alpha = 1$ are the ones classified in Table 1.2. Solving (1.54) for $\alpha \neq 1$ we find

$$u(\zeta) = k + \left(-\frac{b}{\alpha}(\zeta - \zeta_0) \right)^{\frac{1}{1-\alpha}}, \quad (1.56)$$

where the value of $\text{Im}(\zeta_0)$ labels different orbits. We notice that some solutions (identified by $\text{Im}(\zeta_0) = 0$) are simply outgoing or ingoing rays, with the number of rays on every Riemann sheet depending on α . They are described by

$$\arg(u - k) = -\arg\left(\frac{b}{\alpha}\right) + \frac{2n\pi}{1-\alpha}, \quad n \in \mathbb{Z} \quad (\text{outgoing}), \quad (1.57)$$

$$\arg(u - k) = -\arg\left(\frac{b}{\alpha}\right) + \frac{(2n+1)\pi}{1-\alpha}, \quad n \in \mathbb{Z}, \quad (\text{ingoing}). \quad (1.58)$$

The difference between the cases $\alpha > 1$ and $\alpha < 1$ can be described as follows. For $\alpha > 1$ and for every value of $\text{Im}(\zeta_0)$, every orbit approaches the point $u = k$ asymptotically for $\zeta \rightarrow \pm\infty$. They form a pattern resembling flowers with $2(\alpha-1)$ petals on every Riemann sheet. An example is shown in Figure 1.10. On the contrary, for $\alpha < 1$ the rays (1.57-1.58) are the only orbits passing through the

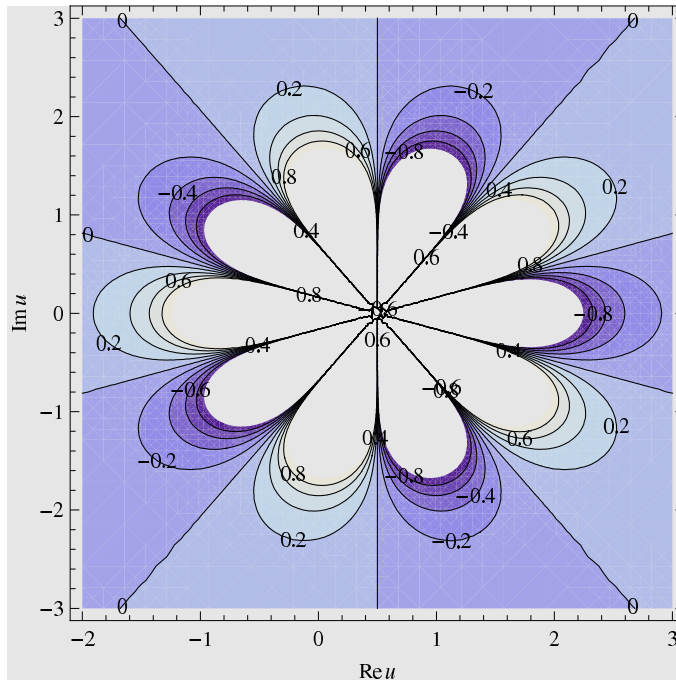


Figure 1.10: Complex \mathcal{PT} -symmetric rational solutions of the deformed KdV equation with $c = 1$, $\beta = 2$ and $\gamma = 3$ for the deformed model $\mathcal{H}_{-1/2}^+$, corresponding to the behaviour (1.54) with $k = 1/2$ and $\alpha = 6$.

point $u = k$, and neighbouring orbits form a saddle-point like pattern (see Figure 1.11).

The deflection of the orbits in the presence of such “generalised turning points” was recently discussed in the paper Bender & Hook [2014]. In this paper the rays (1.57-1.58) are referred to as “separatrix trajectories” and we adopt this terminology in the following. They are a new feature which does not exist in the undeformed case, and we will see that they divide the phase portrait in different sectors.

Let us now present some results, concentrating in particular on the two simplest factorizations: rational and trigonometric solutions.

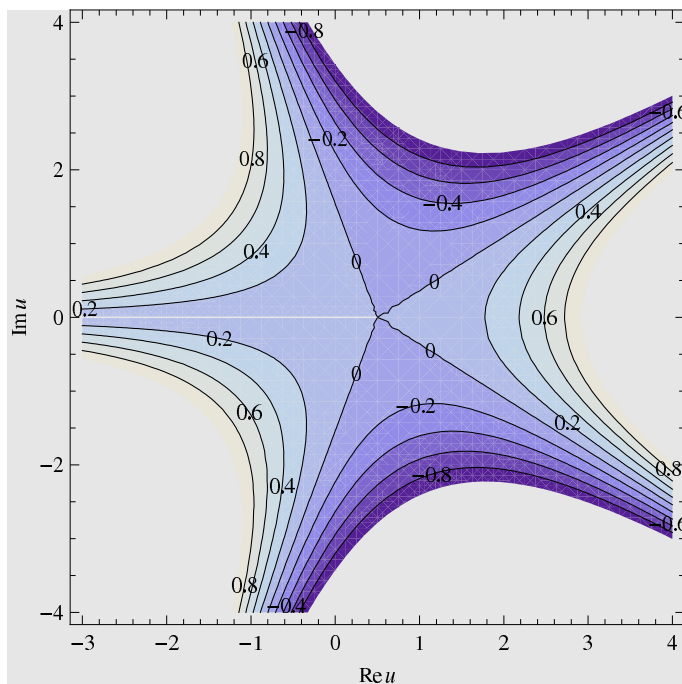


Figure 1.11: Complex \mathcal{PT} -symmetric rational solutions of the deformed KdV equation with $c = 1$, $\beta = 2$ and $\gamma = 3$ for \mathcal{H}_{-3}^+ , corresponding to the behaviour (1.54) with $k = 1/2$ and $\alpha = -3/2$.

1.3.4.1 Rational solutions

The solution for three coincident roots $A = B = C$ is

$$u(\zeta) = A - \left(\frac{(-i)^{\epsilon+1} (\epsilon - 2)^{\epsilon+1} \beta}{6\gamma(\epsilon + 1)^\epsilon} \right)^{\frac{1}{\epsilon-2}} (\zeta - \zeta_0)^{\frac{1+\epsilon}{\epsilon-2}}, \quad (1.59)$$

which is simply the same as (1.56).

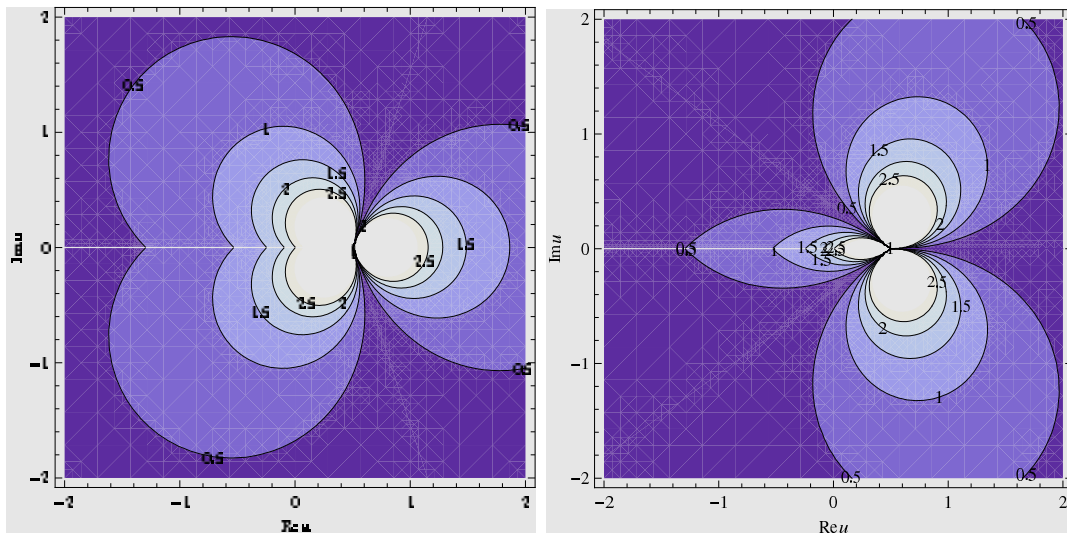
Applying (1.57 - 1.58) with $\alpha = \frac{3}{1+\epsilon}$, we see that the deflection angle between ingoing and outgoing rays is

$$\frac{\pi}{1 - \alpha} = \frac{\pi(1 + \epsilon)}{4 + \epsilon}. \quad (1.60)$$

The case $\epsilon = -\frac{1}{2}$ is illustrated in Figure 1.10. For another example let us consider the case $\epsilon = \frac{1}{3}$. Applying (1.57 - 1.58) with $\alpha = \frac{3}{1+\epsilon} = \frac{9}{4}$, we find the pattern shown in Figure 1.12, with ingoing/outgoing orbits deflected by an angle

1. \mathcal{PT} deformations of KdV travelling waves

$\frac{\pi}{5}$ at this generalised turning point. As shown in Figure 1.12, to complete the “flower” we need to go around its centre twice since in this case the solution extends over four Riemann sheets.



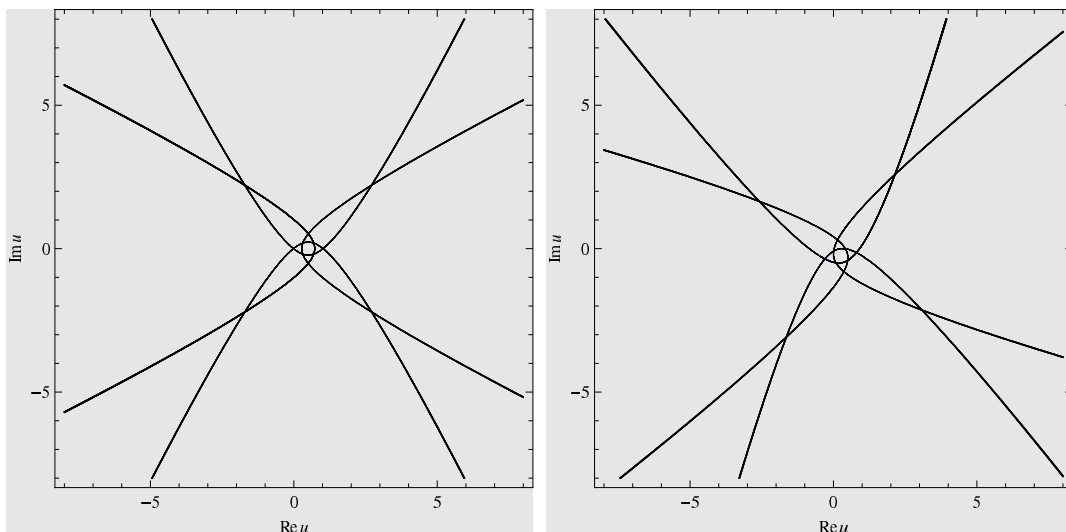


Figure 1.13: In the left panel are shown four different orbits (all of them characterised by $\text{Im}(\zeta_0) = 1$) of the \mathcal{H}_6^+ model with $c = 1$, $\beta = 2$ and $\gamma = 3$, corresponding to (1.54) with $k = 1/2$ and $\alpha = 3/7$. Each orbit makes a turn around the point $u = A$ and is deflected by an angle which approaches asymptotically $\frac{7}{4}\pi$. Notice that these four orbits live on different Riemann sheets, so that there are no intersections. In the right panel, we break \mathcal{PT} -symmetry by taking $c = 1$, $\beta = 2 + 2i$ and $\gamma = 3$, leading to $k = 1/4(1 - i)$, and the same value of α . Clearly this simply amounts to a rotation.

1.3.4.2 Trigonometric solutions

The complete solution when $B = C \neq A$ is expressed in implicit form as Fring [2007]:

$$\zeta - \zeta_0 = \Lambda_\epsilon (u - B)^{\frac{\epsilon}{1+\epsilon}} {}_2F_1 \left(\frac{\epsilon}{1+\epsilon}, \frac{2}{1+\epsilon}, 1 + \frac{1}{1+\epsilon}, \frac{u - B}{A - B} \right) \quad (1.61)$$

where Λ_ϵ is a coefficient:

$$\Lambda_\epsilon = -\frac{i}{\epsilon} \left(-\frac{6\gamma}{\beta(A - B)^2} \right)^{\frac{1}{1+\epsilon}} (1 + \epsilon)^{\frac{\epsilon}{1+\epsilon}}. \quad (1.62)$$

Depending on the value of ϵ , the phase portrait can be organized around two “flower centres” for $-1 < \epsilon < 0$, two “saddles” for $\epsilon < -1 \cup \epsilon > 1$, or a mixed configuration with A a flower center and B a saddle for $0 < \epsilon < 1$.

1. \mathcal{PT} deformations of KdV travelling waves

We consider here simply an example of the first case for $\epsilon = -\frac{1}{2}$, which however shows some features that we have observed also for other choices of ϵ . In this case the solution (1.61) simplifies considerably becoming

$$\zeta - \zeta_0 = \alpha \left(12 \log \frac{u-B}{u-A} + \frac{3(A-B)}{B-u} + \frac{9(A-B)}{A-u} + \frac{3(A-B)^2}{(A-u)^2} + \frac{(A-B)^3}{(A-u)^3} \right),$$

with $\alpha = -\frac{48i\gamma^2}{(A-B)^5\beta^2}$ (1.63)

There are no periodic solutions, and no open orbits: instead every orbit appears to be connected to either A or B at both limits $\zeta \rightarrow \pm\infty$, so that these orbits can be described as solitary wave solutions, but with an algebraic rather than exponential decay.

Also in this case, we see that \mathcal{PT} -symmetry breaking is connected to an interesting topological change in the nature of the orbits. This is illustrated in Figure 1.14, where we show the family of separatrix trajectories for the $\mathcal{H}_{-\frac{1}{2}}^+$ model, for different choices of the \mathcal{PT} -symmetry breaking parameter $\text{Im}(A)$.

The separatrix curves can be defined as orbits connecting one of the two points $u = A$ or $u = B$ to infinity, and they divide the complex the u -plane into sectors. Because they are orbits, they cannot be crossed and therefore all orbits are confined to remain within these sectors. In the Figure, these orbits have been plotted using the fact that they are characterised by $\text{Im}(\zeta_0(u)) = 0$ ¹, at least on one of the branches of the multi-valued function $\zeta(u)$ defined by (1.63). In the upper left panel of Figure 1.14, solutions are \mathcal{PT} -symmetric corresponding to a choice of real $A = 4$, $B = 2$. In the upper right panel, the symmetry has been broken by a very small imaginary part $A = 4 + \frac{i}{200000}$, $B = 2 - \frac{i}{100000}$, and we see that the network of separatrix curves suddenly changes its topology. In particular, while for the symmetric solution the points A and B are in completely disconnected sectors, this is no longer true when the symmetry is broken. This makes the appearance of a new family of solutions connecting the two points possible, such that $\lim_{\zeta \rightarrow +\infty} u(\zeta) = A$ and $\lim_{\zeta \rightarrow -\infty} u(\zeta) = B$ (

¹ Notice that this condition is shared with other orbits which do not pass through $u = \infty$ and are therefore *not* separatrix curves. These orbits have been excluded from the plot.

1. \mathcal{PT} deformations of KdV travelling waves

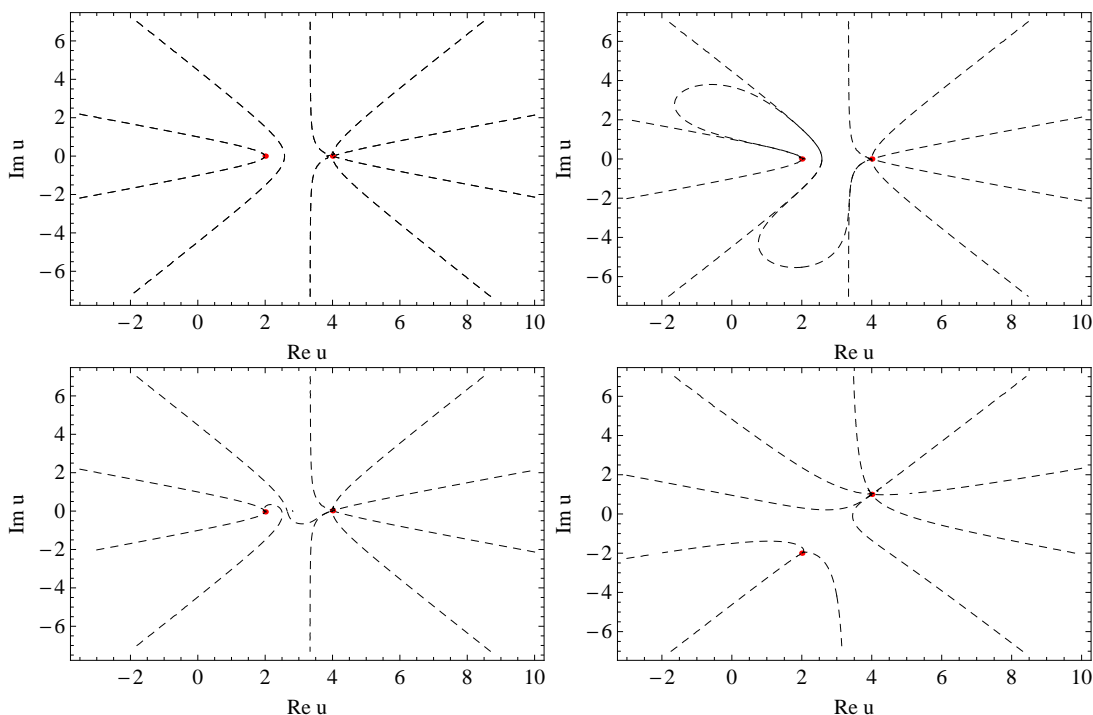


Figure 1.14: The network of separatrix curves for different solutions of the $\mathcal{H}_{-\frac{1}{2}}^+$ model for $c = 1$, $\beta = 3/10$, $\gamma = 3$. The critical points A and B are chosen as: (top left) $A = 4$, $B = 2$; (top right): $A = 4 + \frac{i}{200000}$, $B = 2 - \frac{i}{100000}$; (bottom left): $A = 4 + \frac{i}{50}$, $B = 2 - \frac{i}{25}$; (bottom right): $A = 4 + i$, $B = 2 - 2i$. Notice that the topology of the network corresponding to the first solution (the \mathcal{PT} -symmetric case) differs from the other three and does not allow the existence of orbits connecting A and B .

or $\lim_{\zeta \rightarrow -\infty} u(\zeta) = A$ and $\lim_{\zeta \rightarrow +\infty} u(\zeta) = B$). The new topology of the orbits appears to be preserved for all choices of A with $\text{Im}(A) > 0$.

In Figures 1.15 and 1.16 are illustrated several orbits of the \mathcal{PT} -symmetric solutions and a spontaneously broken solution, respectively. In the latter case, these *kink*-type solutions are clearly visible.

We have observed the same qualitative aspects in the change of topology in other cases, for example the case $\epsilon = -\frac{2}{3}$, very similar but for the different number of sectors, is presented in Cavaglià *et al.* [2011]. However, we remark that, in the case when the two points A and B both correspond to saddle-points, the symmetry breaking has no appreciable qualitative effect on the solutions. This

1. \mathcal{PT} deformations of KdV travelling waves

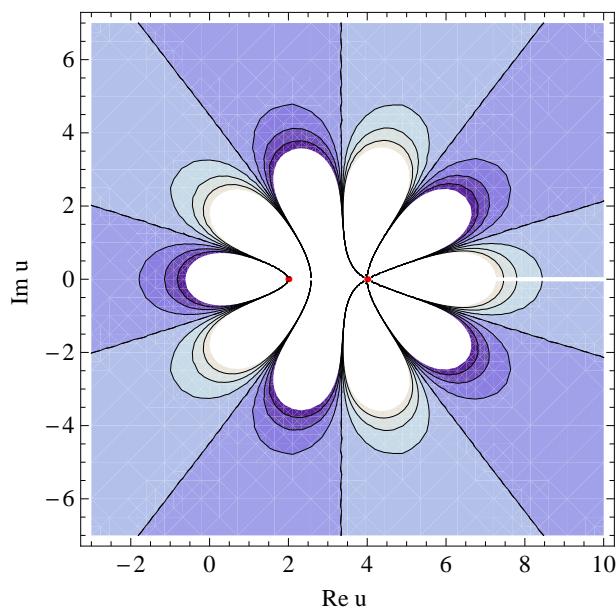


Figure 1.15: Complex \mathcal{PT} -symmetric trigonometric/hyperbolic solutions of the deformed KdV equation with $A = 4, B = 2, c = 1, \beta = 2$ and $\gamma = 3$ for $\mathcal{H}_{-1/2}^+$.

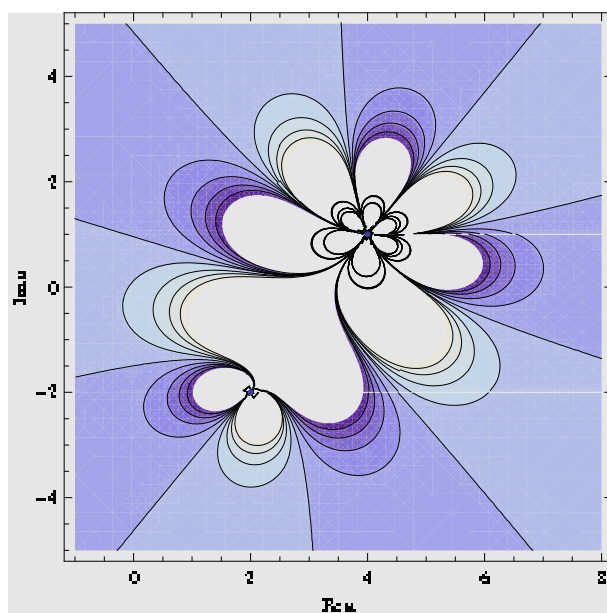


Figure 1.16: Trigonometric/hyperbolic solutions of the deformed KdV equation $\mathcal{H}_{-1/2}^+$ with spontaneously broken \mathcal{PT} -symmetry. The relevant parameters are: $A = 4 + i, B = 2 - 2i, c = 1, \beta = 3/10$ and $\gamma = 3$.

1. \mathcal{PT} deformations of KdV travelling waves

can be seen in Figure 1.17, and is due to the fact that in this case the orbits are not connected to A or B , so that, at least when there are no branch cuts in the complex u -plane, there is not an obvious topological change they might undergo.

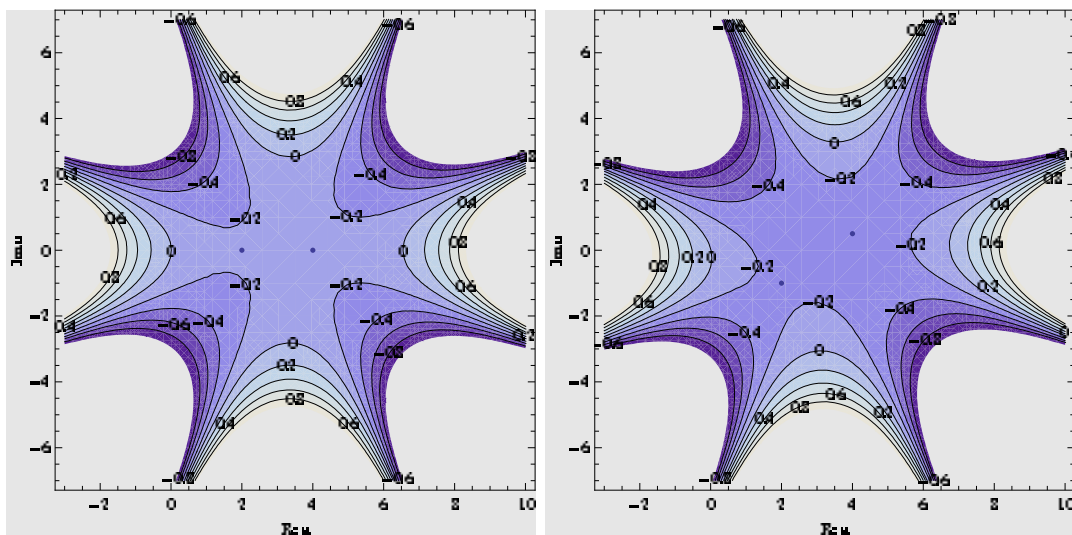


Figure 1.17: Complex \mathcal{PT} -symmetric trigonometric/hyperbolic solutions of the \mathcal{H}_{-2}^+ deformation with $c = 1$, $\beta = 2$ and $\gamma = 3$. In the left panel, the solution is symmetric with $A = 4$, $B = 2$. In the right panel, it is spontaneously broken, with $A = 4 + i/2$, $B = 2 - i$.

1.3.4.3 Elliptic solutions

Finally, we only sketch some general considerations on elliptic solutions. The solution for generic values of $A \neq B \neq C$ is given in the most general case Fring [2007] by the Appel hypergeometric function:

$$\zeta - \zeta_0 = \Lambda_\epsilon (u - A)^{\frac{\epsilon}{1+\epsilon}} F_1 \left(\frac{\epsilon}{1+\epsilon}, \frac{1}{1+\epsilon}, \frac{1}{1+\epsilon}, \frac{1+2\epsilon}{1+\epsilon}; \frac{A-u}{A-B}, \frac{A-u}{A-C} \right) \quad (1.64)$$

with

$$\Lambda_\epsilon = -\frac{i}{\epsilon} \left(-\frac{6\gamma}{\beta(A-B)^2} \right)^{\frac{1}{1+\epsilon}} (1+\epsilon)^{\frac{\epsilon}{1+\epsilon}}. \quad (1.65)$$

1. \mathcal{PT} deformations of KdV travelling waves

Again, the local behaviour around these three points depends on the value of ϵ , and the phase space is divided into sectors by separatrix lines. A few case studies suggest that a connection between \mathcal{PT} -symmetry breaking and the change in the topology of the orbits, analogous to the one reported in the previous section.

1.3.5 Deformations of the KdV equation II: the \mathcal{PT}_- -symmetric deformation

Let us now consider briefly also the second type of deformation. The deformed equation (1.35) can be rewritten as:

$$\dot{u}^2 = \lambda_{\epsilon,-} Q_{\epsilon,-}(u), \quad (1.66)$$

where

$$\lambda_{\epsilon,-} = -\frac{2\beta i^\epsilon}{\gamma(1+\epsilon)(2+\epsilon)} \quad (1.67)$$

and we have denoted:

$$Q_{\epsilon,-}(u) := \frac{2}{\gamma} \left(\kappa_2 + \kappa_1 u + \frac{c}{2} u^2 - \beta \frac{i^\epsilon}{(1+\epsilon)(2+\epsilon)} u^{2+\epsilon} \right) \quad (1.68)$$

If $\epsilon := M \in \mathbb{N}$, for example, $Q_{M,-}(u)$ is a $M+2$ -th order polynomial whose roots are all distinct apart from at most three of them, since their positions depend on only two parameters κ_1 and κ_2 . The most general factorisation is therefore $Q_{M,-}(u) := (u - A_1)^k \prod_{i=1}^{M+2-k} (u - A_{i+1})$, with $k = 1, 2, 3$ or $Q_{M,-}(u) := (u - A_1)^2 (u - A_2)^2 \prod_{i=1}^{M+2-4} (u - A_{i+2})$. Naturally, there are infinitely many possibilities. We expect that, at least for $\epsilon \in \mathbb{N}$ when the orbits cannot cross over to different Riemann sheets¹, the types of orbits would not be too dissimilar from the ones studied in the case of the standard, undeformed KdV, since also in the present case all the roots correspond to either turning points or fixed points. In the following we will limit ourselves to showing an example for $\epsilon = 4$.

However, we remark that at least one class of solutions can be found in closed form for all values of ϵ : they are the solitary wave solutions of the generalised

¹ For noninteger ϵ the behaviour could be much more complicated, as shown by the studies of Bender and Boettcher.

1. \mathcal{PT} deformations of KdV travelling waves

KdV equation, obtained by taking $\kappa_1 = \kappa_2 = 0$:

$$u(\zeta) = \left(\frac{c(\varepsilon + 1)(\varepsilon + 2)}{i^\varepsilon \beta \left[\cosh \left(\frac{\sqrt{c\varepsilon}(\zeta - \zeta_0)}{\sqrt{\gamma}} \right) + 1 \right]} \right)^{1/\varepsilon}. \quad (1.69)$$

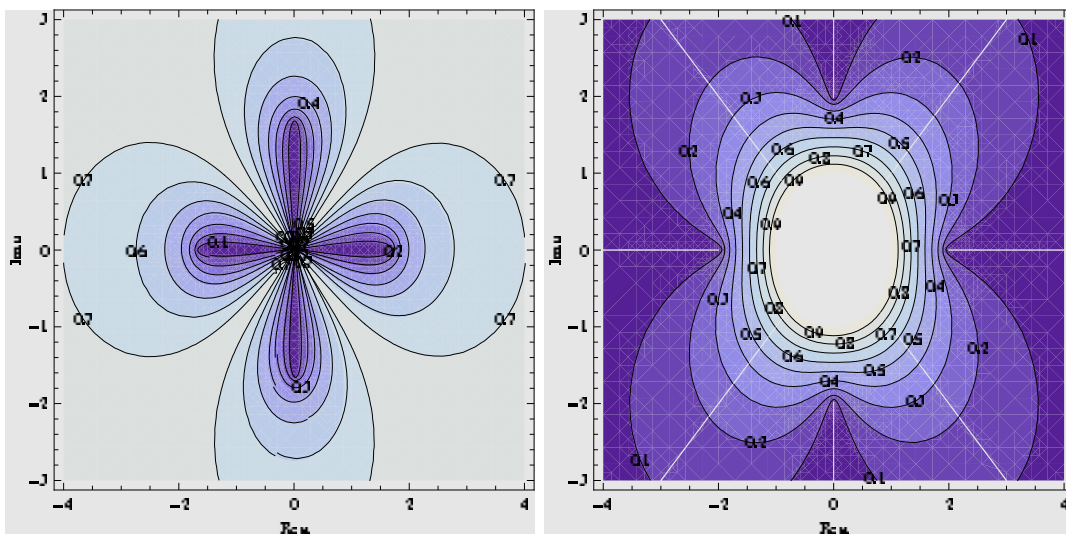


Figure 1.18: \mathcal{PT} -symmetric solutions for \mathcal{H}_4^- : (a) Star node at the origin for $c = 1$, $\beta = 2$, $\gamma = 1$; (b) centre at the origin for $c = 1$, $\beta = 1$, $\gamma = -1$. In both cases there are four turning points at $u = \pm B$, $\pm iB$, with $B = (15/2)^{1/4}$.

1.3.5.1 An example with $\varepsilon = 4$

In this case the polynomial of the right hand side of (1.66) is of sixth order. We present here just one very symmetric solution by assuming a factorization of the form $Q(u) = u^2(u^2 - B^2)(u^2 - C^2)$, which is achieved with the simple choice

$$\kappa_1 = \kappa_2 = 0, \quad B = iC \quad \text{and} \quad C^4 = \frac{15c}{\beta}. \quad (1.70)$$

In particular, for this factorisation the solution is given explicitly by (1.69). This family of solutions has a fixed point at $u = 0$ and four turning points at $u = \pm A$, $u = \pm B$: except for the number of turning points, the phase portrait look very similar to that of the undeformed KdV equation, but here there are

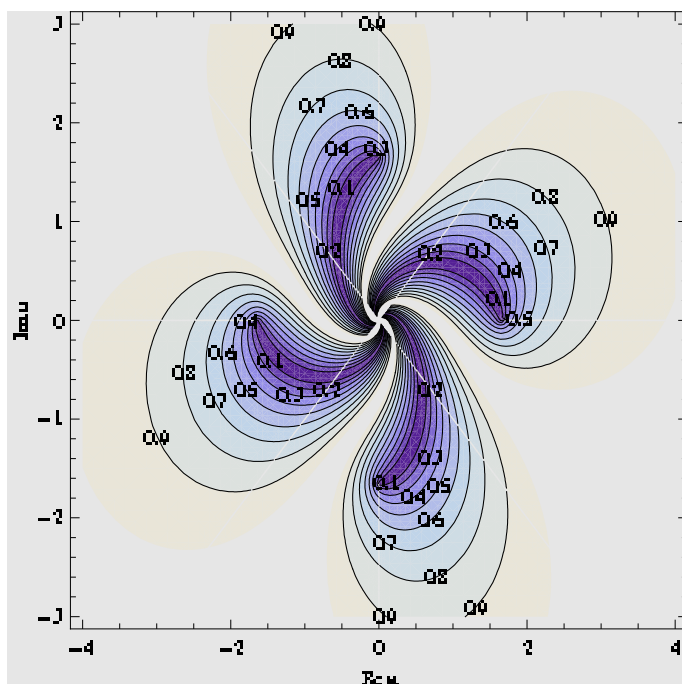


Figure 1.19: Broken \mathcal{PT} -symmetry for the \mathcal{H}_4^- model: these solutions spiral around a focus at $u = 0$, accompanied by four turning points at $u = \pm B, \pm iB$, with $B = (15/2)^{1/4}$. The parameters were chosen as $c = 1$, $\beta = 2$, $\gamma = 1 + i3$.

four distinct families of solitary waves. The behaviour around the fixed point can be studied, just as was done in Section 1.3.3.2, by computing the eigenvalues for small linear perturbations around $u = 0$, which are given by

$$j_1 = \pm i\sqrt{\lambda_{4,-}}B^2, \quad j_2 = (j_1)^*, \quad (1.71)$$

where $\lambda_{4,-} = -\frac{\beta}{15\gamma}$.

Therefore, if we follow the \mathcal{PT}_- -symmetric prescription $\gamma \in \mathbb{R}$, $\beta \in i\mathbb{R}$, we obtain two real eigenvalues and therefore a star node at $u = 0$. This corresponds to solitary wave solutions, and the phase portrait is shown in Figure 1.18 (left panel). In this highly symmetric case these solutions are invariant under reflection across both the real and imaginary axis. The same happens if we take $\gamma \in \mathbb{R}$, $\beta \in \mathbb{R}$, leading to $j_1 \in i\mathbb{R}$ and therefore to a center at $u = 0$ (see Figure 1.18, right panel). In the most generic case with no symmetry, in particular for $\text{Im}\gamma \neq 0$, the fixed point will turn into a focus, namely an open orbit (see Figure 1.19). This

is the same connection between the loss of \mathcal{PT} -symmetry and the periodicity of the orbit observed in the KdV equation.

1.4 Complex deformations of soliton solutions

In this section we come back to the KdV equation and consider two-soliton solutions, perhaps the simplest generalization of the travelling wave solutions we have been considering so far.

They depend on four parameters, the momenta p_1 and p_2 of the two constituent solitons and two phases ϕ_1 and ϕ_2 parametrizing their initial separation. In the spirit of the previous sections, we will make these parameters complex.

Notice that the complex-momentum deformation was not considered before even for the one-soliton solution, since we always focused, for simplicity, on real values for the speed c . The one-soliton solution reads:

$$u(x, t) = \frac{3\gamma p^2}{\beta \cosh^2 \left[\frac{1}{2}(px - \gamma p^3 t + \phi) \right]}, \quad (1.72)$$

with $p := c$ in the previous notations. Interestingly, if we take complex values for c , this is no longer a travelling solution but instead pulsates, resembling a travelling breather. The solution regains its shape after a certain distance Δ_x and certain amount of time Δ_t , namely

$$u(x + \Delta_x, t) = u(x, t + \Delta_t), \quad (1.73)$$

where:

$$\Delta_t = \frac{2\pi \operatorname{Re}(p)}{-|p|^2 \operatorname{Im}(\gamma p^2)}, \quad \Delta_x = \frac{2\pi \operatorname{Re}(\gamma p^3)}{|p|^2 \operatorname{Im}(\gamma p^2)}. \quad (1.74)$$

An example is depicted in Figure 1.20.

The two-soliton solution, first obtained in Gardner *et al.* [1967] via the inverse

1. \mathcal{PT} deformations of KdV travelling waves

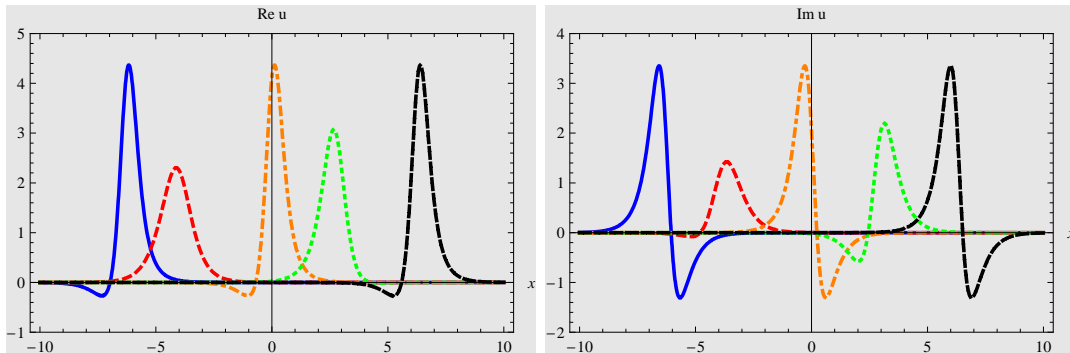


Figure 1.20: Complex spontaneously broken one-soliton solution of the KdV-equation with $\beta = 6$, $\gamma = 1 + i/2$, $p_1 = 2$, $\phi = i0.8$ and $\Delta_t = -\pi/2$ for different times $t = -\pi/2$ solid (blue), $t = -1$ dashed (red), $t = 0$ dasheddot (orange), $t = 0.7$ dotted (green), and $t = \pi/2$ dasheddotdot (black).

scattering method, is

$$u(x, t) = \frac{6\gamma}{\beta} \frac{(p_2^2 - p_1^2) [(p_2^2 - p_1^2) + p_1^2 \cosh(\eta_2) + p_2^2 \cosh(2\eta_2)]}{[(p_1 + p_2) \cosh(\frac{1}{2}(\eta_1 - \eta_2)) + (p_2 - p_1) \cosh(\frac{1}{2}(\eta_1 + \eta_2))]^2}, \quad (1.75)$$

where

$$\eta_i = p_i x - \gamma p_i^3 t + \phi_i, \quad (i = 1, 2). \quad (1.76)$$

The time evolution of this solution, for complex values of the parameters, is illustrated in Figures 1.21 and 1.22 in the u -plane. For large negative time the two-solitons are separated, indicated here by two individual one-soliton solutions touching each other only in the asymptotic point at $u = 0$. In the scattering regime the two solutions merge in a non \mathcal{PT} -symmetric manner until they separate again for large positive time. Their characteristic pulsating frequencies (1.74) can be observed throughout the process, with a slight displacement due to the familiar phase shift in soliton interactions.

Two-soliton complex solutions are considered at a deeper level in Bona & Weissler [2009], in particular in relation with the phenomenon of finite-time blow-up exhibited by the complex KdV equation.

1. \mathcal{PT} deformations of KdV travelling waves

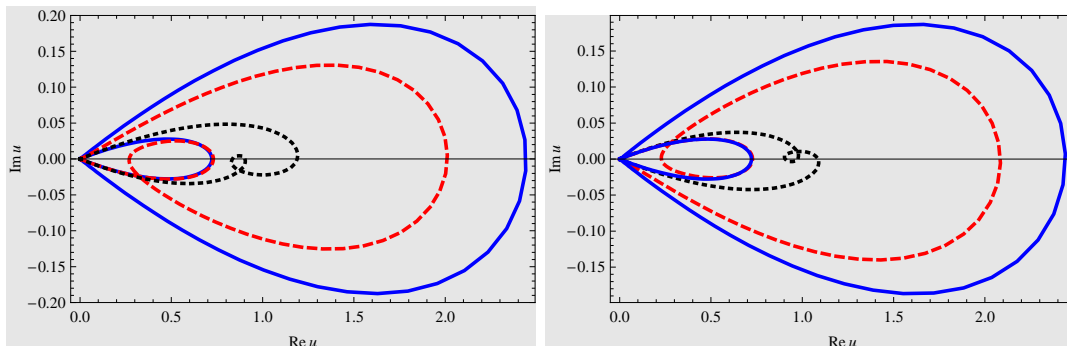


Figure 1.21: \mathcal{PT} -symmetric two-soliton solutions of the KdV equation for $\beta = 6$, $\gamma = 1$, $p_1 = 1.2$, $p_2 = 2.2$, $\phi_1 = i0.1$ and $\phi_2 = i0.2$. Left panel: $t = -2$ solid (blue), $t = -0.2$ dashed (red), $t = 0.2$ dotted (black); right panel: $t = 0.3$ dotted (black), $t = 0.8$ dashed (red), $t = 2.0$ solid (blue).

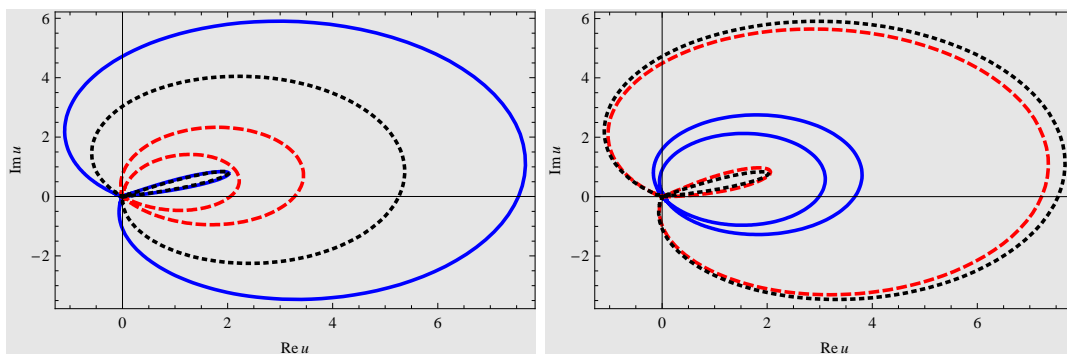


Figure 1.22: Broken \mathcal{PT} -symmetric two-soliton solutions of the KdV equation for $\beta = 6$, $\gamma = 1 + i\pi/8$, $p = 2(2/3)^{1/3}$, $p_2 = 2$, $\phi_1 = i0.1$ and $\phi_2 = i0.2$. Left panel: $t = -4$ solid (blue), $t = -3.5$ dashed (red), $t = -2$ dotted (black); right panel: $t = 0.7$ solid (blue), $t = 2$ dashed (red), $t = 8$ dotted (black). Notice that for this choice of parameters we have $2\Delta_t^1 = 3\Delta_t^2 = 6$. We see that both solitons have almost regained their original shape passing from $t = 2$ to $t = 8$, but for a slight discrepancy due to the well known time delay occurring in soliton scattering.

1.5 Summary of the results of this chapter

In this chapter, which is based on the contents of the paper Cavaglià *et al.* [2011], we have considered many examples of complex travelling wave solutions to the KdV equation and two different \mathcal{PT} deformations of the model.

For the KdV equation, these solutions are obviously well-known, but had

1. \mathcal{PT} deformations of KdV travelling waves

not been previously considered from the present viewpoint. This study confirms the natural expectation that solutions which are not \mathcal{PT} symmetric are in general open, while \mathcal{PT} -symmetric solutions are more regular – they in general correspond to periodic or asymptotically constant solutions; we have also noticed the presence of isolated exceptions to this rule, similar to those observed in Anderson *et al.* [2011].

In Section 1.4, we discussed the analytic continuation of one and two-soliton solutions to complex values of their parameters, making the observation (of which we are unaware in the literature) that, for complex values of the speeds, these solutions acquire a pulsating behaviour.

The deformation that we have denoted as \mathcal{PT}_- was proposed for the first time in this paper. We also provided many new examples of solutions and discussed the general features of a family of deformations – denoted as \mathcal{PT}_+ – which was first introduced in Fring [2007]. We also considered the presence of orbits with broken \mathcal{PT} -symmetry in this family of deformed models and showed that, in the present case, the symmetry breaking can lead to the appearance of orbits with a new, kink-like topology.

Chapter 2

\mathcal{PT} -symmetric deformation of the inviscid Burgers equation

We consider a family of \mathcal{PT} -symmetric deformations of the inviscid Burgers equation in one dimension. The chapter is largely based on the publication Cavaglià & Fring [2012], which completed the analysis Bender & Feinberg [2008] where these models were first investigated. The most interesting aspect of the inviscid Burgers equations is certainly the phenomenon of shock formation. We will discuss in detail how this is affected by the deformation. As compared to Bender & Feinberg [2008], our conclusions are new on the following two points. First, in Bender & Feinberg [2008] it was stated that for $\epsilon \neq (2n + 1)$, $n \in \mathbb{Z}$, no singularities are formed in the evolution of a real initial profile. However, this conclusion was based on an incorrect argument, and by using the method of complex characteristics, we show that singularities can be formed for any value of ϵ . Secondly, we observed that for all $\epsilon > 1$ the nature of the singularities changes. They are no longer gradient singularities as in the undeformed case, but the break-up occurs via a blow-up of the second derivative of the solution. In some specific cases, this leads to the formation of peaked solutions, which are continuous for all times and have a jump in their first derivative, rather than shock solutions. This abrupt change in the nature of the solutions indicates that the \mathcal{PT} deformation is not smooth around the $\epsilon = 1$ case.

2.1 The undeformed case

2.1.1 Inviscid Burgers equation, characteristics and gradient catastrophe

The inviscid Burgers equation is a fundamental model of nonlinear transport, applicable to a variety of situations ranging from traffic flow to gas dynamics. In the one-dimensional scalar case to which we restrict, it reads

$$w_t + ww_x = 0. \tag{2.1}$$

It is well known that for all smooth and bounded real initial conditions, the solution develops a singularity in finite time, characterized by the localized divergence of the gradient of the solution. This happens due to a crossing of the characteristic lines along which the solution is transported. Let us briefly recall the method of characteristics. This is based on realizing that (2.1) implies that the solution is constant along the curves $(t, x(t))$ in the tx -plane satisfying

$$\frac{dx}{dt} = w(x(t), t) = w_0(x(0)), \tag{2.2}$$

where $w_0(y) \equiv w(y, 0)$. The solutions to this equation are a family of lines

$$x(t) = \gamma(x_0, t) = x_0 + w_0(x_0) t, \tag{2.3}$$

parametrised by $x_0 := x(0)$ and are called *characteristic lines* or simply *characteristics*. The solution to (2.1) is defined implicitly as

$$w(x, t) = w_0(x_0), \quad x = \gamma(x_0, t). \tag{2.4}$$

The solution remains smooth as long as no two characteristics cross. However, it undergoes a progressive steepening due to the fact that the equation is nonlinear and therefore the characteristics are not parallel. Computing the gradient of the

2. \mathcal{PT} deformation of the inviscid Burgers equation

solution one finds

$$w_x(x, t) = \frac{w'_0(x_0)}{\frac{\partial}{\partial x_0}\gamma(x_0, t)} = \frac{w'_0(x_0)}{1 + w'_0(x_0)t}. \quad (2.5)$$

This equation shows that, under every smooth initial conditions, the gradient blows up at a critical time t_s defined by

$$0 < t_s = \min_{x_0} \frac{-1}{w'_0(x_0)}. \quad (2.6)$$

Denoting with x_0^{\min} the position where the minimum is attained, one has

$$\lim_{t \rightarrow t_s^-} w_x(x_s, t) = \infty, \quad (2.7)$$

where $x_s = \gamma(x_0^{\min}, t)$. The singularity (2.7) is known as *gradient catastrophe*, or as the formation of a *shock*. Prominent examples of this phenomenon in nature are the breaking of water waves or the formation of pressure shocks in high temperature gas or plasma. The equation (2.1) is an extremely simple mathematical model but still captures interesting universal features of this class of singularities. We consider some of these aspects in the next section. After the formation of the singularity, the method of characteristics defines a multi-valued profile. An example is shown in Figure 2.1. The occurrence of multi-valued solutions has a clear physical meaning if the solution is thought to represent the profile of a breaking wave; in other contexts, to retain the applicability of the model it is necessary to introduce single-valued weak solutions. We briefly recall the basic definitions in Section 2.1.3. In the next section we will concentrate on some complex analytic aspects of the singularity.

2.1.2 Singularities as branch points

A very illuminating viewpoint on the gradient catastrophe was presented in Bessis & Fournier [1984], where it was discovered that it is the result of a square root singularity moving from the complex x -plane to the real axis. In a non-rigorous way, this can be seen as follows. The equation expressing the crossing of charac-

2. \mathcal{PT} deformation of the inviscid Burgers equation

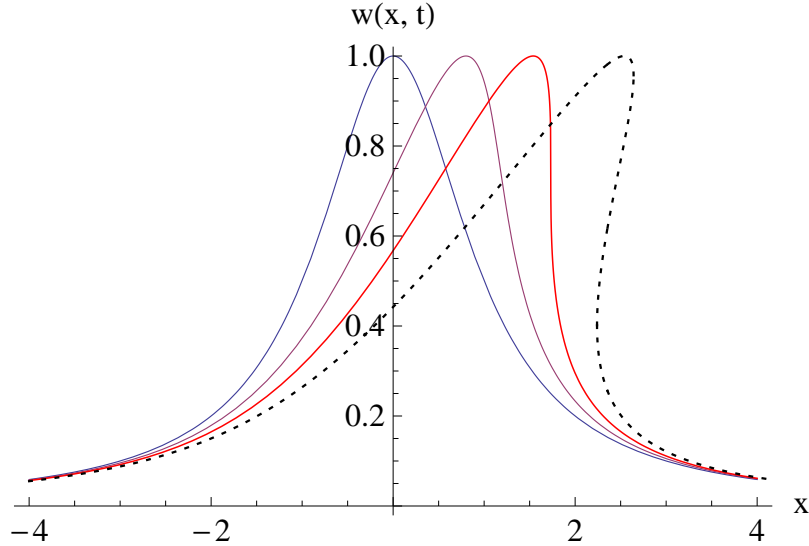


Figure 2.1: Snapshots of the solution $w(x, t)$ to the inviscid Burgers equation with initial condition $w(x, 0) = \frac{1}{1+x^2}$. The solid lines correspond to $t = 0$, $t = 0.8$ and $t = t_s = \frac{8}{3\sqrt{3}} \simeq 1.5396$ (the crest of the wave moves rightwards for increasing times). The dotted multi-valued profile corresponds to $t = t_s + 1$.

teristics is

$$\frac{\partial}{\partial x_0} \gamma(x_0, t) = 0. \quad (2.8)$$

For $t < t_s$, (2.8) this equation normally has a discrete set of solutions, for strictly complex values of x_0 . Let us denote one of these solutions as $x_0 = x_*(t)$, so that $\frac{\partial}{\partial x_0} \gamma(x_0, t) \Big|_{x_0=x_*(t)} = 0$, and let us make the natural assumption that these zeros are single. Then, neglecting higher order terms, in a neighbourhood of $x_0 \sim x_*$ and for fixed time t we have:

$$\gamma(x_0, t) \sim x_*(t) + t w_0(x_*(t)) + t \frac{w_0''(x_*(t))}{2} (x_0 - x_*(t))^2, \quad (2.9)$$

and this implies that

$$x_0(x, t) \sim x_*(t) + \sqrt{\frac{2}{t w_0''(x_*(t))}} (x - z(t))^{\frac{1}{2}} \quad \text{for } x \sim z(t), \quad (2.10)$$

2. \mathcal{PT} deformation of the inviscid Burgers equation

where $z(t) \equiv x_*(t) + t w_0(x_*(t))$. This shows that the solution, defined by $w(x, t) = w_0(x_0(x, t))$, has a square root branch point at the point $x = z(t)$ in the complex x -plane. For $t < t_c$, all such singularities lie far from the real axis in the complex x -plane. Exactly at $t = t_c$, one pair of complex conjugate singularities reaches the real x -axis, causing the gradient catastrophe. The collision of two square-root branch points produces the following universal behaviour at the point of singularity:

$$w(x, t) \sim w(x_s, t_s) + O(x - x_s)^{\frac{1}{3}}. \quad (2.11)$$

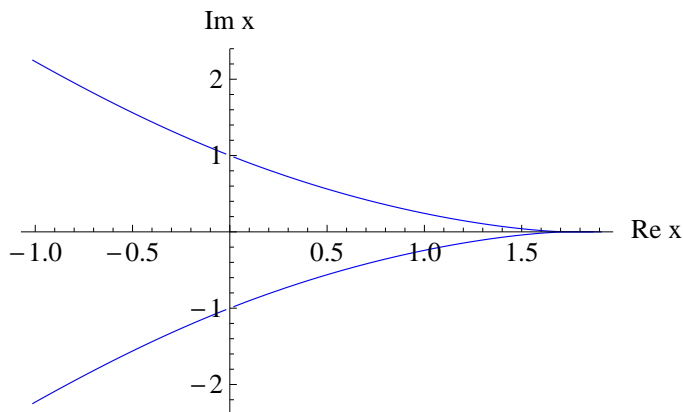


Figure 2.2: Trajectories traced in the complex x -plane by the square root branch points of the solution of (2.1) with initial condition $w(x, 0) = \frac{1}{1+x^2}$. There are four distinct trajectories, all traced for t in the interval $t \in [0.0001, 1.75]$. We observe that two singularities emerge from each of the two poles $x = \pm i$ at $t = 0^+$. One pair of complex conjugate singularities moves off in the in the complex plane, while the other two singularities reach the real axis simultaneously at $t = t_s = \frac{8}{3\sqrt{3}}$. They remain confined to the real axis for $t > t_s$.

An example is shown in Figure 2.2, where we plot part of the trajectories traced by the singularities of the solution with initial condition $u(x, 0) = \frac{1}{1+x^2}$. In this example there are four branch points, which emerge from the two poles $x = \pm i$ at $t = 0^+$. The trajectories shown in the Figure were obtained simply by solving (2.8) and then mapping the four solutions to the x -plane.

¹ In other cases, the singularities lie at complex infinity at $t = 0^+$.

2. \mathcal{PT} deformation of the inviscid Burgers equation

For $t > t_s$, one sees that the two singularities that have collided on the real axis split, producing a multi-valued profile (see for example the dashed profile in Figure 2.1). At the points $x_b(t)$ where two branches merge, one has the algebraic behaviour

$$w(x, t) \sim w(x_b, t) + O(x - x_b(t))^{\frac{1}{2}}, \quad (2.12)$$

for $x \sim x_b(t)$, $t > t_s$.

Notice that throughout this section we have been concerned with real solutions of the real Burgers equation. In the complex case, singularities would cross the real axis individually causing the breaking of the profile. We will discuss this more in detail in Section 2.2.

2.1.3 Shocks and weak solutions

In many applications of nonlinear transport equations, the physical interpretation requires the solution to be single-valued. In gas dynamics, for instance, $w(x, t)$ represents the concentration of the gas and therefore should be a real positive function. After the singularity, one can restore single-valuedness by cutting out part of the multi-valued profile. The resulting profile has a discontinuity, known as a shock. While these discontinuous solutions are certainly an idealization, they can be used as a very good approximation to the very thin shock layers occurring in nature. An indication of the naturality of this construction is that shock solutions can be obtained from the ordinary, smooth solutions of the Burgers equation:

$$w_t + ww_x = \eta w_{xx}, \quad \eta > 0 \quad (2.13)$$

in the zero-viscosity limit $\eta \rightarrow 0$. Naturally, it is crucial that a physically meaningful criterion is used to define the position of the shock front. This is done by requiring the local validity of a conservation law. Normally, since $w(x, t)$ represents a density, one is interested in ensuring the conservation of

$$\int_{-\infty}^{\infty} w(y, t) dy. \quad (2.14)$$

2. \mathcal{PT} deformation of the inviscid Burgers equation

This quantity represents the area shaded by the profile of the solution. After a singularity has formed, the conservation law still holds, provided one considers the area shaded by the (unique) multi-valued profile obtained by analytic continuation. The requirement that the area is preserved after introducing a discontinuity gives a clear prescription on the position of the shock front (see Whitham [2011] for an illustration). Let us mention, referring the reader to Whitham [2011] for more details, that this definition can be easily adapted to a more general conservation law, and that it can be translated into a differential equation, the Rankine-Hugoniot condition, determining the position of the shock discontinuity. Finally, we remind the reader that one could give a precise mathematical meaning to discontinuous solutions in the sense of weak solutions. For this definition and for a much deeper treatment of shock phenomena, including the important concept of entropy which we did not attempt to cover in this overview, see Whitham [2011].

2.2 Deformed case ($\epsilon > 1$)

The family of deformations considered by Bender and Feinberg is

$$u_t - iu(iu_x)^\epsilon = 0. \quad (2.15)$$

Let us summarise their findings.

First, they showed that the solution to (2.15) is given implicitly by

$$u(x, t) = U^{(\epsilon)}(x_0, t) := \frac{1}{\epsilon} (G(x_0) - i\epsilon t)^{\frac{\epsilon-1}{\epsilon}} W_0^{(\epsilon)}(x_0), \quad (2.16)$$

where

$$G(x_0) := (iu_0'(x_0))^{-\epsilon}, \quad W_0^{(\epsilon)}(x_0) := \epsilon u_0(x_0) (iu_0'(x_0))^{\epsilon-1}, \quad (2.17)$$

and the auxiliary parameter x_0 is determined by the characteristic equation

$$x = \gamma^{(\epsilon)}(x_0, t) := x_0 + W_0^{(\epsilon)}(x_0)t, \quad (2.18)$$

2. \mathcal{PT} deformation of the inviscid Burgers equation

with $u_0(y) \equiv u(y, 0)$. In Bender & Feinberg [2008], this result was derived by using the method of characteristic strips, a generalization of the method of characteristics to the case of non-quasilinear equations such as (2.15). This solution can be easily checked by explicit computation. Notice that (2.18) represents a family of deformed characteristic lines, and for $\epsilon = 1$ the solution reduces precisely to (2.4). However, for $\epsilon > 1$, the solution is no longer constant along the characteristics, as (2.16) is explicitly time-dependent.

It was subsequently realised in Curtright & Fairlie [2008] that there exists a simple transformation relating (2.15) to the undeformed inviscid Burgers equation (2.1). In fact, setting

$$w^{(\epsilon)}(x, t) \equiv \epsilon u(x, t)(iu_x(x, t))^{\epsilon-1}, \quad (2.19)$$

one finds that, at least formally, if $u(x, t)$ is a solution to (2.15) then $w(x, t)$ satisfies the undeformed model (2.1).¹ In this light the solution (2.16)-(2.17) becomes much more transparent, since the function W_0 appearing in (2.17) plays the rôle of initial condition $W_0^{(\epsilon)}(x) = w^{(\epsilon)}(x, 0)$ and (2.18) are simply the characteristic lines of this simpler, undeformed problem.

Finally, we report a useful expression, obtained by differentiating (2.16):

$$u_x(x, t) = \frac{1}{(G(x_0) - i\epsilon t)^{\frac{1}{\epsilon}}} = \frac{u'_0(x_0)}{(1 + i^{\epsilon-1}\epsilon(u'_0(x_0))^{\epsilon} t)^{\frac{1}{\epsilon}}}. \quad (2.20)$$

2.2.1 Singularities

In Bender & Feinberg [2008] the formation of singularities was also addressed. More precisely, in this section we are considering singularities related to the crossing of the characteristics (2.18), therefore associated to solutions of the equation

¹ It is, furthermore, easy to generalise this map to the slightly more general case

$$u_t - if(u)(iu_x)^{\epsilon},$$

in this case u is related to a solution $w(x, t)$ of (2.1) by

$$w^{(\epsilon)}(x, t) \equiv \epsilon f(u)(iu_x)^{\epsilon-1}.$$

This modification does not add much to the qualitative aspects of the problem.

2. \mathcal{PT} deformation of the inviscid Burgers equation

$1 + \frac{d}{dx_0} W_0^{(\epsilon)}(x_0)t = 0$. We will comment later on a different kind of singularities, which are related to solutions of $G(x_0) - i\epsilon t = 0$.

Similar to the undeformed case, the map (2.18) is degenerate whenever $\frac{d}{dx_0} W_0^{(\epsilon)}(x_0) = -\frac{1}{t}$, and the generalisation of (2.6) appears to suggest that the time of formation of the first singularity t_s is given by

$$t_s^{(\epsilon)} = \min_{x_0 \in \mathbb{R}} \frac{-1}{\frac{d}{dx_0} W_0^{(\epsilon)}(x_0)} = \min_{x_0} \frac{-1}{\epsilon \frac{d}{dx_0} (u_0(x_0)(iu_0'(x_0))^{\epsilon-1})}. \quad (2.21)$$

This is the expression present in Bender & Feinberg [2008]. Notice that, for a real initial condition $u_0(x)$, (2.21) can have a solution $t_s \in \mathbb{R}^+$ only for $\epsilon = (2n + 1)$, $n \in \mathbb{Z}$. Therefore, Bender and Feinberg argued that, except for these special values of ϵ , no singularities are formed in the evolution of a real initial condition. By allowing the system to become complex and avoid the singularity, the deformation would then have a smoothing effect.

However, as observed in Cavaglià *et al.* [2011], this conclusion is not correct. The reason is that, for generic values of ϵ , the characteristic lines (2.18) become complex and the simple expression (2.21) needs to be modified. The method of complex characteristics has appeared before: in fact, the inviscid Burgers equation with complex initial data has a wide range of important applications, e.g. in the study of geostrophic flows Baker *et al.* [1996], Chae *et al.* [2005] and even random matrix models Matytsin [1994]. The only difference from the real case is that, for $t > 0$, the inverse image of $x \in \mathbb{R}$ under the characteristic map (2.18) is in general complex $x_0 \in \mathbb{C}$; the solution is still given by (2.16).¹ The singularity time t_s can be found as

$$t_s^{(\epsilon)} = \min_{x_0^*} \frac{-1}{\frac{d}{dx_0} W_0^{(\epsilon)}(x_0^*)}, \quad (2.22)$$

¹ Notice that we are implicitly assuming that the functions $W_0^{(\epsilon)}$ and G in (2.16) are analytic, so that they can be continued unambiguously to complex values of the arguments. This assumption can probably be relaxed but this is not important for the present discussion.

2. \mathcal{PT} deformation of the inviscid Burgers equation

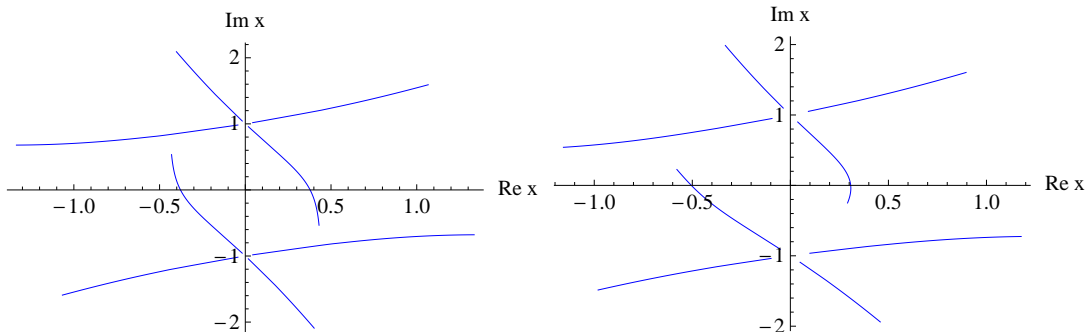


Figure 2.3: In the left panel, trajectories traced in the complex x -plane by the square-root branch points of the $\epsilon = 2$ solution with $u_0(x) = \frac{1}{1+x^2}$. In the right panel, we consider the $\epsilon = 2.2$ deformation with the same initial condition (in this case, we are showing only some of the singularities, the ones corresponding to the principal branch in the definition of $W_0^{(\epsilon)}$). In both plots the trajectories are shown for $t \in [10^{-6}, 0.36]$; the arrow of time is such that the square-root branch points move out of the poles at $x = \pm i$ as t increases from $t = 0^+$.

where x_0^* are all possible solutions of the equations

$$0 < \frac{-1}{\left. \frac{d}{dx_0} W_0^{(\epsilon)}(x_0) \right|_{x_0=x_0^*}}, \quad (2.23)$$

$$0 = \operatorname{Im} \left[x_0^* - \frac{W_0^{(\epsilon)}(x_0^*)}{\left. \frac{d}{dx_0} W_0^{(\epsilon)}(x_0) \right|_{x_0=x_0^*}} \right]. \quad (2.24)$$

The first condition is simply $t_s > 0$, while the second is the requirement that the image of x_0^* crosses the real axis. These are two real equations, and therefore are expected to have a discrete set of solutions $x_0^* \in \mathbb{C}$. This shows that singularities are possible for any value of ϵ and not only for $\epsilon \in 2\mathbb{N} + 1$. We have studied a number of examples, considering the initial condition $u_0(x) = \frac{1}{1+x^2}$ and different values of ϵ , see for example Figures 2.3 and 2.4. These plots are the deformed version of Figure 2.2. Again the singularities emerge from the two poles at $t = 0^+$, their number depending continuously on ϵ^1 . One can notice immediately that

¹ For $u_0(x) = \frac{1}{1+x^2}$ and $\epsilon = m \in \mathbb{N}$, we have $4m$ singular points. For irrational values of ϵ the situation is more complicated since, due to (2.17), the point $x_0 = 0$ is an infinite genus branch point of the characteristic map, connecting infinitely many sheets. However, the number of singularities on the first, physical Riemann sheet changes continuously.

2. \mathcal{PT} deformation of the inviscid Burgers equation

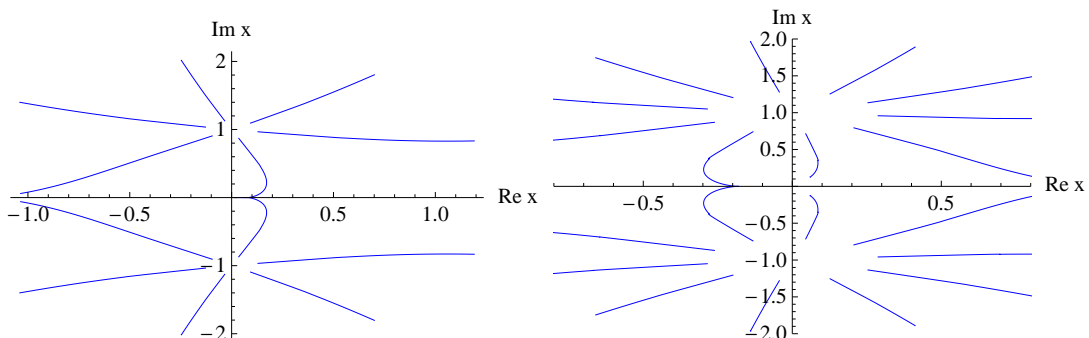


Figure 2.4: Trajectories of square root branch points in the complex x -plane, for the $\epsilon = 3$ (left) and $\epsilon = 5$ deformation (right), where the initial condition was chosen again as $u_0(x) = \frac{1}{1+x^2}$. In both plots the trajectories correspond to $t \in [10^{-6}, 0.4]$, and move out of the poles at $x = \pm i$ as time progresses. One can see that, since the solution is real, singularities arrive on the real axis in pairs and afterwards remain confined there.

ϵ	$t_{s,1}$	$t_{s,2}$	$x_{s,1}$	$x_{s,2}$
3	0.311791	0.644466	0.0770262	-1.21712
5	0.394011	0.662872	-0.18255	1.05226
7	0.594697	0.913866	0.241058	-0.970114
9	0.997223	1.45053	-0.279227	0.919109

Table 2.1: Time and location at which the first and the second singularities are formed for some selected values of ϵ , in the case of $u_0 = \frac{1}{1+x^2}$.

there are crossings of the real axis at a finite time t_s (one can see in Table 2.1 the time and position of the first two crossings for some values of ϵ). As one can see in Figure 2.4, the cases $\epsilon = (2n + 1)$, $n \in \mathbb{R}$ are distinguished by the reality of the solution: for these special values, singularities arrive at the same point on the real axis in pairs and remain confined there for $t > t_s$. However, singularities do occur also for other values of ϵ .

Curvature blow-up In Cavaglià & Fring [2012] it was also observed that, for $\epsilon > 1$ and provided that $u \neq 0$ in a neighbourhood of the singularity, it no longer corresponds to a gradient catastrophe. Instead, u_x remains finite while the *second* derivative u_{xx} blows up. This can be seen very clearly from (2.19). Differentiating

2. \mathcal{PT} deformation of the inviscid Burgers equation

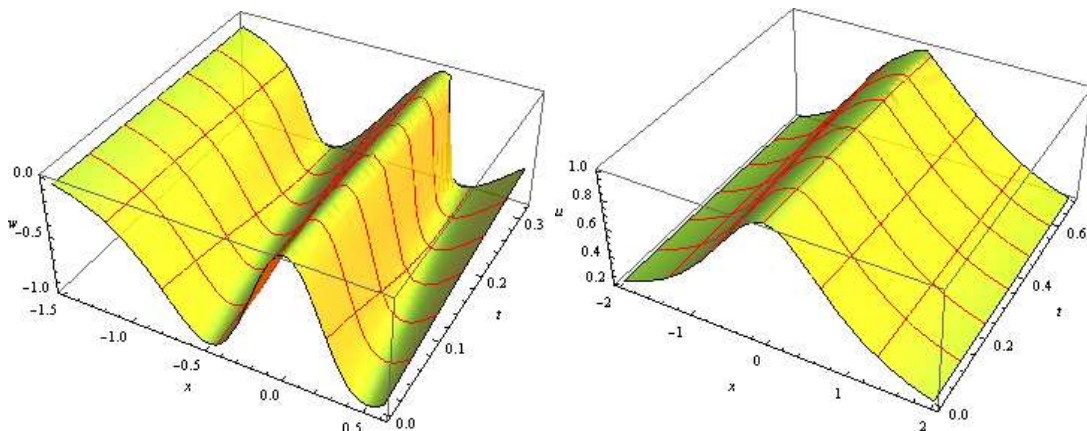


Figure 2.5: *Left panel:* space-time plot of (2.1) with initial condition $w_0(x) = W_0^{(3)}(x)$ defined by (2.17) with $\epsilon = 3$, $u_0(x) = \frac{1}{1+x^2}$, for $0 < t < t_s$. *Right panel:* the corresponding solution of the $\epsilon = 3$ -deformed model, in the same time interval. One can see that, as $t \rightarrow t_s^-$, $w_x^{(\epsilon)} \rightarrow \infty$, while for u this appears as $u_{xx} \rightarrow \infty$.

this expression one finds:

$$(iu_x(x, t))^{\epsilon-1} = \frac{1}{\epsilon u(x, t)} w^{(\epsilon)}(x, t), \quad (2.25)$$

$$u_{xx}(x, t) = i^{\epsilon-1} \frac{(u(x, t)w_x^{(\epsilon)}(x, t) - u_x(x, t)w^{(\epsilon)}(x, t))}{\epsilon(\epsilon-1)u^2(x, t)(u_x(x, t))^{\epsilon-2}}, \quad (2.26)$$

where $w^{(\epsilon)}(x, t)$ is the solution of the inviscid Burgers equation with $w^{(\epsilon)}(y, 0) = W_0^{(\epsilon)}(y)$. As $t \rightarrow t_s^-$, we know that $w^{(\epsilon)}(x, t)$ remains regular while $w_x^{(\epsilon)}(x_s, t) \rightarrow \infty$. This implies that, provided $u(x, t) \neq 0$ in a neighbourhood of (x_s, t_s) ,

$$\lim_{t \rightarrow t_s} u_x(x_s, t) < \infty, \quad \lim_{t \rightarrow t_s} u_{xx}(x_s, t) = \infty. \quad (2.27)$$

This is illustrated in Figures 2.5, 2.6 and 2.7.

Algebraic degree We have found that the points $\epsilon > 1$ behave rather differently from the undeformed case. This is confirmed by the algebraic degree of these singularities in the x -plane: while for $\epsilon = 1$ they are square-root branch points of the solution, for $\epsilon > 1$ they correspond in general to branch points of

2. \mathcal{PT} deformation of the inviscid Burgers equation

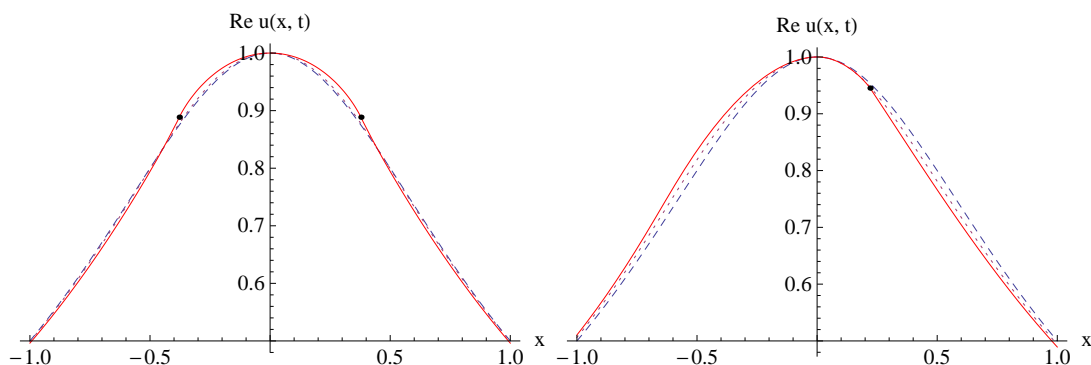


Figure 2.6: Left: solution of the $\epsilon = 2$ -deformed inviscid Burgers equation for $u_0(x) = \frac{1}{1+x^2}$ at times $t = 0$ (blue, dashed), $t = 0.1$ (purple, dotted) and at the singularity time $t = t_s \sim 0.191$ (red, solid). Right: solution of the $\epsilon = 5/2$ -model with the same initial condition, shown for $t = 0$ (blue, dashed), $t = 0.1$ (purple, dotted) and $t = t_s \sim 0.176$ (red, solid). The black dots mark the places where $u_{xx} \rightarrow \infty$.

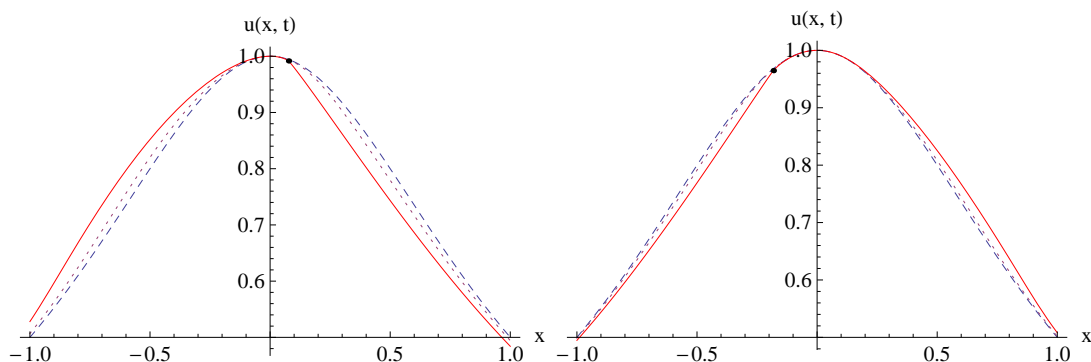


Figure 2.7: Left: solution of the $\epsilon = 3$ -model with $u_0(x) = \frac{1}{1+x^2}$, shown for $t = 0$ (blue, dashed), $t = 0.1$ (purple, dotted) and $t = t_s \sim 0.312$ (red, solid). Right: solution of the $\epsilon = 5$ -model with the same initial condition, shown for $t = 0$ (blue, dashed), $t = 0.1$ (purple, dotted) and $t = t_s \sim 0.395$ (red, solid). The black dots mark the places where $u_{xx} \rightarrow \infty$.

the form $(x - z(t))^{\frac{3}{2}}$. Repeating the argument of Section 2.1.2, we know that, if

$$1 + t \frac{d}{dx_0} W_0^{(\epsilon)}(x_0) \Big|_{x_0=x_*(t)} = 0,$$

2. \mathcal{PT} deformation of the inviscid Burgers equation

then the inverse characteristic map $x \rightarrow x_0$ has a square root branch point at $x = z(t) := \gamma^{(\epsilon)}(x_*(t), t)$, and this means that we can write

$$u(x, t) \sim u(z(t), t) + k \frac{\partial}{\partial x_0} U^{(\epsilon)}(x_0, t) \Big|_{x_0=x_*(t)} (x - z(t))^{\frac{1}{2}} + \mathcal{O} (x - z(t))^{\frac{3}{2}},$$

for $x \sim z(t)$ (where $k = \frac{\sqrt{2}}{\sqrt{t \frac{d^2}{dx_0^2} W_0^{(\epsilon)}(x_*(t))}}$). However, while for $\epsilon = 1$ we had that $\frac{\partial}{\partial x_0} U^{(\epsilon)}(x_0, t)|_{x_0=x_*(t)} \neq 0$, for $\epsilon > 1$ one finds¹

$$\frac{\partial}{\partial x_0} U^{(\epsilon)}(x_0, t)|_{x_0=x_*(t)} = 0, \quad \frac{\partial^2}{\partial x_0^2} U^{(\epsilon)}(x_0, t)|_{x_0=x_*(t)} \neq 0,$$

proving that the singularities have the algebraic degree $\frac{3}{2}$.

Peaked solutions After the time of formation of a singularity, one is usually forced to introduce a jump in the solution. However, for the deformed models we find that in some cases it is possible to define a weak solution for $t > t_s$ that remains continuous but develops a peak, namely a discontinuity in its first derivative. This kind of weak solutions are particularly relevant to some dispersive equations, in which case they can display a solitonic behaviour and are called peakons Camassa & Holm [1993].

In the present case, the construction of these peaked solutions is not always possible, but only if the singularity is the product of two branch points which remain on the real x -axis for all times $t > t_s$. For a real initial condition, this is the case only if $\epsilon = (2n + 1)$, $n \in \mathbb{N}$. In Figure 2.8 we depict an example for $\epsilon = 3$ and $u_0(x) = \frac{1}{1+x^2}$. Notice that for $t > t_s$ the solution has formed a multi-valued profile with a self-crossing: the peak solution is obtained by excluding the closed

¹ In fact from (2.16) one can check that

$$\frac{\partial}{\partial x_0} U^{(\epsilon)}(x_0, t) = \frac{\left(1 + t \frac{d}{dx_0} W_0^{(\epsilon)}(x_0)\right)}{\left(1 + i^{\epsilon-1} \epsilon t (u_0'(x_0))^\epsilon\right)^{\frac{1}{\epsilon}}} u_0'(x_0).$$

The numerator vanishes at $x_0 = x_*(t)$, and therefore the result is zero for all $\epsilon > 1$. For $\epsilon = 1$, instead, this is compensated by the denominator because $W^{(1)}(x) = u_0(x)$.

2. \mathcal{PT} deformation of the inviscid Burgers equation

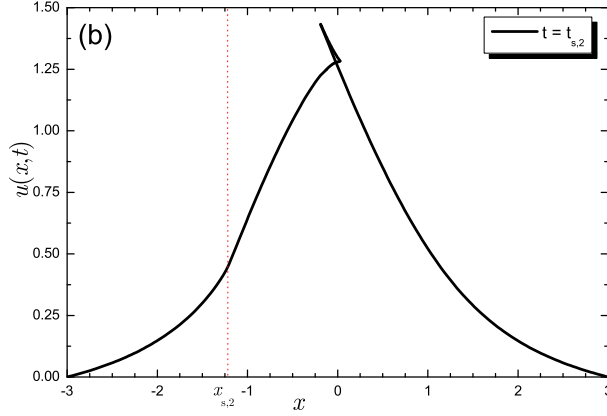


Figure 2.8: Solution of the $\epsilon = 3$ equation with $u_0(x) = \frac{1}{1+x^2}$ at the time of appearance of the second singularity $t = t_{s,2} \sim 0.64 > t_{s,1} \sim 0.31$. The vertical line marks the location $x_{s,2} \sim -1.2$. Notice that, around $x_{s,1} \sim 0.08$, the solution has branched into a multi-valued profile with a self-intersection.

loop in the profile. To gain an insight into the mechanism of formation of the peak, it is useful to consider the relation between the solution $u(x, t)$ and the solution of the undeformed inviscid Burgers equation $w^{(\epsilon)}(x, t)$ defined by (2.19). From equation (2.19), we have that, at least formally,

$$\tilde{u}(x, t) = (\epsilon - 1)^{-1} \epsilon^{\frac{\epsilon-2}{\epsilon-1}} \int^x \tilde{w}(y, t) dy, \quad (2.28)$$

where we have denoted

$$\tilde{w}(x, t) := (w^{(\epsilon)}(x, t))^{\frac{1}{\epsilon-1}}, \quad \tilde{u}(x, t) := iu(x, t)^{\frac{\epsilon}{\epsilon-1}}. \quad (2.29)$$

If $t > t_s$, the profile of $w^{(\epsilon)}(x, t)$ becomes multi-valued, and by making a suitable change of variable, we can use (2.28) to obtain a corresponding multi-valued profile for $u(x, t)$ ¹. For example we can switch to the arc-length parameter s by $dx = ds / \sqrt{1 + \left(\frac{\partial}{\partial x} w^{(\epsilon)}(x, t)\right)^2}$, where one should change the sign of the square root every time one of the branch points is encountered. Let us suppose, for simplicity, that $w^{(\epsilon)}(x, t)$ and $u(x, t)$ are positive, so that the branches in (2.29)

¹ In fact, Figure 2.8 was obtained in this way.

2. \mathcal{PT} deformation of the inviscid Burgers equation

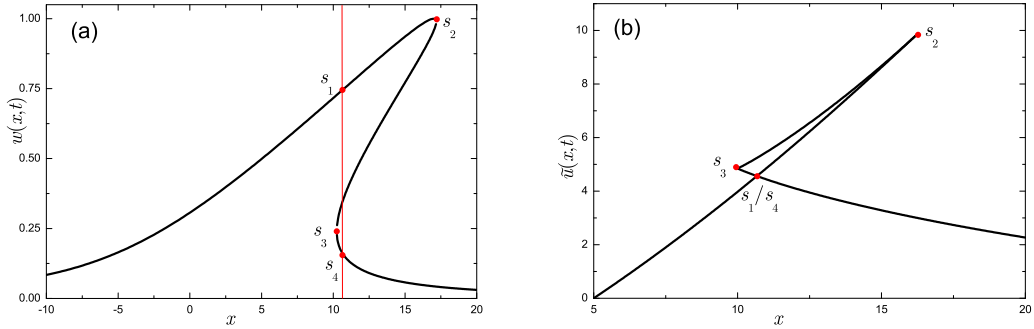


Figure 2.9: These two figures illustrate the mechanism of formation of a self-crossing profile in real solutions of the deformed equation after the breaking time. A multivalued profile of the undeformed equation (*left*) is transformed into a self-intersecting profile for $\tilde{u} = iu^{\frac{\epsilon}{\epsilon-1}}$ (*right*) according to (2.28). The vertical line in the left plot preserves the area shaded by the graph of $\tilde{w} = (w^{(\epsilon)}(x,t))^{\frac{1}{\epsilon-1}}$. It corresponds to a self-intersection for the graph of \tilde{u} since $0 = \left(\int_{s_1}^{s_2} - \int_{s_2}^{s_3} + \int_{s_3}^{s_4} \right) \tilde{w}(x(s),t) \left| \frac{dx}{ds} \right| ds = \tilde{u}(x(s_4),t) - \tilde{u}(x(s_1),t)$.

do not pose additional complications. Then, as illustrated in Figure 2.9, the multi-valued profile for \tilde{u} has a self-intersection precisely at the position where one would trace a shock front for \tilde{w} according to the equal-area prescription explained in Section 2.1.3.

Finally, let us remark that in the more general case where a single branch point crosses the real x -axis, this construction is not possible and the profile would break, for both u and $w^{(\epsilon)}$, after the singularity.

Other kinds of singularities As shown by (2.25), it is possible that the gradient $u_x \rightarrow \infty$ at zeros of u . An example can be seen in Figure 2.10, where we have taken an initial condition $u_0(x) = \frac{x}{1+x^2}$ with an isolated zero at $x = 0$ and we are considering $\epsilon = 3$. Notice that the position of the zero remains fixed: this is a simple consequence of (2.15). An isolated zero also corresponds to a zero of the solution of the undeformed Burgers equation $w^{(\epsilon)}(x,t)$ obtained by applying the map (2.19). A simple scaling analysis of (2.19) shows that, if $w^{(\epsilon)}$ develops a singularity at $t = t_{\text{shock}}$, then correspondingly $u_x \rightarrow \infty$. One can also easily

2. \mathcal{PT} deformation of the inviscid Burgers equation

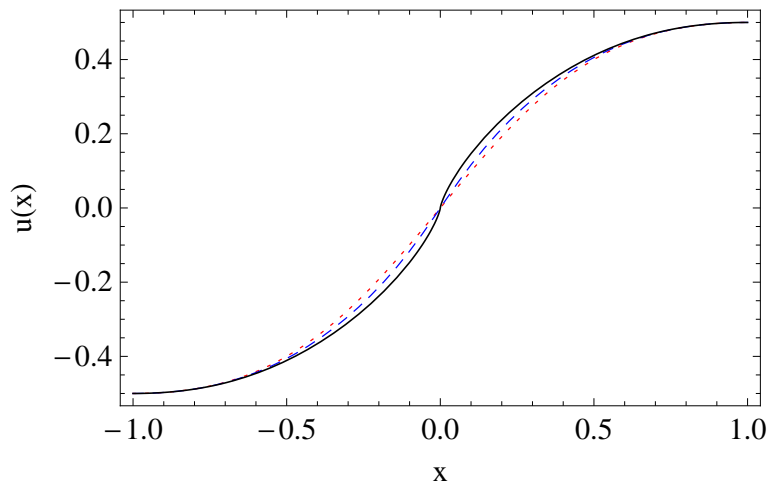


Figure 2.10: Snapshots of the solution of the $\epsilon = 3$ deformation with initial condition $u(x, 0) = \frac{x}{1+x^2}$, shown at time $t = 0$ (red, dotted), $t = 1.5$ (blue, dashed) and $t = t_{\text{shock}} = \frac{1}{3}$ (solid, black).

translate (2.11, 2.12) and find that

$$u(x, t_s) \sim (x - x_s)^{\frac{\alpha + \epsilon - 1}{\epsilon}}, \quad (2.30)$$

where $\alpha = \frac{1}{3}$ or $\frac{1}{2}$ depending on whether w obeys (2.11) or (2.12), respectively.

Finally, we point out that in principle we could have singularities that do not correspond to fixed zeros, but where $u_x \rightarrow \infty$ and $u \rightarrow 0$ simultaneously as a result of the evolution. Expression (2.20) shows that such singularities would correspond to solutions of the equation

$$(G(x_0) - i\epsilon t) = 0, \quad (2.31)$$

whose images $\gamma(x_0, t)$ cross the real axis in the x -plane. Notice that, for $\epsilon > 1$, these singularities are distinct from the points of degeneracy of the characteristic map. Equation (2.20) implies that, associated to (2.31), the solution would have the behaviour:

$$u(x, t) \simeq (x - z)^{\frac{\epsilon - 1}{\epsilon}}, \quad x \sim z, \quad (2.32)$$

where $z = \gamma(x_0, t)$. However, we did not find examples of this kind of singularities.

2. \mathcal{PT} deformation of the inviscid Burgers equation

We have considered the initial condition $u_0(x) = \frac{1}{1+x^2}$ for several values of ϵ , and in all these examples the images of the roots of (2.31) in the complex x -plane appear to stay safely away from the real axis¹.

2.3 Summary of the results of this chapter

Let us summarise the main findings of this chapter.

- We have shown that one of the conclusions of the paper Bender & Feinberg [2008] is not correct. In fact, while in this work it was stated that the \mathcal{PT} -symmetrically deformed inviscid Burgers equation (2.15) does not exhibit shocks for $\epsilon \neq (2n+1)$, $n \in \mathbb{Z}$ and real initial conditions, we argued (presenting some explicit examples) that singularities can occur for any value of ϵ .
- Secondly, we gave a characterisation of the singularities, showing that, in the generic case when $u \neq 0$ at the singularity, the solution approaches the profile

$$u(x, t_c) - u(x_c, t_c) \sim (x - x_c)^{\frac{3}{2}}, \quad \text{for } x \sim x_c, \quad (2.33)$$

(where t_c and x_c denote, respectively, the time and position at which the singularity is formed). This behaviour is the same for all $\epsilon > 1$, and is markedly different from the undeformed $\epsilon = 1$ case, where singularities are (or are formed by collisions of) simple square-root points in the x -plane.

- Finally, we have argued that the cases $\epsilon = (2n+1)$, $n \in \mathbb{N}$ are distinguished by the fact that a real solution becomes multi-valued but remains continuous after the singularity, forming a self-intersection. We saw how this suggests a natural definition of weak solutions which remain continuous but develop a peak after the singularity.

¹ To be more precise, the images of some of the roots do cross the real x -axis at some values of t , but not on the principal Riemann sheet. Therefore they affect only some distant branches of the solution.

Chapter 3

Numerical study of the Rosenau-Hyman compacton equations

In this chapter we introduce the second main topic of the dissertation: the dynamics of one-dimensional PDEs with nonlinear dispersion, in particular equations admitting compacton solutions. To introduce this topic, we will review some well known results on a simple, nondispersive equation admitting dissipative compactly supported solutions, the porous medium equation. This example is used in particular to discuss a local relation between the behaviour of compactly supported solutions close to the endpoint of their support and the speed of motion of this point. In the case of the porous medium equation this relation is the famous Darcy's law Darcy [1856], and we show how it can be simply generalized to other models. Then we introduce the family of degenerate dispersive $K(m, n)$ equations of Rosenau & Hyman [1993] and review some of their properties. Finally we present some original numerical investigations on two equations of this family, the $K(2, 2)$ and the $K(4, 4)$ equation. These numerical experiments serve both to illustrate well-known properties of these equations and to make some new observations.

3.1 Solutions with compact support in degenerate equations

Compactly supported structures play an important role in the dynamics of *degenerate* quasi-linear equations, which are characterized by the fact that, for certain values of the dependent variable, the highest derivative term vanishes. In particular, we will be concerned with *evolutionary* equations¹, namely equations of the form

$$u_t = f(u, u_x, u_{xx}, \dots, u_{nx}), \quad n \in \mathbb{N}. \quad (3.1)$$

In this case, one can assume without great loss of generality that the degeneracy occurs for $u = 0$. In the following, we will consider equations of the form

$$u_t = A(u)u_{nx} + H(u, u_x, \dots, u_{(n-1)x}), \quad A(0) = 0, \quad (3.2)$$

where $n \in \mathbb{N}$ and A and H will be polynomials.

A first observation to make is that, around any point of the solution where $u = 0$, one cannot apply standard results such as the Cauchy-Kovalevskaya theorem (see Evans [2010]) to establish local existence, uniqueness and analyticity of the solution. This is the reason why it is possible to glue together the constant $u = 0$ solution with a piece of an ordinary solution obtaining a compactly supported (weak) solution. As stressed in particular in Li *et al.* [1999], the position of the interface where these solutions can be joined together is defined only by an intrinsic property of the equation, namely the vanishing of the highest derivative term. Therefore, these solutions can be seen as solutions in a stronger sense than, for example, shock solutions of the inviscid Burgers equation, where the position of the shock front is not intrinsically determined, but needs to be fixed by a physical prescription (see Section 2.1.3). For this reason, the authors of Li *et al.* [1999] refer to compactly-supported solutions to degenerate equations as *pseudo-classical* solutions. Moreover, the breakdown of the standard proof of

¹ Notice that many important phenomena are described by non-evolutionary equations. A prominent example is the integrable Camassa-Holm equation, which describes water waves beyond the KdV approximation Camassa & Holm [1993].

3. Nonlinear dispersion and compactons. Numerical studies

local analyticity also indicates that any points where the value $u = 0$ is reached are potentially singular – we will see many examples of these singularities in the following.

In the next section we will consider the first example of equation of this form, the porous medium equation.

3.2 The porous medium equation

The porous medium equation (PME) is a very well-studied degenerate equation whose typical solutions have a compact support. In one dimension, it reads

$$u_t = (u^m)_{xx} \tag{3.3}$$

where $m > 1$ and $u(x, t) \in \mathbb{R}$.

This equation is also known in the literature as the equation of non-stationary filtration or nonlinear heat equation, and was introduced in Muskat [1937], Leibenzon [1930] to describe the adiabatic propagation of an ideal gas through a porous medium, where $u(x, t)$ represents the density of the gas and the coefficient m is related to the coefficient of adiabatic expansion γ by $m = \gamma + 1$ ¹. In other words, m characterises the relation between the density of the gas and its pressure P , as in the equation of state

$$P \propto u^{m-1}. \tag{3.4}$$

The equation can be derived by using the fact that the propagation of the gas through a porous medium obeys an empirical law known as *Darcy's law* Darcy [1856], stating that the flux q (the rate of flow of gas through unit cross-sectional area) is proportional to the gradient of the pressure:

$$q \propto -P_x. \tag{3.5}$$

¹ The values of m relevant to this physical application are $m \geq 2$. However, from the mathematical point of view, the equation has a similar qualitative behaviour for all $m > 1$ and for this reason we do not restrict m to be greater than 2.

3. Nonlinear dispersion and compactons. Numerical studies

The equation (3.3) is then obtained (in appropriate units) as the conservation equation $u_t = -(uq)_x$.

We refer the reader to the monograph Vázquez [2006] for a full treatment of the porous medium equation, and in particular to Chapter 2 for the derivation of the model in different physical contexts.

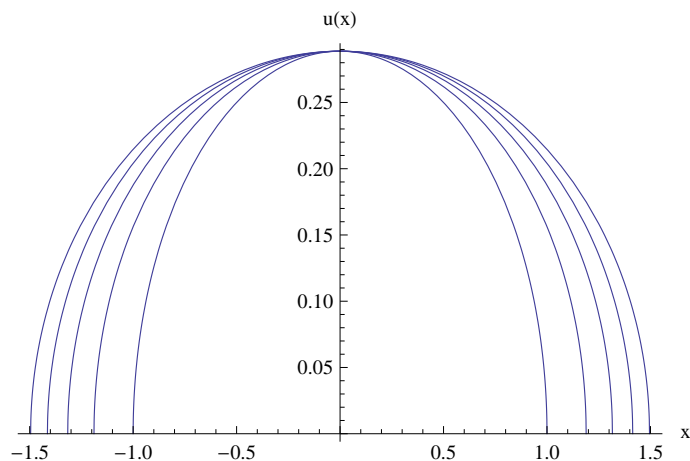


Figure 3.1: The Barenblatt solution (3.7) of the porous medium equation with $m = 3$, with the parameter choice $\beta = 1$, shown at times $t = 1, t = 2, t = 3, t = 4, t = 5$. The support of the solution spreads as time increases.

Notice that (3.3) can be seen as a nonlinear deformation of the heat equation, which is recovered for $m = 1$. The crucial effect of the nonlinearity is to make information propagate with a finite speed. This allows the porous medium equation to sustain solutions with a compact support, in contrast to the linear case, where it is well known that every compactly supported initial data spreads instantly over the whole real axis.

Because u usually represents a density, a particularly interesting class of solutions of (3.3) are the ones defined by a non-negative initial condition supported on an interval:

$$u(x, 0) = u_0(x), \tag{3.6}$$

where $u_0(x)$ is continuous, $u_0(x) > 0$ for $x \in [a, b]$ and $u_0(x) = 0$ for $x \notin [a, b]$, with $a, b \in \mathbb{R}$.

3. Nonlinear dispersion and compactons. Numerical studies

An explicit solution of (3.3) which can be used as a paradigm for any solution with an initial condition of the form (3.6) is the so-called *Barenblatt solution* Barenblatt [1953]:

$$U(x, t; m, \beta) = W t^{-\frac{1}{m+1}} \left(\beta^2 t^{\frac{2}{m+1}} - x^2 \right)^{\frac{1}{m-1}} \quad (3.7)$$

where $W = \left(\frac{(m-1)}{2m(m+1)} \right)^{\frac{1}{m-1}}$ and $\beta \in \mathbb{R}$ is a free parameter. It can be proved rigorously (see Oleinik *et al.* [1958], Kalashnikov [1967], Aronson [1969], Aronson [1970a], Aronson [1970b], Knerr [1977], Vázquez [2006] and references therein) that the generic solution of the Cauchy problem with an initial condition of the form (3.6) behaves very similarly to the Barenblatt solution. Let us list some of these results (a nice survey of all these properties is given in Knerr [1977]):

- The solution is defined globally for all times $t > 0$, and its support always remains a connected interval:

$$\text{supp } u(x, t) = [-\zeta_1(t), \zeta_2(t)]. \quad (3.8)$$

The sign of the solution are always preserved. The solution is smooth in the interior of its support, but is in general singular at the interface points, and has to be interpreted in the weak sense.

- The interface functions $\zeta_i(t)$, $i = 1, 2$ marking the position of the edges of the support are always monotonically non decreasing.

For each endpoint of the support there exists a, possibly vanishing, *waiting time* τ_i with $0 \leq \tau_i < \infty$ ¹ such that $\zeta_i(t) = \zeta_i(0)$ for $t \leq \tau_i$ and $\zeta_i(t') < \zeta_i(t'')$ for $\tau_i < t' < t''$.

- The speed of motion of the edges of the support is related to the singular behaviour of the solution at the interface.

¹ For the Barenblatt solution, $\tau_i = 0$ for $i = 1, 2$.

3. Nonlinear dispersion and compactons. Numerical studies

In fact, the functions $\zeta_i(t)$, $i = 1, 2$ are differentiable for $t > \tau_i$ and satisfy:

$$\frac{d}{dt}\zeta_i(t) = -\frac{m}{m-1} \lim_{\substack{x \rightarrow \zeta_i(t) \\ x \in \text{supp}}} \frac{\partial}{\partial x} u^{m-1}(x, t), \quad (3.9)$$

Due to (3.4), the last relation can be seen as a microscopic version of Darcy's law at the edge of the support (and is sometimes also referred to as Darcy's law). We will refer to it as the *edge equation*. Notice that requiring the right hand side of (3.9) to be nonzero implies that, for $m > 2$, the solution has $u_x \rightarrow \infty$ at the interface (see equation (3.18) below). On the other hand, when the solution has enough regularity at the edge, its support remains fixed. This explains the occurrence of a positive waiting time, which is the time required for the solution to steepen until it reaches a critical edge behaviour. As we will see below, these is a generic feature of degenerate equations.

3.2.0.1 Heuristic derivation of the edge equation

Let us now present a small heuristic derivation of Darcy's law (3.9). Although this argument is not rigorous, it will be useful in the rest of this work since it is easy to generalise to a more general degenerate equation. Let us consider a trajectory $y_\epsilon(t)$, $t > 0$, $y_\epsilon(t) \in \text{supp}(u(\cdot, t))$, defined by the condition

$$u(y_\epsilon(t), t) := \epsilon, \quad (3.10)$$

where $0 < \epsilon \ll 1$. Differentiating (3.10), we find

$$\frac{d}{dt}y_\epsilon(t) = -\frac{u_t(x, t)}{u_x(x, t)} \Big|_{x=y_\epsilon(t)} = -\frac{\frac{\partial^2}{\partial x^2} u^m(x, t)}{u_x(x, t)} \Big|_{x=y_\epsilon(t)}. \quad (3.11)$$

We will suppose that one of the interface functions $\zeta_i(t)$ is recovered as the limit $\lim_{\epsilon \rightarrow 0^+} y_\epsilon(t) = \zeta_i(t)$. Interchanging the time derivative with the $\epsilon \rightarrow 0^+$ limit,

3. Nonlinear dispersion and compactons. Numerical studies

we find

$$\frac{d}{dt}\zeta_i(t) = - \lim_{\epsilon \rightarrow 0^+} \frac{\frac{\partial^2}{\partial x^2} u^m(x, t)}{u_x(x, t)} \Big|_{x=y_\epsilon(t)} = - \lim_{x \rightarrow \zeta_i(t)} \frac{\frac{\partial^2}{\partial x^2} u^m(x, t)}{u_x(x, t)} \quad (3.12)$$

$$= -m \lim_{x \rightarrow \zeta_i(t)} \left((m-1) \frac{u_x(x, t)}{u^{2-m}(x, t)} + \frac{u_{xx}(x, t)}{u_x(x, t) u^{1-m}(x, t)} \right). \quad (3.13)$$

We are interested in the case of a moving interface, $0 \neq \frac{d}{dt}\zeta_i(t) \in \mathbb{R}$. We shall make the assumption that the two terms on the rhs of (3.13) both have, individually, a finite and nonzero limit ¹: for $m \neq 2$, this is possible only if u_x vanishes (for $1 < m < 2$) or diverges (for $m > 2$) at the interface. Then, by l'Hopital's theorem ², we have (for $m \neq 2$),

$$\lim_{x \rightarrow \zeta_i(t)} \frac{u_x(x, t)}{u^{2-m}(x, t)} = \lim_{x \rightarrow \zeta_i(t)} \frac{u_{xx}(y, t)}{(2-m)u^{1-m}(x, t) u_x(x, t)}, \quad (3.14)$$

and (3.13) becomes

$$\frac{d}{dt}\zeta_i(t) = -m \lim_{x \rightarrow \zeta_i(t)} u^{m-2}(x, t) u_x(x, t) = -\frac{m}{m-1} \lim_{x \rightarrow \zeta_i(t)} \frac{\partial}{\partial x} u^{m-1}(x, t). \quad (3.15)$$

Invoking enough regularity, this can be rewritten as a one-sided derivative taken in the interior of the support,

$$\frac{d}{dt}\zeta_i(t) = -\frac{m}{m-1} \frac{\partial}{\partial x} u^{m-1}(x, t) \Big|_{x=\zeta_i(t)}, \quad (3.16)$$

¹This excludes the possibility that $u_{xx} \rightarrow \infty$ while $u_x \rightarrow b$, $b \in \mathbb{R} \setminus \{0\}$. We think this case is not relevant.

² In order to fulfil the conditions of the theorem, we assume that both u and its space derivatives are nonzero in a one-sided open neighbourhood of the interface. This is in accordance with the physical intuition about the simple, generic solutions we are trying to describe.

and, by definition of derivative,

$$\begin{aligned} \frac{d}{dt}\zeta_i(t) &= -\frac{m}{m-1} \frac{\partial}{\partial x} u^{m-1}(x, t) \Big|_{x=\zeta_i(t)} = -\frac{m}{m-1} \lim_{x \rightarrow \zeta_i(t)} \frac{u^{m-1}(x, t)}{(x - \zeta_i(t))}, \\ &= -\frac{m}{m-1} \left(\lim_{x \rightarrow \zeta_i(t)} \frac{u(x, t)}{(x - \zeta_i(t))^{\frac{1}{m-1}}} \right)^{m-1}. \end{aligned} \quad (3.17)$$

Equation (3.17) shows that, for $x \sim \zeta_i(t)$, the solution has the shape

$$u(x, t) \sim \left(-\frac{(m-1)}{m} \frac{d}{dt}\zeta_i(t) \right)^{\frac{1}{m-1}} (x - \zeta_i(t))^{\frac{1}{m-1}}. \quad (3.18)$$

Finally, let us point out that, as a shortcut to expression (3.15), one could also start from the expression in (3.12) and apply l'Hopital's rule "backwards":

$$\begin{aligned} \frac{d}{dt}\zeta_i(t) &= -\lim_{x \rightarrow \zeta_i(t)} \frac{\frac{\partial^2}{\partial x^2} u^m(x, t)}{u_x(x, t)} = -\lim_{x \rightarrow \zeta_i(t)} \frac{\frac{\partial}{\partial x} u^m(x, t)}{u(x, t)} \\ &= -\frac{m}{m-1} \lim_{x \rightarrow \zeta_i(t)} \frac{\partial}{\partial x} u^{m-1}(x, t). \end{aligned} \quad (3.19)$$

Notice that this trick implicitly requires that the expression obtained after integrating numerator and denominator is an indeterminate form. This is verified, a posteriori, by expression (3.18), and is equivalent to the assumption that the two terms on the rhs of (3.13) both have a finite, nonzero limit.

We will now turn to degenerate dispersive equations, where the dynamics will be much richer than that of the porous medium equation.

3.3 The equations of Rosenau and Hyman and compactons

The investigation of nonlinear dispersive effects was initiated by Rosenau and Hyman in the seminal study Rosenau & Hyman [1993] (for a review, see also Rosenau [2005]). They were motivated by the appearance of nonlinear dispersion in the description of a number of strongly nonlinear regimes in fluid mechanics, such as the formation of liquid drops and patterns on liquid surfaces. In their

3. Nonlinear dispersion and compactons. Numerical studies

study they introduced a now famous family of KdV-like models, known as $K(m, n)$ equations:

$$K(m, n) : \quad u_t + (u^m)_x + (u^n)_{xxx} = 0. \quad (3.20)$$

A crucial feature of (3.20) is that, due to the balance between nonlinear convection and degenerate dispersion, travelling solutions with vanishing boundary conditions as $x \sim \pm\infty$ necessarily have a compact support for all $m \geq 1$ and $n > 1$. These solutions were named *compactons* in a reference to solitons. Moreover, Rosenau and Hyman discovered numerically that arbitrary initial conditions appear to be resolved into a number of constituent compactons; furthermore, compactons scatter in a near-elastic manner. Both these properties justify the analogy with solitons and point out at the great stability of these solutions. In particular, the fact that they appear in the decomposition of arbitrary initial data resonates with the so-called *soliton resolution conjecture*, according to which, in a vast class of semilinear evolution equations (both integrable and nonintegrable), stable solitary waves play the role of nonlinear basis functions and dominate the initial value problem. See Tao [2009] for a discussion of the conjecture.

3.3.1 Compacton solutions

Let us consider compacton solutions in more detail. By making the substitution

$$u(x, t) = v(z), \quad z = x - ct, \quad (3.21)$$

(where c is the speed), one finds – after two integrations –

$$(v_z)^2 = -\frac{2}{n(n+m)}v^{2+m-n} + \frac{2c}{n(n+1)}v^{3-n} + K_1v^{2-n} + K_2v^{2-2n}. \quad (3.22)$$

To obtain compactly supported solutions which are not excessively singular at the edge of the support, we have to take the integration constants $K_1 = K_2 = 0$. Let us denote the compacton solution of $K(m, n)$ with speed c as $u_{(m,n;c)}(x, t)$.

3. Nonlinear dispersion and compactons. Numerical studies

For $m = n$, (3.22) can be solved explicitly and we find

$$u_{(n,n;c)}(x, t) = \begin{cases} \left(\frac{2nc}{n+1}\right)^{\frac{1}{n-1}} \cos^{\frac{2}{n-1}}\left(\frac{n-1}{2n}(x - ct)\right), & x \in \text{supp}(u(x, t)) \\ 0, & x \notin \text{supp}(u(x, t)) \end{cases}. \quad (3.23)$$

The amplitude is related to the speed – taller compactons travel faster but, contrary to the familiar case of solitary waves, the width of compacton solutions is independent on their amplitudes. This is due to the symmetry of the $K(n, n)$ equations under:

$$x \rightarrow x, \quad u \rightarrow Au, \quad t \rightarrow A^n t. \quad (3.24)$$

For $m \neq n$, $m, n > 1$, the solution is not always expressible in terms of elementary functions, and the width of its support does depend on the amplitude. However, it is qualitatively similar, with a single maximum, and satisfying the same scaling relation at the endpoints of its support, namely ¹

$$u_{(m,n;c)}(x, t) \sim |x - e_{\pm}(t)|^{\frac{2}{n-1}}, \quad \text{for } x \sim e_{\pm}(t), \quad (3.25)$$

where we have denoted e_{\pm} the endpoints of the support, namely $e_{\pm}(t) = ct \pm \frac{\pi n}{n-1}$.

Examples of single-compacton solutions are shown in Figure 3.2.

3.3.1.1 Compactons as weak solutions

Notice that, when $n = 2$ or $n = 3$, (3.23) can be considered almost as solutions in the ordinary, classical sense since, despite the fact that some of their higher derivatives are discontinuous across the endpoints of the support², one still has $u^n \in C^3$ so that the dispersive term of (3.20) is well-defined.

For $n > 3$, one can prove that compacton solutions satisfy the following weak

¹ This relation does not depend on the value of $m > 1$ since, close to the endpoints of the support, the right hand side of (3.22) is dominated by the v^{3-n} term.

² In particular, $u_{(m,2;c)}(x, t)$ is only differentiable up to the first order (the second derivative is discontinuous), while $u_{(m,3;c)}(x, t)$ is not differentiable (the first derivative is discontinuous across the endpoints).

3. Nonlinear dispersion and compactons. Numerical studies

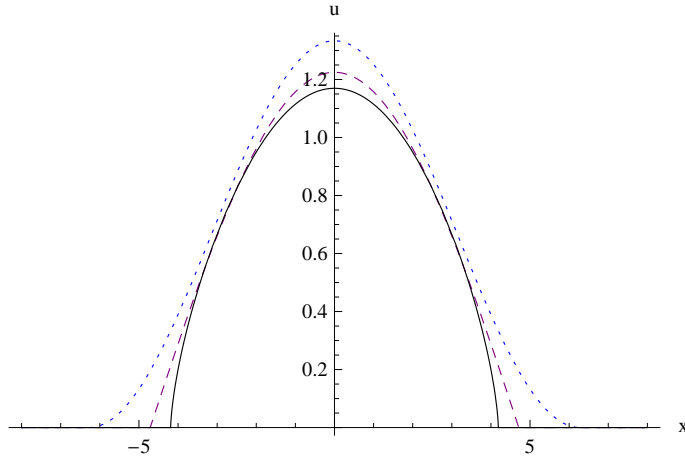


Figure 3.2: The shapes of compacton solutions to the K(2, 2) equation (blue, dotted), to the K(3, 3) equation (purple, dashed), and to the K(4, 4) equation (black, solid). In all cases we took $c = 1$. The behaviour of these three solutions close to the endpoints e_{\pm} of the support is $u_{2,2} \sim |x - e_{\pm}|^2$, $u_{3,3} \sim |x - e_{\pm}|$, and $u_{4,4} \sim |x - e_{\pm}|^{\frac{2}{3}}$, respectively.

formulation of (3.20):

$$\int_{-\infty}^{\infty} \int_0^{+\infty} dy dt \left[\partial_t f(y, t) u(y, t) - \partial_y f(y, t) (u^m(y, t) + \frac{\partial^2}{\partial y^2} u^n(y, t)) \right] = 0, \quad (3.26)$$

for every smooth and compactly supported $f \in C^{\infty}(\mathbb{R} \times [0, +\infty))$. In fact, because compactons are smooth in the interior of their support, it can be shown (for a rigorous proof in a similar case see Simpson *et al.* [2007], Proposition 6) that the only requirement in order to satisfy (3.26) is that

$$\lim_{\substack{x \rightarrow e_{\pm}(t) \\ |x - ct| < \frac{\pi n}{n-1}}} \frac{\partial^2}{\partial x^2} (u_{(m,n;c)}(x, t))^n = 0, \quad (3.27)$$

which is satisfied by all solutions to (3.22). A heuristic explanation for (3.27) is that this condition expresses the vanishing of the boundary terms arising from the integration by parts of (3.26) with respect to the y variable.

For a rigorous definition of compactons as weak solutions of the travelling

3. Nonlinear dispersion and compactons. Numerical studies

wave ODE, see also Li & Olver [1997].

However, we remind the reader that compactons appear to be solutions in a stronger sense than just weak solutions Li *et al.* [1999]. It has been proved Li & Olver [1997], Li & Olver [1998], although only in the case of the K(2, 2) equation, that they can be obtained as a limiting case of a family of smooth ordinary solutions. In fact, the above cited works show that travelling wave solutions with asymptotics $\lim_{x \rightarrow \pm\infty} u(x, t) = k \neq 0$ are smooth, and reduce to compactons of the same speed in the limit $k \rightarrow 0$.

It would be tempting to conjecture that the most general solution of the equation is a piecewise analytic function supported on a finite collection of intervals, satisfying (3.27). In fact, notice that any solution which were: a) continuous, b) supported on a finite collection of intervals, c) piecewise analytic in the interior of its support and d) satisfying the singularity bound (3.27) at every edge point, would be a well-defined weak solution in the same sense as (3.26). However, this class of functions appears too limited to describe the dynamics of these models. In particular, it is known Defrutos *et al.* [1995] that the evolution can lead to the formation of shocks. A precise mathematical formulation of these equations is still lacking. A more detailed discussion about these issues and on singularities is presented below and in Section 3.3.2.

Possible issues of ill-posedness Finding a good mathematical theory for compacton equations is a very important open problem. In particular, there are no results guaranteeing that the solution is globally defined in an appropriate function space. To the best of our knowledge, this holds true for degenerate dispersive equations in general, apart from exceptional cases where integrability plays a role such as the Camassa-Holm equation. The only available results are short-time existence results, valid as long as the solution remains bounded away from zero. Even more discouraging, it has been suggested that, for data close to zero, the K(2, 2) equation might be ill-posed Ambrose *et al.* [2012]. We remind the reader (see Evans [2010] for a complete treatment) that the initial value problem of a PDE is well-posed in a normed space of functions if the solution depends continuously on the initial data, while an equation is said to be ill-posed if its solutions do not depend continuously on the initial data, even for arbitrary short

3. Nonlinear dispersion and compactons. Numerical studies

times. It would be very problematic if the equation were not well-posed in any sense, and in particular this would make the numerical study of the equation meaningless. In Ambrose *et al.* [2012], the authors demonstrate numerically ill-posedness of the K(2, 2) equation in H^2 ¹. This is a serious issue to keep in mind when trying to interpret the numerical results. However, since the space H^2 is rather regular (in particular, it does not include solutions with shocks), a possible hopeful point of view is that the equation might still be well-posed in a more general function space.

3.3.2 Interactions of compactons

In Rosenau & Hyman [1993], Rosenau and Hyman performed an extensive numerical study of some of the equations (3.20) with $n \leq 3$, in particular equation K(2, 2), and made several important observations. First, they observed that the evolution of an arbitrary compactly supported initial condition yields its decomposition in a number of compactons (the decomposition process may also involve negative-amplitude compactons, known as anti-compactons). Moreover, they observed that collisions between two initially separated compactons travelling with different speeds are remarkably close to being elastic. In particular, compactons are able to pass through each other and separate again regaining – at least in the case of the K(2, 2) equations – exactly their original shapes and amplitudes. The process is not fully elastic because a third compact structure is left in the wake of the interaction. Typically, this ripple has a much lower amplitude than the two colliding compactons, and has both a positive and a negative part. The center of momentum of this structure appears to remain fixed, while it slowly decomposes into pairs of compactons and anti-compactons of very small amplitude. In Defrutos *et al.* [1995], it was also shown that the ripple typically develops a shock layer. This process is illustrated in Figures 3.3 and 3.11 for the K(2, 2) and K(4, 4) equations, respectively.

Although these robustness properties resemble strongly the properties of solitons in integrable models, it is important to remark that none of the K(m, n)

¹ The H^s -norm ($s \in \mathbb{N}$) is defined as $\|u(\cdot, t)\|_{H^s} = \sum_{i=1}^s \|\frac{\partial^i}{\partial x^i} u(\cdot, t)\|_{L^2}$, where derivatives up to the s -th order are supposed to exist in the weak sense.

3. Nonlinear dispersion and compactons. Numerical studies

models with $m, n > 0$ are integrable. In particular, it was recently proved in Vodova [2013] via a symmetry classification approach that the $K(n, n)$ model admits only four local conservation laws of the form

$$\partial_t \rho_i = \partial_x \sigma_i, \quad (3.28)$$

given by

$$\rho_1 = u, \quad \sigma_1 = (u^n)_{xx} + u^n, \quad (3.29)$$

$$\rho_2 = u^{n+1}, \quad \sigma_2 = nu^{2n-1}u_{xx} + \frac{n(n-2)}{2}u_x^2u^{2n-2} + \frac{1}{2}u^{2n}, \quad (3.30)$$

$$\rho_3 = u \sin(x), \quad \sigma_3 = (u^n)_{xx} \sin(x) - u_x \cos(x), \quad (3.31)$$

$$\rho_4 = u \cos(x), \quad \sigma_4 = (u^n)_{xx} \cos(x) + u_x \sin(x). \quad (3.32)$$

It is unclear if other, non-local conservation laws may play a role in explaining the exact preservation of the amplitudes of interacting compactons after the interactions. This peculiar property appears to hold for equations $K(2, 2)$ and $K(4, 4)$, and possibly for all equations of the form $K(2m, 2m)$, $m \in \mathbb{N}$. In other models, compacton collisions are still very robust interactions, but compactons may re-emerge with slightly different amplitudes: in the case of the $K(3, 3)$ equation, for instance, this is implied by the presence of the positive-defined conserved quantity $\int dx u^4$; after the creation of the ripple, the outgoing compactons must have lower amplitudes in order for this quantity to be preserved.

Further numerical studies of compacton collisions for members of the $K(m, n)$ family were presented in Defrutos *et al.* [1995]; Ismail & Taha [1998]; Mihaila *et al.* [2010b]. Other quasi-linear dispersive equations, such as the so called $L(l, p)$ equations

$$L(l, p) : \quad u_t + u^{l-2}u_x - p(u^{p-1}(u_x)^2)_x + 2\alpha(u^p u_x)_{xx} = 0, \quad (3.33)$$

$$(l, p \in \mathbb{N}, \quad p \geq 1, \quad l \geq 2)$$

introduced by Cooper-Shepard-Sodano in Cooper *et al.* [1993], were also studied numerically Mihaila *et al.* [2010a]. Interactions of compactons in quintic equations were studied in Cooper *et al.* [2001]. Although there are subtle differences in the

3. Nonlinear dispersion and compactons. Numerical studies

shape of the ripple left after the interaction (in particular, see Mihaila *et al.* [2010a] for a comparison between the Cooper-Shepard-Sodano equation and the $K(m, n)$ models), the general characteristics of compacton collisions were found to be the same in a vast class of models, and in all these cases these solutions appear to be extremely robust.

Finally, let us mention that interactions among compactons of positive and negative amplitude (the so-called anti-compactons) are very different, and do not show any signs of elasticity Cardenas *et al.* [2011]; Rosenau & Hyman [1993]. In the case of the $K(m, n)$ equations, it has been showed that they lead to the formation of very strong shock singularities, and it has been suggested that they may lead to a blow up of the equation.

Before presenting our numerical results, let us discuss some general properties of the equations.

3.3.2.1 Other general properties

Behaviour at the edge of the support Let us show how the *edge equation* (3.9-3.16) can be generalized in the case of the $K(m, n)$ equations. Repeating the heuristic argument ¹ introduced in Section 3.2.0.1, we expect that, for compactly-supported solutions that are sufficiently regular close to the endpoints of the support, the position of the edge $\zeta(t)$ satisfies:

$$\begin{aligned} \frac{d}{dt}\zeta(t) &= - \lim_{\substack{x \rightarrow \zeta(t) \\ x \in \text{supp}}} \frac{u_t(x, t)}{u_x(x, t)} = \lim_{\substack{x \rightarrow \zeta(t) \\ x \in \text{supp}}} \frac{u^m(x, t) + \frac{\partial^2}{\partial x^2}(u^n(x, t))}{u(x, t)} \\ &= \lim_{\substack{x \rightarrow \zeta(t) \\ x \in \text{supp}}} \frac{\frac{\partial^2}{\partial x^2}(u^n(x, t))}{u(x, t)}. \end{aligned} \tag{3.34}$$

Notice that in the last line we have omitted the contribution of the convective term, since we are assuming $m > 1$. Assuming that the limit in (3.34) exists, we

¹In the second equality of (3.34), we apply l'Hopital's rule backwards. As discussed in Section 3.2.0.1, this is justified heuristically because the resulting expression is seen a posteriori to be an indeterminate form.

3. Nonlinear dispersion and compactons. Numerical studies

have that, for $x \sim \zeta(t)$:

$$u(z, t) \simeq \left(\frac{(n-1)^2}{2n(n+1)} \frac{d}{dt} \zeta(t) \right)^{\frac{1}{n-1}} |z - \zeta(t)|^{\frac{2}{n-1}}. \quad (3.35)$$

Notice that this is the same behaviour of (3.25) but with c replaced by $\frac{d}{dt}\zeta(t)$. However, to the best of our knowledge, it has never been pointed out that, at least in sufficiently regular cases, the same behaviour should also hold for more general solutions with a nonconstant speed.

Singularities Finally, we would like to make a comment on the development of singularities for degenerate equations, as an introduction to the numerical data presented in the next section. In particular, we would like to point out that, as proved in Ambrose & Wright [2010]; Ambrose *et al.* [2012]; Wright & Ambrose [2012], the approach of the value $u = 0$ is intimately connected to the loss of smoothness. For example, in Wright & Ambrose [2012] (see Section 5 of that paper), is proved that an initially smooth and positive solution cannot reach the value $u = 0$ without, at least, causing the divergence of the H^4 -norm.

The results of Ambrose & Wright [2010] show that, for sufficiently smooth solutions to a degenerate equation, the measure of the support is invariant. In particular, Theorem 8 of that paper is particularly interesting. It states that compactly-supported solutions that are supported on intervals and that are at least piecewise- C^3 on their full support (including at the edge points) cannot change their sign. As remarked in that paper, since in many simulations it is observed that sign changes do take place, this demonstrates that singularities must be formed in conjunction with the development of a negative part.

We will see some examples in the numerical simulations of the following section. For instance, as discussed below, during the collision of two compactons, the creation of a shock layer across the point where the solution changes sign creating a negative part is always observed (a phenomenon first described in Defrutos *et al.* [1995]). Notice that this happens also for equations – such as $K(2, 2)$ – where compacton solutions are still quite regular at their edges. We remark that, although this appears to be always the case for the $K(m, n)$ equations, the

3. Nonlinear dispersion and compactons. Numerical studies

singularity may in principle not be associated to a shock. For example the results of Mihaila *et al.* [2010a] on the CSS equations appear to be consistent with the development of gradient singularities (see Figure 8 in that paper), but the formation of shocks was never observed.

Finally, the behaviour of the solution around points where $u = 0$ may be very different depending on the sign of u_x . In fact, our numerical observations indicate that no singularity is formed when a smooth piece of the solution changes sign crossing the line $u = 0$ with $u_x < 0$. Similarly, for positive compactly-supported solutions, no singular behaviour is observed close to the edge where $u_x < 0$. On the contrary, points where $u_x > 0$ are potentially very critical, and appear to be always associated to singularities. This was first pointed out in Defrutos *et al.* [1995] based on numerical observations as well as a rigorous argument. The authors of the latter paper also point out that an intuitive explanation comes from expanding the dispersive term of (3.20):

$$u_t = -3n(n-1)u^{n-2}u_xu_{xx} + \dots \quad (3.36)$$

For $u > 0$, $u_x > 0$, the term on the right hand side acts like a backwards heat operator, which is a dangerous possible source of instability.

3.4 Numerical study of the $K(2, 2)$ and $K(4, 4)$ equations

In this section we will present some numerical investigations on two models of the Rosenau-Hyman family, the $K(2, 2)$ and $K(4, 4)$ equations. The $K(2, 2)$ model has been considered by many authors Defrutos *et al.* [1995]; Mihaila *et al.* [2010b]; Rosenau & Hyman [1993]; Rus & Villatoro [2007a]. The main reason to consider the $K(4, 4)$ equation in detail is that it has the same degree of nonlinearity as the integrable equation (4.10), which will be the object of the next chapter. We will study this integrable equation numerically using the same method as for the Rosenau-Hyman models. The results of this chapter therefore serve also as a test of the numerical method.

3.4.1 General description of the numerical method

The numerical solution of degenerate equations has to deal with the difficult problem of representing non-smooth solutions. Some of the numerical techniques used to solve compacton equations include pseudo-spectral methods Rosenau & Hyman [1993], finite-difference methods Ismail & Taha [1998], methods based on Padè approximants Defrutos *et al.* [1995], finite-element methods Levy *et al.* [2004], particle methods Chertock & Levy [2001] or adaptive-grid methods Saucez *et al.* [2004]. For the numerical studies presented in this and in the following chapter, we have adapted the Padè finite-difference method introduced in Defrutos *et al.* [1995]. This method was originally used to solve the $K(2, 2)$ equation and was applied in Mihaila *et al.* [2010a,b] to the study of the $K(m, n)$ and CSS models. Let us give a general description of the method, referring to Appendix B for more details. The equation is solved numerically on a domain $I \times [0, T]$, where $T \in \mathbb{R}$, $[0, T]$ is the time domain and the space domain I is a finite interval. We always apply periodic boundary conditions on I , although in most of our simulations the support of the solution is, within numerical precision limits, strictly contained in I . The space domain is discretized with a constant step Δx and the space derivatives are approximated with the 4th order Padè approximant formulae of Defrutos *et al.* [1995]; Rus & Villatoro [2007a]. The detailed expressions are listed in Appendix B. The original PDE is then replaced by a system of ODEs for the time evolution of the solution vector sampled at the grid points, which is integrated with an appropriate ODE solver. Because this system of ODEs is stiff (see Iserles [2009], Press *et al.* [1990]), the method used for the time integration must be implicit.

In general, we observe that the time integration does not pose great accuracy or convergence problems. Usually we use a simple Crank-Nicolson method, which is 2nd order accurate; the difference between this method and a 4th order implicit Runge-Kutta method would not be appreciable on the scale of any of the Figures presented in this thesis.

3. Nonlinear dispersion and compactons. Numerical studies

The space discretization is a much more critical aspect, both for the accuracy and for the convergence of the numerical scheme. In fact, a common problem encountered when integrating compacton equations with a fixed-grid method is the introduction of spurious modes in the numerical solution. Typically, these spurious oscillations start localized around the trailing edge of compacton profiles. Even when trying to reproduce the simple one-compacton solutions, these disturbances tend to grow unstable due to nonlinear effects and can rapidly destroy the simulation. This problem can be controlled by applying an appropriate smoothing procedure. In the case of pseudo-spectral methods, one typically uses a frequency cut-off to remove the fastest oscillations, while in the case of finite-difference-based methods the common recipe is to introduce a small amount of dissipation. Namely, rather than (3.20), we discretise the equation

$$u_t + (u^m)_x + (u^n)_{xxx} = \eta_2 u_{xx} - \eta_4 u_{xxxx}, \quad (3.37)$$

where $0 < \eta_i \ll 1$ are assumed to be very small. Typically, we take $\eta_2 = 0$ and observe that the numerical scheme is stable, for most of the data presented in this chapter, for values of η_4 as small as 10^{-5} . Notice that the amount of dissipation needed to stabilize the numerics depends on the step size Δx : for smaller values of Δx , the scheme is stable with a lesser amount of dissipation.

The dissipation has some visible effects on the solution (see Abassy *et al.* [2009] for a specific study): the sharp edges of compactly supported solutions are replaced by exponential tails, the amplitude of compacton solutions is slowly damped, and low-amplitude numerical radiation is emitted Rus & Villatoro [2007b]. For improvements of the numerical method that can minimize these effects, see Garralón *et al.* [2013].

Finally, let us mention that in other, more sophisticated approaches, such as particle¹ methods Chertock & Levy [2001], finite element methods Levy *et al.* [2004] and adaptive-grid methods Saucez *et al.* [2004], there is apparently no need for adding dissipative terms as in (3.37).

¹ However, we point out that particle methods have an important limitation, since they preserve the sign of the solution. Therefore, they are unsuited to study equations where sign changes can take place, which is the case for the Rosenau-Hyman models.

3. Nonlinear dispersion and compactons. Numerical studies

In all the simulations presented below, we verified that the conserved quantities

$$F_i \equiv \int dx \rho_i(x), \quad i = 1, \dots, 4, \quad (3.38)$$

with ρ_i defined in (3.29-3.32) are preserved as long as the solution does not develop shock singularities, although they are slowly dissipated due to the added viscosity. In all the simulations presented below, this dissipation rate did not exceed a fraction of 0.1% of the total for each conserved charge, for unit time. Notice that the conservation of F_1 is automatically enforced numerically since the numerical scheme is conservative, however the preservation of the other three quantities is a nontrivial test of our numerics. After shocks are formed, the conserved charges F_j are no longer exact with $j \geq 2$, due to boundary conditions across the shock front.

3.4.2 Numerical experiments: the K(2, 2) equation

Let us present some numerical experiments on the K(2, 2) equation. In particular we will present three types of phenomena:

- The collision of two compactons.
- The decomposition of a generic compactly-supported, positive initial profile.
- The development of a singularity in a solution initially smooth and strictly positive.

Collision The collision among two compactons with speeds $c_1 = 3$, $c_2 = 1$ is illustrated in Figure 3.3. This simulation was obtained with $\Delta x = 50/2048 \sim 0.024$ and by adding the dissipation $\eta_2 = 0$, $\eta_4 = 10^{-3}$. Our choice of initial separation is such that the supports of the two compactons merge at time $t = 0.217$. After the interaction, the fastest compacton appears to re-emerge around time $t = 12.$, while the second separates from the residual “ripple” around time $t = 22$. Both appear to regain exactly their amplitudes. In the case of the smaller compacton, the relative amplitude drop is less than 0.3 percent after the

3. Nonlinear dispersion and compactons. Numerical studies

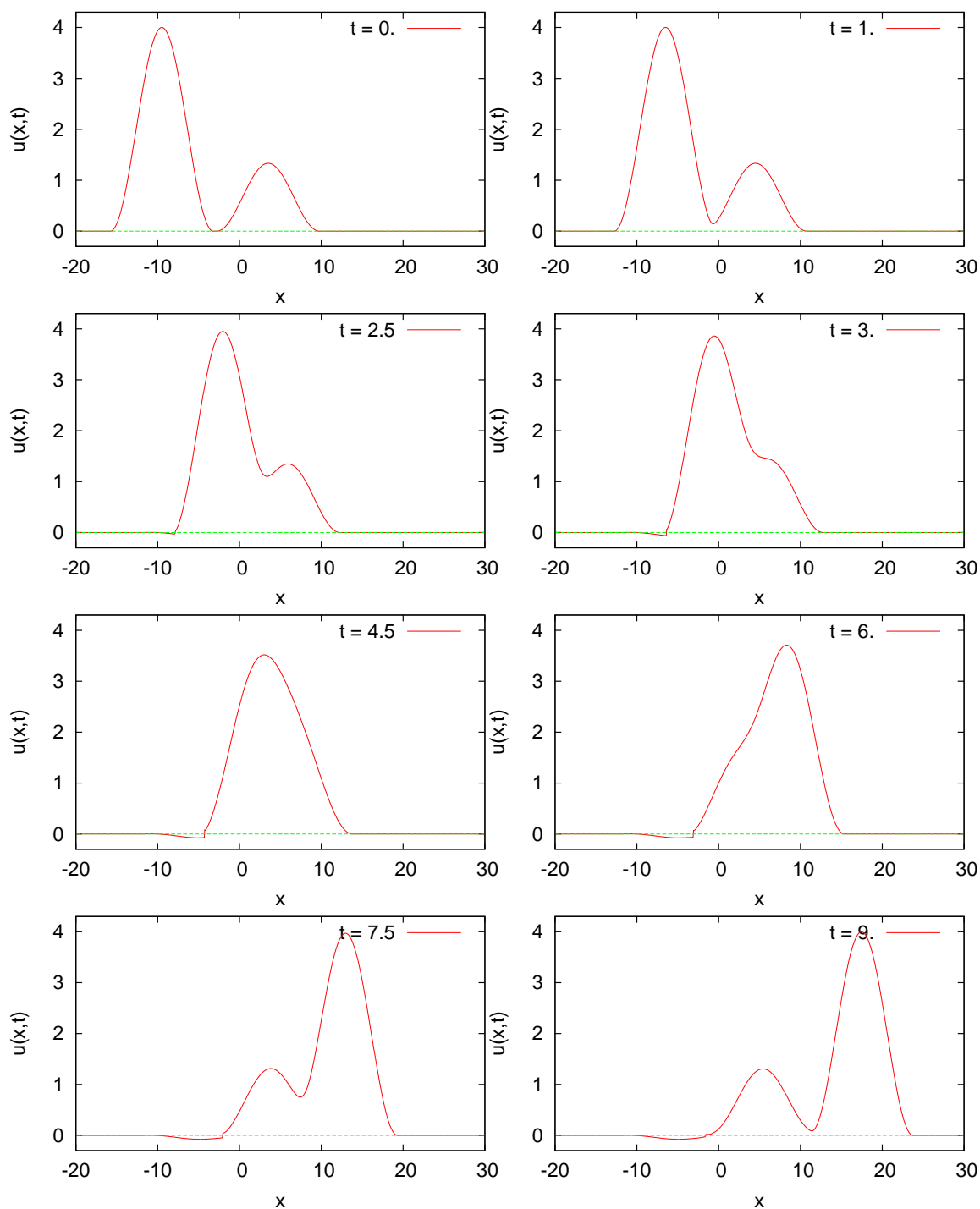


Figure 3.3: Numerical solution of the $K(2, 2)$ equation showing the scattering among two compactons of speeds $c_1 = 1$ and $c_2 = 3$. This simulation was performed with $\eta_2 = 0$ and $\eta_4 = 10^{-3}$.

3. Nonlinear dispersion and compactons. Numerical studies

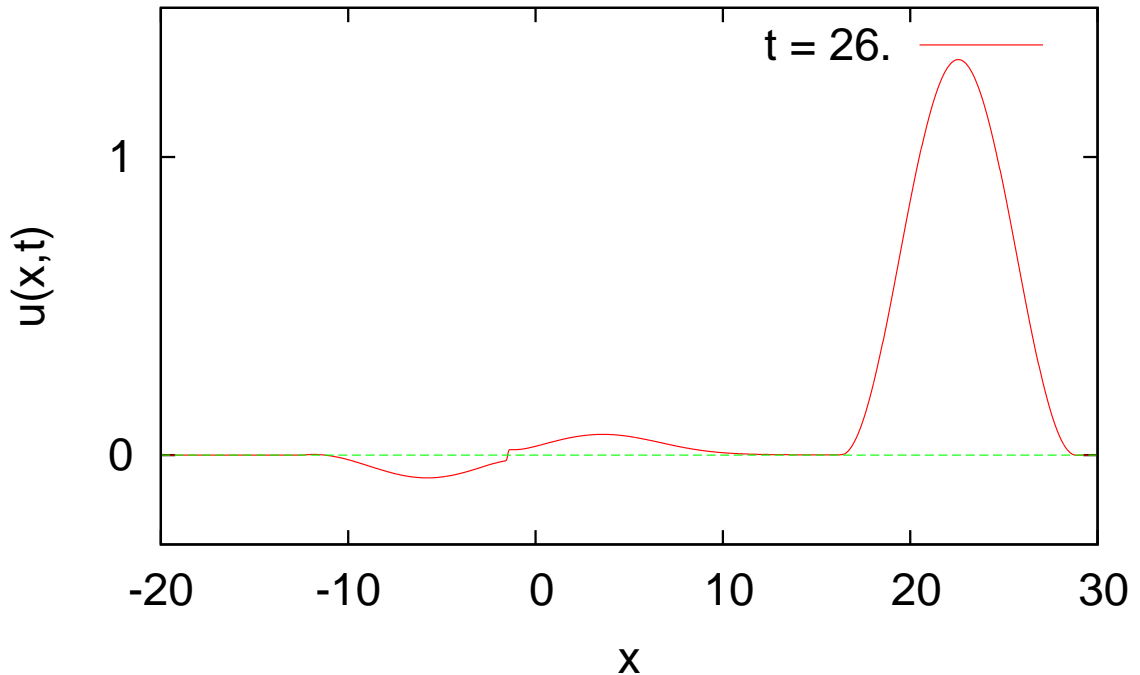


Figure 3.4: Detail of the ripple left by the collision of two compactons, for the same data shown in Figure 3.3. The compacton on the right of the picture is the $c = 1$ compacton after its emergence from the interaction.

interaction (which we believe is due to the rather large added dissipation used for this set of data), while the agreement is even better for the taller compacton.

We observe that the separation of the emerging compactons from the part of the solution that is left behind is very regular and no singularities are formed at the point where the support splits.

It is interesting to describe in detail the creation of the ripple, which starts to form around the left endpoint of the support of the solution during the interaction of the two compactons. In this example, roughly around time $t \sim 1.9$, the solution bends down and starts to become negative at the left edge of the support. The interface between the negative and the positive parts of the solution is a shock, which is visible starting from the third panel in Figure 3.3. The shock layer initially moves to the right, disclosing the negative part of the ripple in its wake. Then it slows down and appears to stop moving around time $t \sim 10$: at this point, the positive part of the ripple starts to be revealed to the right of the shock layer, as the compacton with speed $c = 1$ moves away. Notice that, on the time scale of the emergence of the two compactons, the ripple appears essentially

3. Nonlinear dispersion and compactons. Numerical studies

still. The shape of the ripple left at the interaction site can be seen in Figure 3.4, where in particular the shock layer connecting its negative and positive parts is clearly visible. The amplitude of the ripple is of order $\sim 0.07 - 0.08$.

Considering several other choices of speeds for the colliding compactons, we observed that the formation of the ripple is qualitatively very similar in all cases. In particular, we always observed the formation of a single shock layer. As a last observation, we did not notice a simple relation between the amplitude of the ripple and the speeds of the colliding compactons. For example, colliding two compactons of speeds $c_1 = 3$, $c_2 = 2.5$, the ripple had roughly half the amplitude as in the previous example; colliding two compactons with amplitudes $c_2 = 3$, $c_1 = 0.2$, the amplitude of the ripple was ~ 0.03 .

Decomposition of compact initial data In a second experiment, we consider the decomposition of a positive, compactly supported initial condition. In particular, we considered several conditions of the form

$$u(x, 0) = \begin{cases} \cos^4\left(\frac{\pi x}{2W}\right), & |x| < W \\ 0, & |x| > W \end{cases}, \quad (3.39)$$

for different values of W . The data relative to $W = 6\pi$ are represented in Figure 3.5. This simulation was obtained with a step size $\Delta x = 60/2048 \sim 0.03$ and with added viscosity $\eta_2 = 0$ and $\eta_4 = 10^{-3}$.

The Figure illustrates the emergence of one compacton by time $t \sim 7$. ; a second compacton structure of smaller amplitude ~ 0.19 was clearly formed (however it had not completely separated from the residual part of the data) when we stopped the simulation at time $t = 25$. Notice also the small shock layer visible close to the left edge of the solution. This is a general feature of the decomposition of compactly supported positive initial data. In several simulations with initial conditions of the form (3.39) we observed the development of fast oscillations close to the left edge of the support, leading to the formation of a sequence of shocks. We believe this is not a numerical artefact. A similar phenomenon was first observed in the case of the K(3, 3) equation in Levy *et al.* [2004], although in that case no comments were made on the evolution of the oscillations into shocks. In the present case, we observe the following general characteristics of

3. Nonlinear dispersion and compactons. Numerical studies

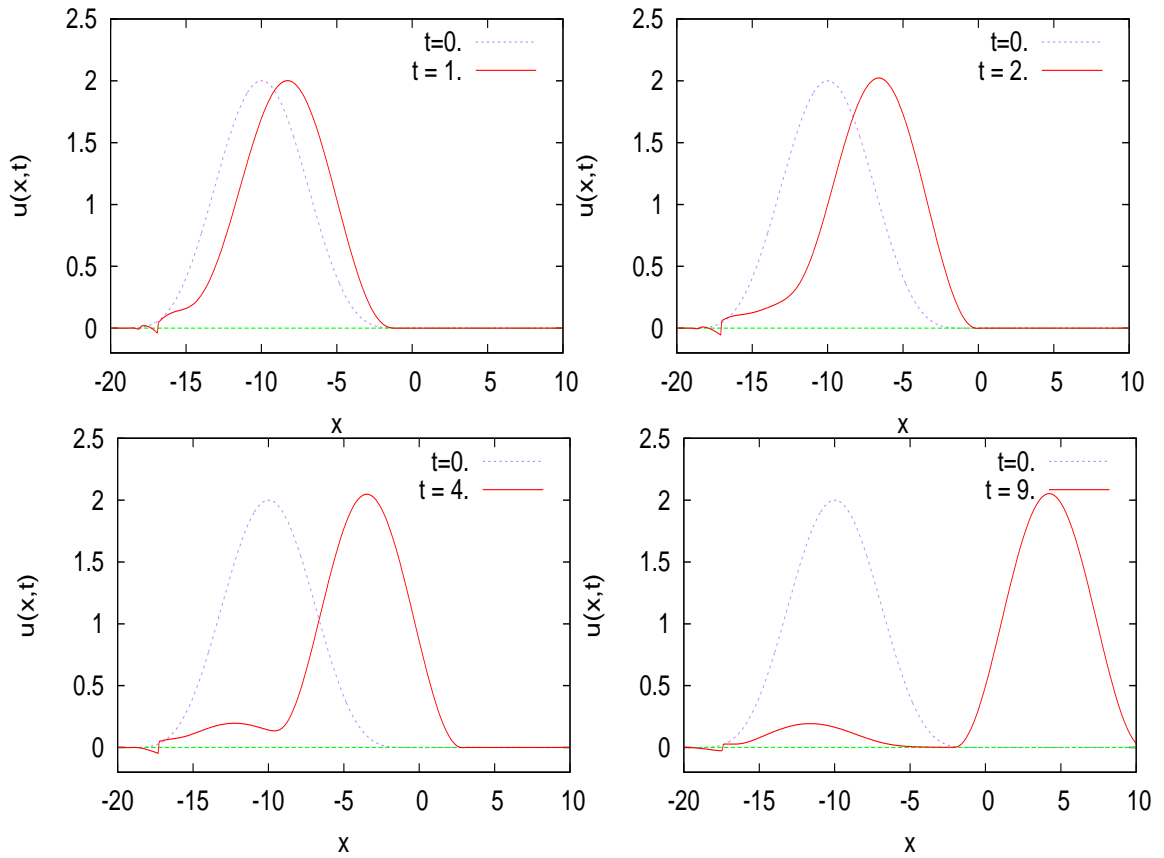


Figure 3.5: $K(2,2)$ equation: evolution of the initial condition $u(x,0) = \cos^4(\frac{x}{6})\chi_{[-3\pi,3\pi]}(x)$. The data in the plot were obtained by adding the viscosity $\eta_2 = 0$ and $\eta_4 = 10^{-3}$.

the sequence of shock layers: the discontinuities always form across the line $u = 0$, jumping between a region with $u < 0$ at the immediate left of the shock layer and $u > 0$ at its immediate right. The shock layers are connected by apparently smooth pieces of the solution crossing $u = 0$ with $u_x < 0$. This “radiation” shows a tendency of moving leftwards. However, the precise structure and evolution of these oscillations is difficult to follow, since the added dissipation needed to stabilize the numerical method tends to eventually dissipate these oscillations.

An interesting dynamics can be observed in the case of initial data with a very narrow support. In Figure 3.6 and 3.7 are shown aspects of the evolution of data of the form (3.39), whose initial support has width $W = \frac{2}{3}\pi$ (we remind the reader that the width of a traveling compacton solution is 2π). It was already

3. Nonlinear dispersion and compactons. Numerical studies

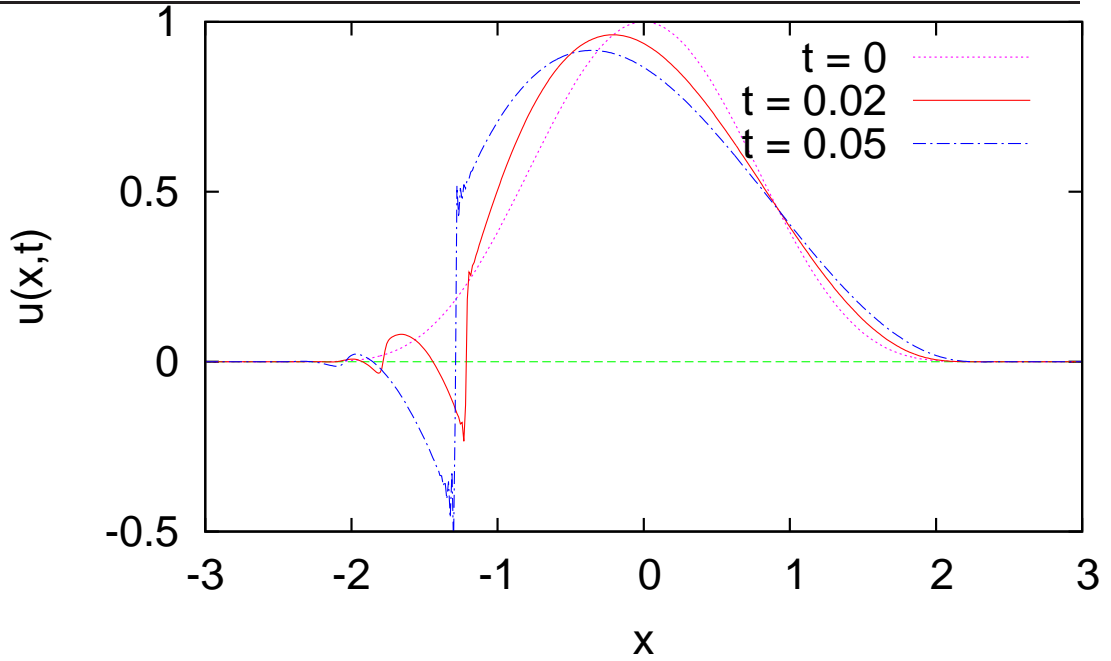


Figure 3.6: K(2,2) equation: decomposition of very narrow initial data $u(x,0) = \cos^4(\frac{3x}{4})\chi_{[-\frac{2}{3}\pi, \frac{2}{3}\pi]}(x)$, showing a sequence of shocks formed close to the left endpoint of the support. The simulation was done with added dissipation $\eta_4 = 10^{-3}$.

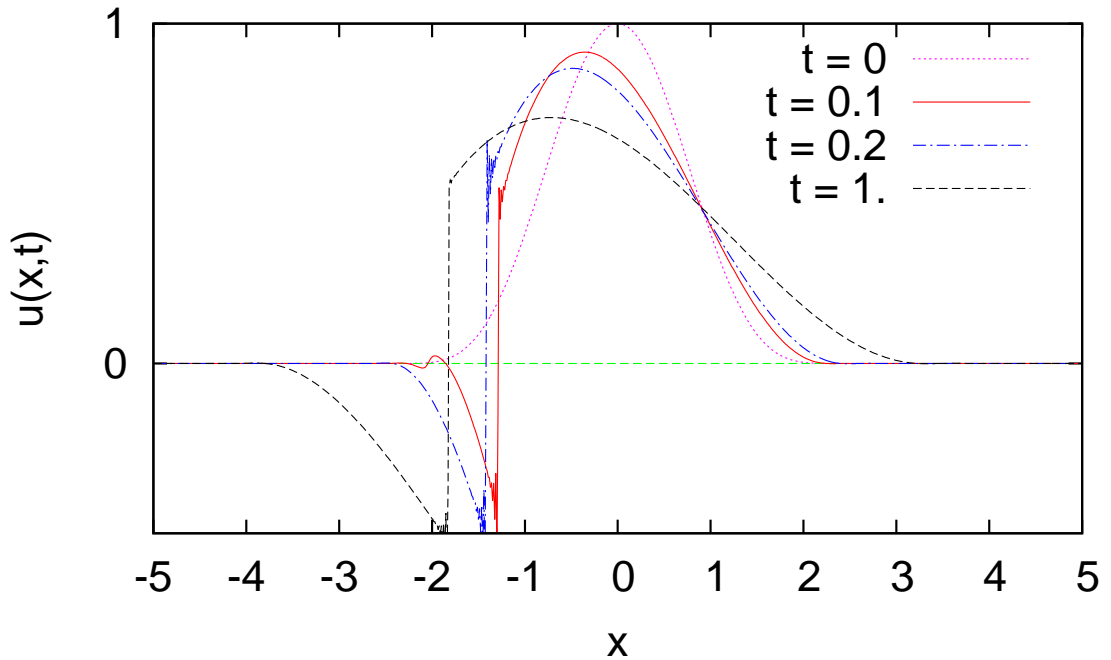


Figure 3.7: Evolution of the same data as in Figure 3.6, for larger times.

3. Nonlinear dispersion and compactons. Numerical studies

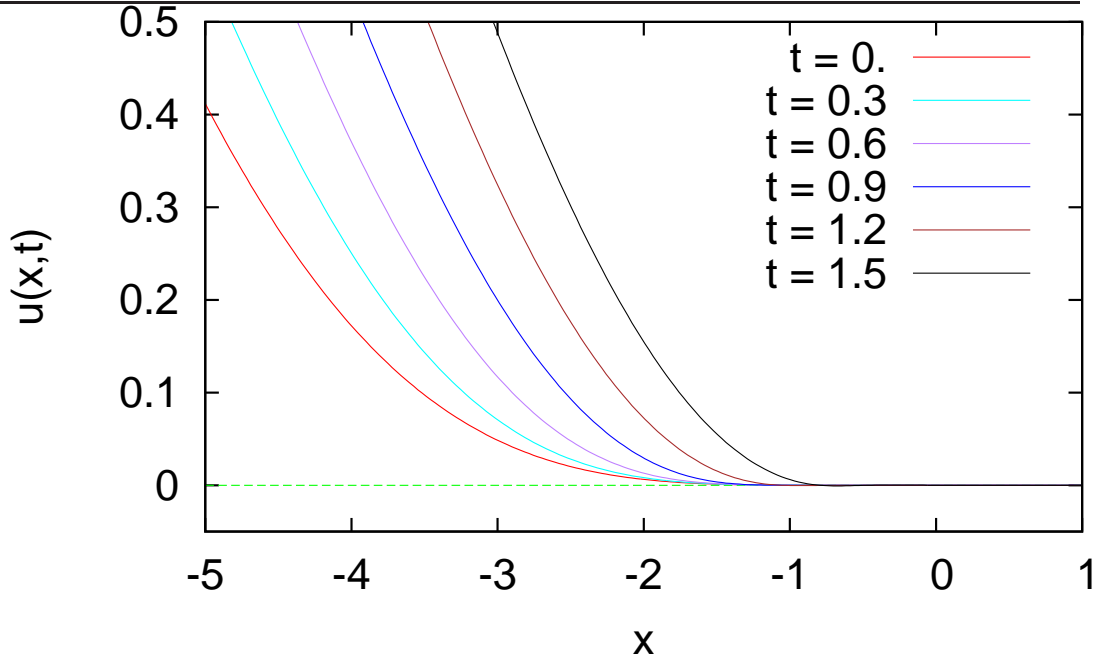


Figure 3.8: Illustration of the steepening at the right edge of the support for the same data as in Figure 3.5.

observed in Rosenau & Hyman [1993] that the evolution of very narrow initial data leads to very strong shock singularities. The shape of the radiative oscillations described above is clearly visible in the Figures. The data were obtained with $\Delta x = 12/1024 = 0.012$ and with dissipation specified by $\eta_4 = 10^{-3}$. We observe that, as a result of the dissipation, all the shock layers to the left of the largest, rightmost one gradually shrink and disappear. The numerical solution then has developed a negative part on the left of this shock layer and the support starts expanding in both directions; eventually, for later times than those shown in the figures above, compactons and antcompactons are emitted from the shock layer. These data appear to show that even narrow initial data can decompose into compactons and antcompactons and that there is no blow-up. However, the transition described above to a profile with a single shock layer may also be simply a product of the addition of dissipation. Similar observations were made in Mihaila *et al.* [2010b].

As a final comment, we always observed that the behaviour close the right edge of the support is very regular. We observe that there is a waiting time, during which this endpoint remains motionless, while the solution gradually steepens

3. Nonlinear dispersion and compactons. Numerical studies

until it attains the scaling $u \sim x^2$. This process is very smooth, as can be seen in detail in Figure 3.8.

Data initially bounded away from zero Let us now illustrate how initial data smooth and bounded away from zero can reach the value $u = 0$ and develop a singularity. In Figure 3.9 we show the evolution of the smooth periodic initial profile

$$u(x, 0) = \sin\left(\frac{\pi x}{3}\right) + 1.1. \quad (3.40)$$

The simulation was performed with a step size $\Delta x = 60/4096 \sim 0.015$ and with added dissipation defined by $\eta_2 = 0$, $\eta_4 = 10^{-3}$.

The profile bends towards the line $u = 0$ reaching it around time $t \sim 0.036$. Judging from the data, the solution appears to form a cusp with finite value of u_x on both sides but with $u_{xx} \rightarrow \infty$ as it touches zero. A detail is shown in Figure 3.10. After it crosses the line $u = 0$, the solution appears to develop a shock layer, shown in the last three panels of Figure 3.9. Notice that the addition of dissipation with $\eta_4 = 10^{-3}$ is needed for the simulation to converge after the singularity time. However, for times $t \leq 0.036$, when the solution is still strictly positive, there is no need for any added viscosity. In Figure 3.10 is shown that the solution obtained with $\eta_4 = 10^{-3}$ and with $\eta_4 = 0$ display a perfect agreement up to the time of singularity formation.

Finally, notice that data which vary on a larger scale appear to remain smooth for longer times. In particular, we have considered the evolution of an initial profile specified by stretching $u(x, 0) = \sin\left(\frac{2\pi x}{15}\right) + 1.1$: the solution remains smooth and positive at least until time $t = 25$. The evolution of this profile shows the emergence of three smooth structures that travel across the periodic domain displaying an apparently recurrent behaviour and, during this time span, the solution does not approach the line $u = 0$ significantly.

3. Nonlinear dispersion and compactons. Numerical studies

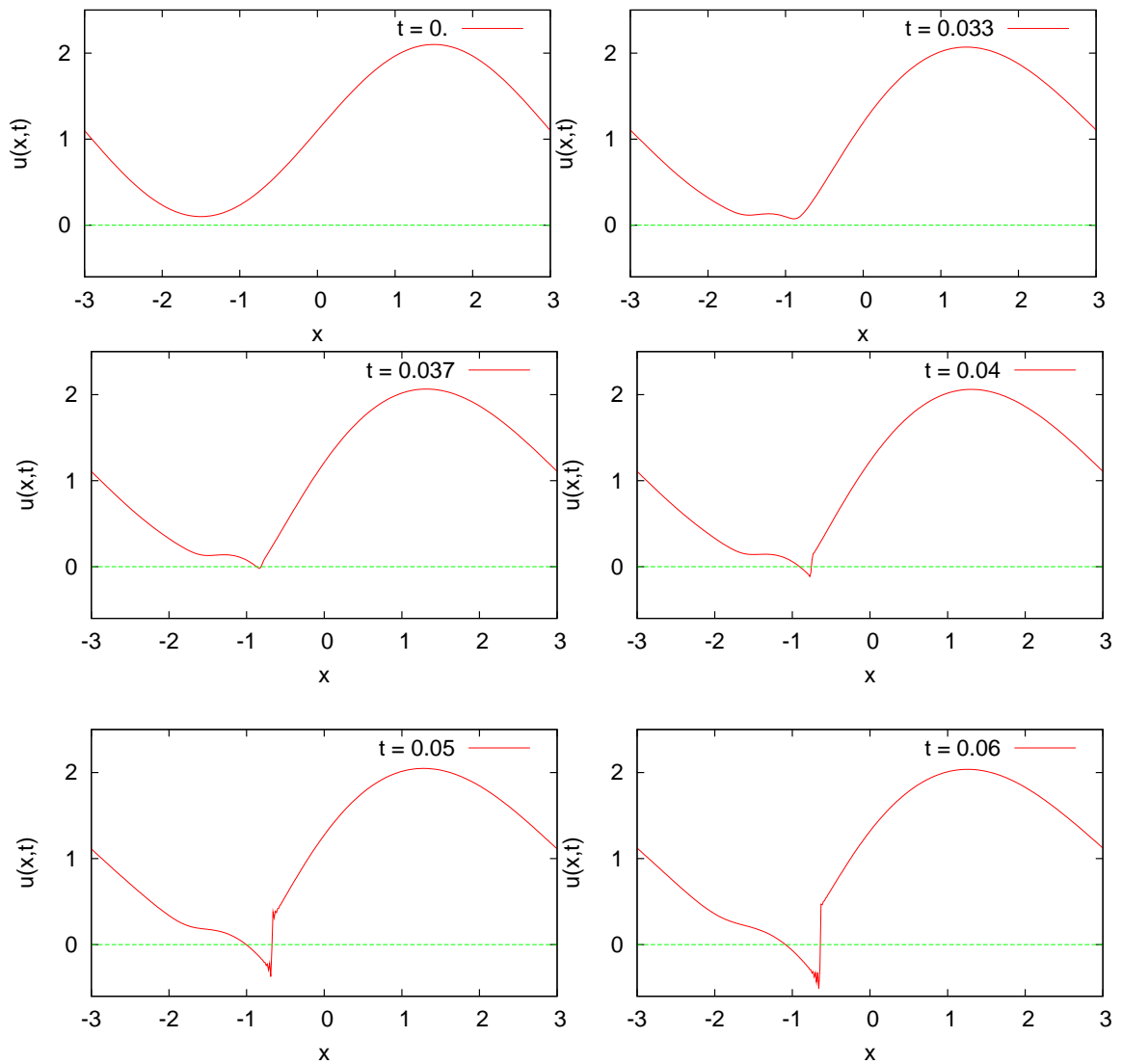


Figure 3.9: K(2,2) equation: evolution of the initial condition $u(x,0) = \sin(\frac{\pi x}{3}) + 1.1$. The profile crosses the critical line $u = 0$ around time 0.036, developing a shock discontinuity for later times.

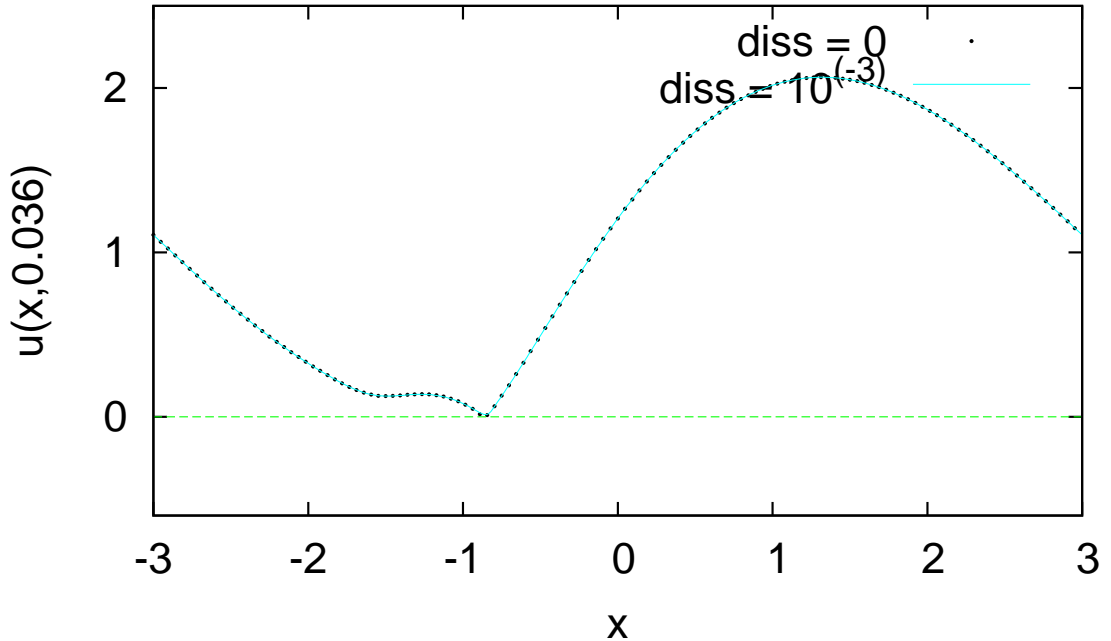


Figure 3.10: Detail of the approach to singularity for the same solution to the $K(2, 2)$ equation as in Figure 3.9. Dots (black) represent the numerical solution obtained without adding any dissipative term, while the continuous (light-blue) line was obtained with $\eta_4 = 10^{-3}$ (the two curves are almost indistinguishable in the plot).

3.4.3 Numerical experiments: the $K(4, 4)$ equation

Let us now present some numerical experiments on the $K(4, 4)$ equation, in the same dynamical regimes previously analyzed for the $K(2, 2)$ model. We find that, apart from local differences, the behaviour is overall very similar. This also demonstrates that the numerical method works rather well also in describing this more singular equation.

Collision among compactons Similar to the $K(2, 2)$ case, collisions among compacton solutions to the $K(4, 4)$ equation are very robust. In Figure 3.11 we show the collision among two compactons with speeds $c_1 = 2$ and $c_2 = 1$, whose supports come in contact at time $t \sim 0.6$. This simulation was obtained with a step size $\Delta x = 35/1024 \sim 0.034$ and with added viscosity $\eta_2 = 0$ and $\eta_4 = 3 \times 10^{-5}$.

3. Nonlinear dispersion and compactons. Numerical studies

The mechanism of formation of the ripple left as a residual of the interaction is very similar to the $K(2,2)$ case, and leads to the formation of a single shock layer across the line $u = 0$. In the present case this structure has a rather small amplitude as can be seen in Figure 3.12.

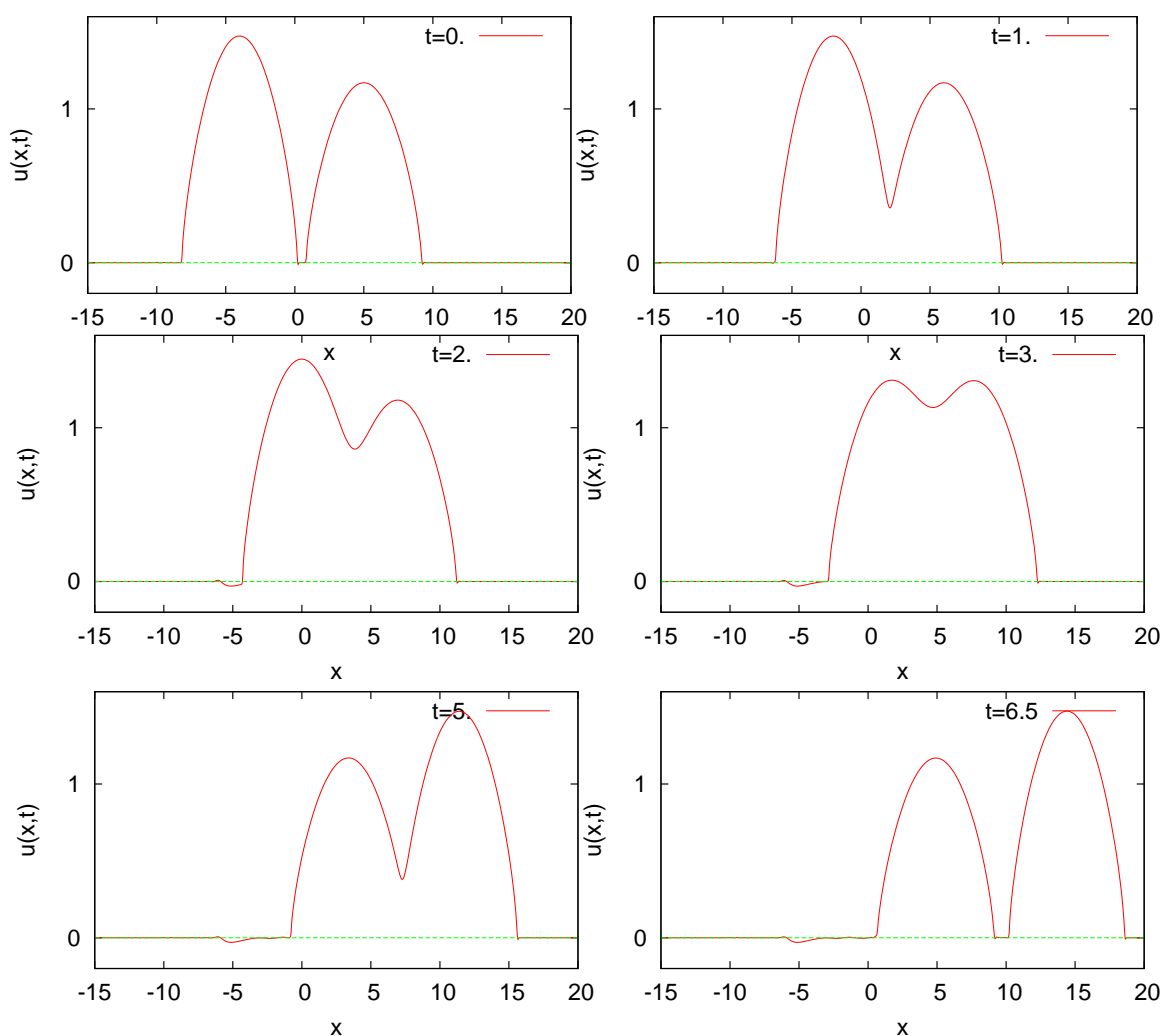


Figure 3.11: $K(4,4)$ equation: collision among two compactons with speeds $c_1 = 2$ and $c_2 = 1$. This simulation was obtained with added viscosity $\eta_2 = 0$ and $\eta_4 = 3 \times 10^{-5}$.

3. Nonlinear dispersion and compactons. Numerical studies

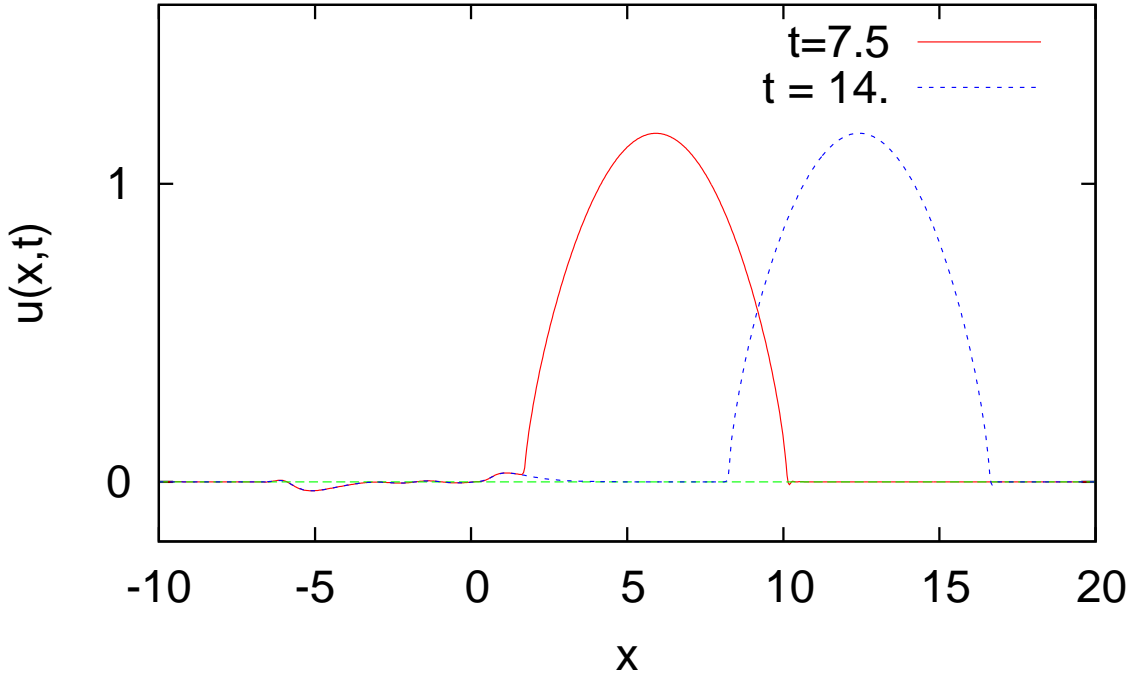


Figure 3.12: The figure shows two later snapshots of the evolution of the same data as in Figure 3.11, showing the separation of the $c = 1$ compacton from the residual left at the site of the interaction (notice that the faster, $c = 2$ compacton has been removed and is not visible in the plot).

Decomposition of compact initial data In Figure 3.13 is displayed the evolution of the profile

$$u(x, 0) = \begin{cases} \cos\left(\frac{\pi x}{20}\right), & |x| < 10 \\ 0, & |x| > 10 \end{cases} .$$

These numerical data were obtained with $\Delta x = 50/1024 \sim 0.049$ and with added dissipation $\eta_4 = 10^{-4}$. In the Figure is clearly visible the emergence of two individual compactons. In analogy to the $K(2,2)$ case, we observe that the steepening of the solution close to the right endpoint of the support is very smooth, while several oscillations are formed close to the left edge.

Looking more closely at the shape of the oscillations formed close to the left edge, we see that, when the solution first touches $u = 0$ at its inflection point, it forms an infinite derivative spike. This is illustrated (for a different initial condition) in Figure 3.14. After the solution becomes negative, they appear to evolve into a number of shock layers connected by pieces of the solution that cross

3. Nonlinear dispersion and compactons. Numerical studies

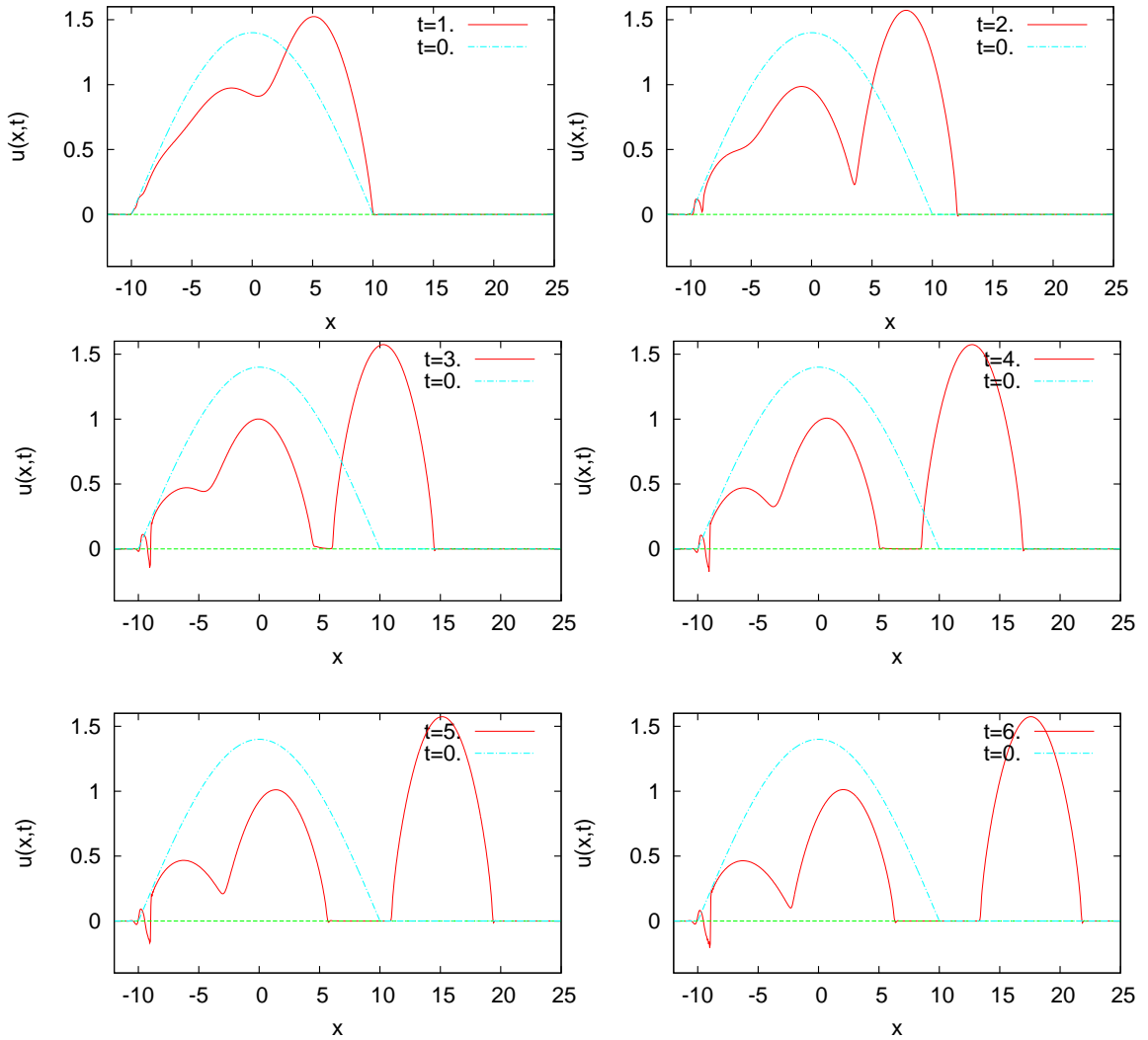


Figure 3.13: $K(4,4)$ equation: decomposition of the compactly supported initial data $u(x, 0) = \cos(\frac{\pi x}{20})\chi_{[-10,10]}(x)$. Data obtained with added dissipation $\eta_4 = 10^{-4}$.

$u = 0$ with $u_x = -\infty$. Our data are not clear on the fate of these oscillations. Similar to the $K(2,2)$ case, the smaller oscillations are eventually dissipated by the added viscosity necessary to stabilise the simulation. However, we point out that, at least for the duration of our simulation of Figure 3.13, the left endpoint of the support of the solution does not seem to be able to expand beyond its initial position. Finally, let us stress that the numerical solution appears to be very reliable to the right of the rightmost shock layer visible in Figure 3.13. In

3. Nonlinear dispersion and compactons. Numerical studies

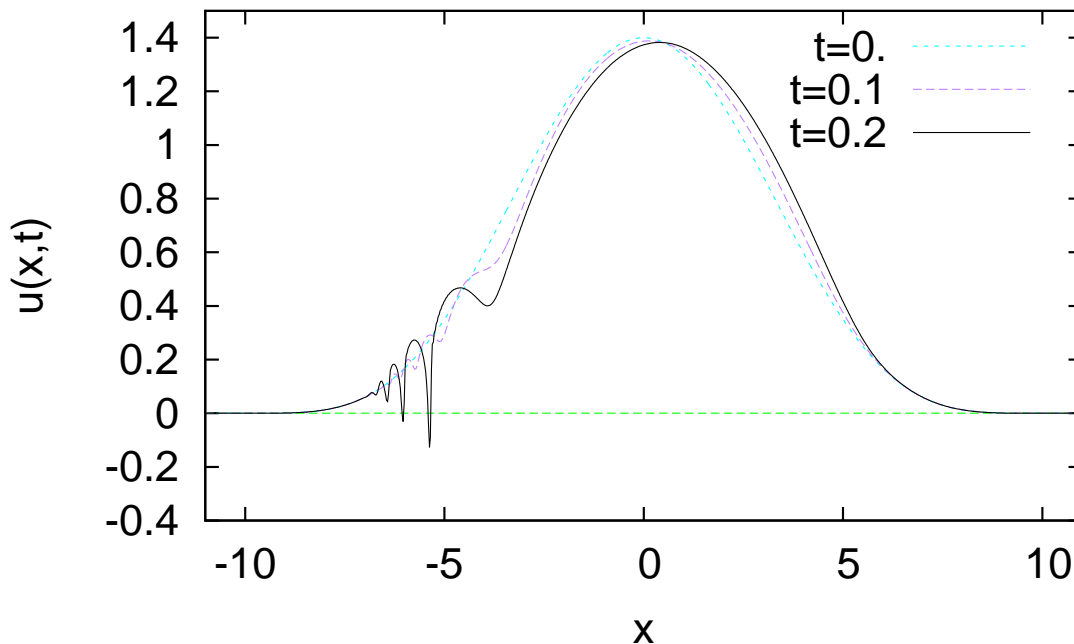


Figure 3.14: Initial phase of the decomposition of the profile $u(x, 0) = \cos^4(\frac{\pi x}{20})\chi_{[-10,10]}(x)$, showing in detail the spiky oscillations formed close to the left edge of the support. As compared to the data in Figure 3.13, the oscillations are more pronounced, but appear to have the same shape. These data were obtained with $\eta_2 = 0$ and $\eta_4 = 10^{-4}$.

particular we have checked that this part of the plot, as well as the position of this largest shock front, are robust against decreasing the value of η_4 .

Singularity in initially positive data Finally, we consider also for the $K(4, 4)$ equation the evolution of initial data bounded away from zero and we find clear evidence that for some choices of initial condition, the solution touches down reaching the value $u = 0$ and develops a singularity. Here we consider $u(x, 0) = 1.1 + \sin(\frac{\pi x}{10})$, with periodic boundary conditions. As illustrated in Figure 3.15, the solution approaches $u = 0$ around time $t \sim 0.37$. These data were obtained with $\Delta x = 20/512 \sim 0.040$ and with no added dissipation $\eta_4 = 0$. The singularity formed appears to have again the shape of a sequence of spikes with an infinite derivative.

3. Nonlinear dispersion and compactons. Numerical studies

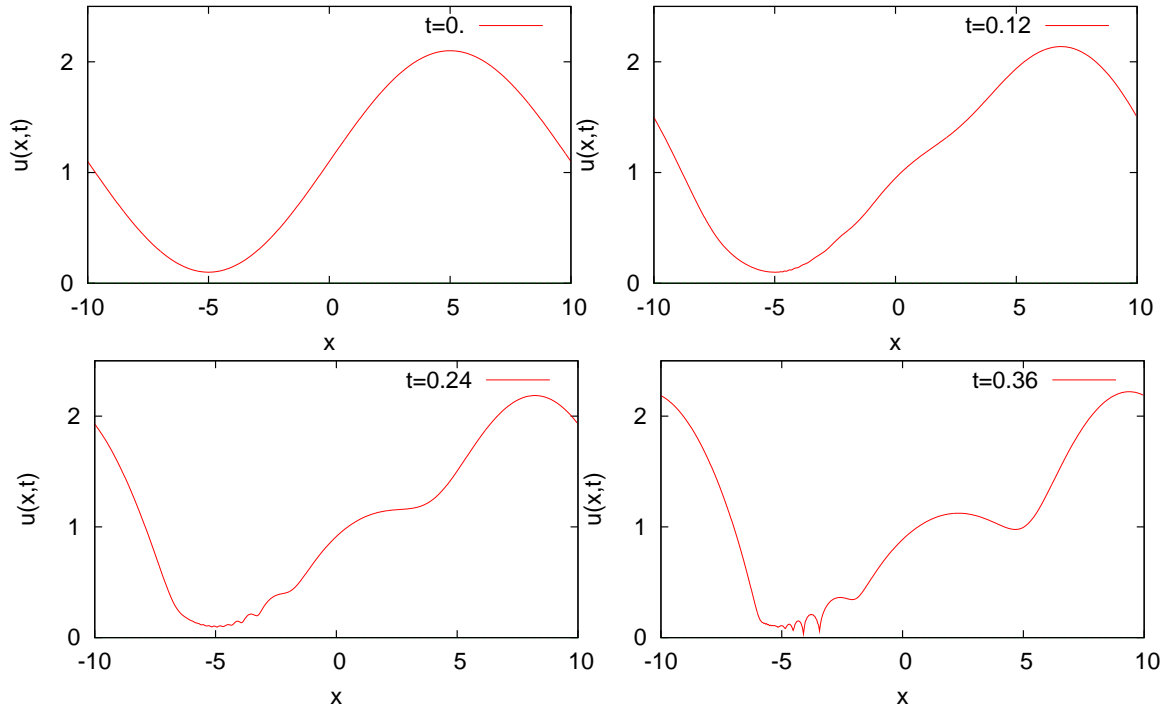


Figure 3.15: $K(4,4)$ equation: evolution of the smooth positive profile $u(x,0) = 1.1 + \sin(\frac{\pi x}{10})$. It is shown how this profile approaches the line $u = 0$ forming a number of singular spikes. Data obtained with $\eta_2 = \eta_4 = 0$.

3.5 Summary of the results of this chapter

In this chapter we presented new numerical investigations of the behaviour of the $K(2,2)$ and $K(4,4)$ equations. Most of these findings are a confirmation of previous studies such as Defrutos *et al.* [1995]; Levy *et al.* [2004]; Mihaila *et al.* [2010b]; Rosenau & Hyman [1993]; Rus & Villatoro [2007a]. In these studies, the $K(4,4)$ equation was not considered in the same detail, but our simulations indicate that – apart from the local characteristics of the singularities – its dynamics is extremely similar to that of the $K(2,2)$ model. Our numerical results confirm that, for both the models considered, colliding compactons are able to re-emerge from the interaction unscathed, leaving behind a small ripple with an internal shock layer. We also investigated the evolution of positive, piecewise-smooth initial conditions supported on a single interval, making the following observations:

3. Nonlinear dispersion and compactons. Numerical studies

- Close to the *right* edge, the solution remains smooth in the interior of the support. If the solution has initially a mild behaviour close to the edge point, a waiting time ensues¹, during which the interface steepens without developing oscillations; afterwards, the support starts expanding rightwards. We are unaware of other numerical observations of this behaviour.
- As reported in many works starting from Rosenau & Hyman [1993], a number of right-moving compactons emerge and completely separate from the initial condition.
- Close to the *left* edge of the support, the solution develop oscillations that grow singular forming a sequence of shocks. These oscillations were also observed in Levy *et al.* [2004] in the case of the K(3,3) equation. In Rosenau & Hyman [1993], it was reported that solutions of the K(2,2) equation with an initial support narrower than the width of a travelling compacton develop very strong singularities. However this was not analysed further. Our simulations indicate that these singularities are present for any initial width, although they are more pronounced in the case of a narrow initial support. In general the numerical evolution with the addition of viscosity is stable, leading to the development of a negative portion of the solution, which decays into a number of leftmoving antcompactons. This has also been observed in Mihaila *et al.* [2010b].

In agreement with Defrutos *et al.* [1995], we found that the formation of shocks appears to occur only at points where $u = 0$ and $u_x > 0$ ². It appears that the only case in which a shock is not formed at such points is the edge of exact compacton solutions.

A numerical observation which we did not find elsewhere in the literature is that initial conditions bounded away from zero can touch down reaching the value $u = 0$. Theorem 8 of Wright & Ambrose [2012] implies that they then develop a singularity; this was clearly visible in our data.

¹ As required by the theorems of Ambrose & Wright [2010].

² This is in a way reminiscent of the breakup results for the Camassa-Holm equation (see the Steepening Lemma in Camassa *et al.* [1994]).

3. Nonlinear dispersion and compactons. Numerical studies

Finally, in Section 3.2.0.1 and Section 3.3.2.1 we have presented a heuristic argument to determine the shape of a compactly-supported solution close to a moving edge of the support.

Chapter 4

Numerical study of stability for an integrable compacton equation

Since their discovery in Rosenau & Hyman [1993], the soliton-like properties of compactons have been intensively investigated. However, as this research has been almost entirely based on numerical exploration, a deep understanding of these solutions and their stability is still lacking. In comparison, the properties of peakon solutions Camassa & Holm [1993] occurring in non-evolutionary equations are much better understood, due to the paradigm set by at least two completely solvable examples Camassa & Holm [1993]; Degasperis & Procesi [1999]. The existence of an integrable equation modeling the interaction of compactons would be a major step forward in understanding this class of solutions to nonlinear dispersive equations. A parallel, still unsettled question is whether integrability (or perhaps an approximate form of integrability) plays any role in explaining the quasi-elasticity of compacton interactions. In this chapter we study numerically an integrable nonlinear dispersive equation supporting compacton solutions. This equation was introduced by Rosenau in Rosenau [1996] where it was shown that it is linked to the MKdV equation through a non-local change of variables, and admits both travelling and stationary compactly supported solutions. As we describe below, numerical studies of the equation ¹ suggest that only stationary compacton solutions are stable. Despite the fact that the original goal of

¹This equation was already studied numerically by Hyman and Rosenau, in an unpublished work cited in Rosenau [2006].

4. Studies of stability for an integrable compacton equation

finding an integrable paradigm for the dynamics of the $K(m, n)$ models was not accomplished, the observation of unstable compacton solutions is interesting in itself. An intuitive explanation – which can be found already in Rosenau [2006] – comes from the structure of the phase space of travelling wave solutions: the model admits infinitely many distinct compactly-supported travelling solutions with the same speed. Introducing a deformation of the equation interpolating between the integrable case and the Rosenau-Hyman $K(4, 4)$ model, this heuristic criterion can be used to determine the value of the deformation parameter at which the exchange of stability properties between stationary compactons and travelling compactons takes place. A similar *exchange of stability* between stationary leftons and travelling peakon solutions was discovered in Holm & Staley [2003]¹ in a one-parameter family of equations arising in water wave theory; this result has been rigorously established in Hone & Lafortune [2014].

After this work had been completed, we learnt that the main results of this chapter are already contained in Rosenau [2006]. However, since the numerical work of Hyman and Rosenau is unpublished we believe that the present work is a useful complement. In Section 4.4 we list in detail which claims of this work are believed to be new.

4.1 Integrable quasi-linear equations, hodograph transformations and the Lagrange map

Several examples of integrable compacton-supporting equations have been pointed out in the literature, for instance see Fokas *et al.* [1997]; Olver & Rosenau [1996]; Rosenau [1996]; Sakovich [2003]. In this section we will review these results using the perspective of Clarkson *et al.* [1989] on the classification of integrable quasi-linear equations.

The problem of classifying all the integrable equations of a given form is one of the main topics the theory of integrable systems, and different perspectives exist, such as the symmetry approach Mikhailov & Sokolov [2009]; Mikhailov

¹The expression “exchange of stability” is quoted from this paper

4. Studies of stability for an integrable compacton equation

et al. [1987, 1991] or Painlevé tests (see Hone [2009]; Kruskal *et al.* [1997] for reviews).

For 3rd order evolutionary semilinear equations, namely equations of the form

$$u_t = u_{xxx} + G(u_{xx}, u_x, u), \quad (4.1)$$

where G denotes a generic function, this problem was solved in Svinolupov & Sokolov [1982]; Svinolupov *et al.* [1983], proving that an equation of this type is integrable if and only if it can be transformed, through a *local* change of variables, to one of the following eight equations:

1. $u_t = u_{xxx} + \gamma u_x$ (Linear Third Order Equation)
2. $u_t = u_{xxx} + uu_x + \gamma u_x$ (KdV Equation)
3. $u_t = u_{xxx} + u^2 u_x + \gamma u_x$ (MKdV Equation)
4. $u_t = u_{xxx} - \frac{1}{8}u_x^3 + (\alpha_1 e^u + \alpha_2 e^{-u} + \gamma) u_x$ (CDF Equation)
5. $u_t = u_{xxx} - \frac{3}{2}u_x u_{xx}^2 (1 + u_x^2)^{-1} - \frac{3}{2}\mathcal{P}(u)(u_x^2 + 1)u_x + \gamma u_x$
6. $u_t = u_{xxx} - \frac{3}{2}u_{xx}^2 u_x^{-1} + \alpha u_x^{-1} - \frac{3}{2}\mathcal{P}(u)u_x^2 + \gamma u_x$

where $\mathcal{P}(u)$ denotes one of Weierstrass' elliptic functions and $\alpha_1, \alpha_2, \alpha, \gamma$ are free parameters. By local change of variables, we mean one that transforms separately the coordinates (x, t) and the dependent variable u , plus possibly a potential transformation $u = f_x$ or $u_x = f$.

The classification of quasi-linear equations, namely equations that can be written in the form

$$\partial_t u = g(u) \partial_x^n u + f(u, \partial_x u, \dots, \partial_x^{n-1} u), \quad (4.2)$$

(where g and f are generic functions of their arguments) is in general much more difficult. In particular, it is known that Painlevé tests, which are the simplest algorithmic method to scan for the integrability of equations of a given class, are appropriate only for semi-linear equations (see Clarkson *et al.* [1989] for a discussion). To overcome this problem, the authors of Clarkson *et al.* [1989] point

4. Studies of stability for an integrable compacton equation

out that a quasi-linear equation of the form (4.2) can sometimes be transformed into the semi-linear equation:

$$\partial_\tau w = \partial_y^n w + h(w, \partial_y w, \dots, \partial_y^{n-1} w). \quad (4.3)$$

through a non-local change of variables defined as follows:

$$\begin{aligned} \tau &= t \\ y &= \int^x \phi(u(x', t)) dx' \\ w(y, \tau) &= u(x, t), \end{aligned} \quad (4.4)$$

where $\phi(u)$ is related to the function $g(u)$ in (4.2) by $\phi(u) = (g(u))^{-\frac{1}{n}}$. The transformation (4.4) is known as *extended hodograph transformation*. The proposal of Clarkson *et al.* [1989] is that a quasi-linear equation is integrable if and only if it can be mapped to an integrable semi-linear equation. An important point to stress is that the extended hodograph transformation is not always applicable, in the sense that in general (4.4) could lead to a non-local (integro-differential) equation, rather than to a semi-linear PDE as in (4.3). According to the proposal of Clarkson *et al.* [1989], all these cases are non-integrable. In order for the hodograph map to yield a local semi-linear PDE, a precise condition on the form of (4.2) must be met. For third order equations, the condition can be found in Proposition 2.2 of Clarkson *et al.* [1989], and reads:

$$\begin{aligned} &f(u, u_x, u_{xx}) \\ &= \frac{\partial}{\partial u} B(u, u_x) u_x + \frac{\partial}{\partial u_x} B(u, u_x) u_{xx} + \left(\frac{g''(u)}{g'(u)} - \frac{4}{3} \frac{g'(u)}{g(u)} \right) B(u, u_x) \\ &+ \left(\frac{g''(u) g(u)}{g'(u)} - \frac{g'(u)}{3} \right) u_x u_{xx}, \end{aligned} \quad (4.5)$$

where $B(u, u_x)$ is an arbitrary function and $g(u)$ is the same function as in (4.2). It is worth remarking that the Rosenau-Hyman $K(m, n)$ equations for $n, m \in \mathbb{N}$, as well as the compacton equations introduced in Cooper *et al.* [1993] by Cooper, Shepard and Sodano (CSS), are not in this form and therefore not integrable.

4. Studies of stability for an integrable compacton equation

Let us now apply the hodograph transformation to the following generic equation:

$$u_t = u^3 u_{xxx} + \alpha u^2 u_x u_{xx} + \beta u u_x^3 + u^{r+1} u_x, \quad \alpha, \beta, r \in \mathbb{R}. \quad (4.6)$$

For $r > -1$, all of these equations admit compactly supported travelling wave solutions, as a result of the relative positive sign between the highest derivative term and the convective term. Notice that the class of equations (4.6) is quite general: since we can change the power of the non-linearity of the dispersive term by a transformation of the form $u \rightarrow u' = u^m$, this ansatz encompasses all cases in which the dispersive term is a homogeneous polynomial. The reason for the choice of $g(u) = u^3$ is that it will simplify some expressions later.

According to (4.5), the hodograph method is applicable only if $\beta = 0$ ¹. In that case, applying (4.4) yields

$$w_\tau = w_{yyy} + \frac{(\alpha - 3)}{2} \left(\frac{w_y^2}{w} \right)_y + \frac{r+1}{r} w^r w_y \quad \text{for } r \neq 0, \quad (4.7)$$

$$w_\tau = w_{yyy} + \frac{(\alpha - 3)}{2} \left(\frac{w_y^2}{w} \right)_y + (w \ln w)_y \quad \text{for } r = 0. \quad (4.8)$$

A complete classification of the integrable equations in (4.7) could be attacked for example with Painlevé analysis. This task is partially accomplished in Clarkson *et al.* [1989], where it is proved that, if one drops the convective term, then the equation is only integrable for $\alpha = 3$, $\alpha = \frac{3}{2}$ and $\alpha = 0$. For these particular values of α , it is easy to complete the classification:

- For $\alpha = 3$, (4.7) becomes the *generalized* KdV equation, which is known to be integrable if and only if $r = -1$, $r = 1$ or $r = 2$. These cases are related to the linear third order equation, the KdV equation and the MKdV equation, respectively.
- Secondly, the case $\alpha = \frac{3}{2}$ can be immediately obtained using a symmetry of the equation noticed in Clarkson *et al.* [1989]. In fact (4.7) is invariant for $w \rightarrow w' = (w)^{\alpha-1}$, $r \rightarrow r' = \frac{r}{\alpha-1}$, $x \rightarrow x' = \sqrt{\frac{r+1}{r+\alpha-1}} x$, $\tau \rightarrow \tau' = \left(\frac{r+1}{r+\alpha-1} \right)^{\frac{3}{2}} \tau$,

¹ Notice how this rules out, in particular, the K(4, 4) equation.

4. Studies of stability for an integrable compacton equation

$\alpha = 3$	$r = -1$ linear	$r = 1$ KdV	$r = 2$ MKdV
$\alpha = 3/2$	$r = -1/2$ linear	$r = 1/2$ KdV	$r = 1$ MKdV
$\alpha = 0$	$r = -1$ MKdV	$r = 1$ CDF	$r = 2$ CDF

Table 4.1: The table shows nine choices of α , r , with $\beta = 0$, that make equation (4.6) integrable, indicating the related integrable semi-linear equation.

$\alpha \rightarrow \alpha' = \frac{\alpha}{\alpha-1}$. This relates the case $\alpha = 3$ considered above to $\alpha = \frac{3}{2}$, and we find that the $\alpha = \frac{3}{2}$ equation is integrable if and only if $r = -\frac{1}{2}$, $r = \frac{1}{2}$ or $r = 1$.

- Finally, for $\alpha = 0$, (4.6) becomes the Harry Dym equation modified by a convective term. This case was analysed in Example 2.3 of Clarkson *et al.* [1989], showing that the only integrable cases are: $r = -1$, or $r = -2$, $r = 2$. For $r = -1$, the equation can be mapped to MKdV after applying an additional Cole-Hopf transformation: $q = \frac{w_x}{w}$. The latter two equations are examples of the Calogero-Degasperis-Fokas (CDF) equation.

These nine integrable cases are summarised in Table 4.1. It is tempting to conjecture that these are the only integrable cases in the class (4.6), although this would require a more rigorous analysis which is outside the scope of the present work.

Finally, let us remark that, when $g(u) = u^3$, the hodograph transformation becomes particularly simple. In particular, in this case the inverse transformation, which is a map from a semi-linear (4.3) to a quasi-linear equation (4.2) with $g(u) = u^3$, is the so-called *Lagrange map*, introduced by Rosenau in Rosenau [1996]. This transformation is defined by

$$\begin{aligned} x &= \int^y w(y', \tau) dy', \\ t &= \tau. \end{aligned} \tag{4.9}$$

4.2 An asymptotically stationary compacton equation

The focus of the rest of this chapter will be on the equation corresponding to $\alpha = 3$, $r = 2$. In order to be more uniform with the conventions of Chapter 3, let us make the substitution $t \rightarrow -t$. Then the equation reads:

$$0 = u_t + u^3 u_{xxx} + 3 u^2 u_x u_{xx} + u^3 u_x, \quad (4.10)$$

and is related by the Lagrange map (4.9) to the modified KdV (MKdV) equation in the form:

$$0 = w_t + w_{yyy} + \frac{3}{2} w^2 w_y. \quad (4.11)$$

The MKdV equation is exactly solvable for any initial condition through the inverse scattering method Ablowitz & Segur [1981]; Gardner *et al.* [1967]. However, as pointed out in Rosenau [1996] it is not always possible to translate solutions of the MKdV equation into solutions of (4.10), since in the presence of sign changes the Lagrange map is ill-defined, leading to a multi-valued profile for u . This problem is relevant since typical solutions of the MKdV equation do not preserve their sign. Moreover, we are particularly interested in studying solutions of (4.10) with a compact support. In general, they would correspond to solutions (4.11) defined on an interval with non trivial boundary conditions.

Let us consider in more detail some properties of the transformation (4.9). The simplest case is the one in which $w(\cdot, t)$ is smooth and rapidly decaying at infinity. Then, $I = \int w \, dy$ is a conserved quantity. Assuming that $w(\cdot, t)$ is non-negative, the image of such a solution through (4.9) is supported on a *fixed* interval of width precisely equal to I . In particular, if $w(y, t)$ is exponentially decaying:

$$w(y, t) \sim e^{-k^2|y|} \quad y \sim \pm\infty, \quad (4.12)$$

then we find that $u(x, t)$ defined by (4.9) has a linear behaviour at the edges of

4. Studies of stability for an integrable compacton equation

its support:

$$u(x, t) \simeq k^2|x - e_{\pm}|, \quad x \sim e_{\pm}, \quad (4.13)$$

where e_- and $e_+ = e_- + I$ are the endpoints of the support.

Another relevant example is the case when $w(y)$ touches zero quadratically at a point a , namely

$$w(y) \sim (y - a)^2, \quad y \sim a. \quad (4.14)$$

(where we have omitted the time dependence for clarity). Then it can be checked that a is mapped into a point b where the solution to (4.10) has the behaviour

$$u(x) \sim (x - b)^{\frac{2}{3}}, \quad x \sim b. \quad (4.15)$$

Notice that (4.14) is the typical behaviour found when an initially positive solution of the MKdV equation crosses the $w = 0$ line and changes its sign. The corresponding solution to (4.10) approaches the line $u = 0$ forming a spike with the behaviour (4.15). This is illustrated in Figure 4.1. We point out that, given the fact that the equations share the same degree of nonlinearity, it is natural to speculate that the same shape characterises the spikes formed by solutions of the K(4, 4) touching zero (see Figure 3.14 and Figure 3.15 in the previous chapter).

For completeness we report the zero-curvature condition for (4.10), which can be derived directly from the corresponding formulation for the MKdV equation, and was written down in Sakovich [2003]. It can be checked that (4.10) arises as the compatibility condition (namely, $\partial_t U - \partial_x V + [U, V] = 0$) of the linear problem

$$\Psi_x = U\Psi, \quad (4.16)$$

$$\Psi_t = V\Psi, \quad (4.17)$$

4. Studies of stability for an integrable compacton equation

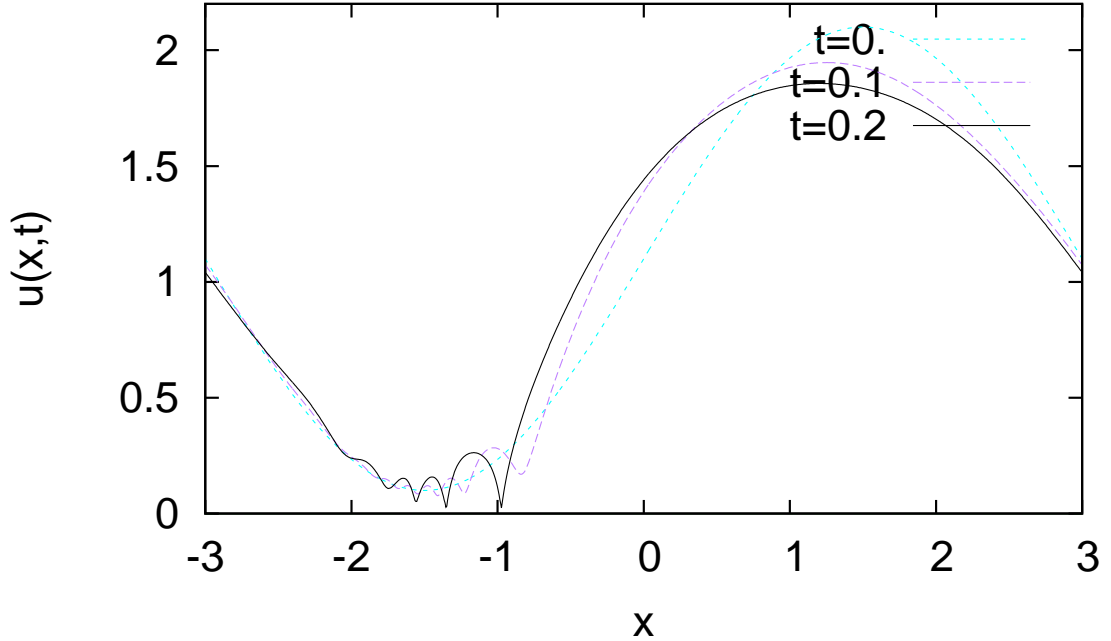


Figure 4.1: Numerical solution of the equation (4.10) with initial condition $u(x, 0) = 1.1 + \sin(\frac{\pi}{3}x)$. The solution approaches the line $u = 0$ forming spikes with the shape (4.15).

where $\Psi = \Psi(x, t)$ is a two-component vector and

$$U = \begin{pmatrix} \lambda u^{-1} & \frac{i}{2} \\ \frac{i}{2} & -\lambda u^{-1} \end{pmatrix}, \quad (4.18)$$

$$V = - \begin{pmatrix} -\lambda(uu_{xx} + u_x^2) + 4\lambda^3 & 2i\lambda^2 u + i\lambda uu_x \\ 2i\lambda^2 u - i\lambda uu_x & \lambda(uu_{xx} + u_x^2) - 4\lambda^3 \end{pmatrix}, \quad (4.19)$$

where λ is the spectral parameter. Notice that, as one can see in (4.18), the linear problem is strongly singular in correspondence of initial data that come close to $u = 0$, in particular for compactly supported initial data. Despite this difficulty, studying (4.10) directly with the method of the inverse spectral transform would naturally be very interesting.

4.2.1 Special solutions

Some important explicit solutions to (4.10) were found in Rosenau [1996]. In this section we review these results. The first solution is a stationary compacton

4. Studies of stability for an integrable compacton equation

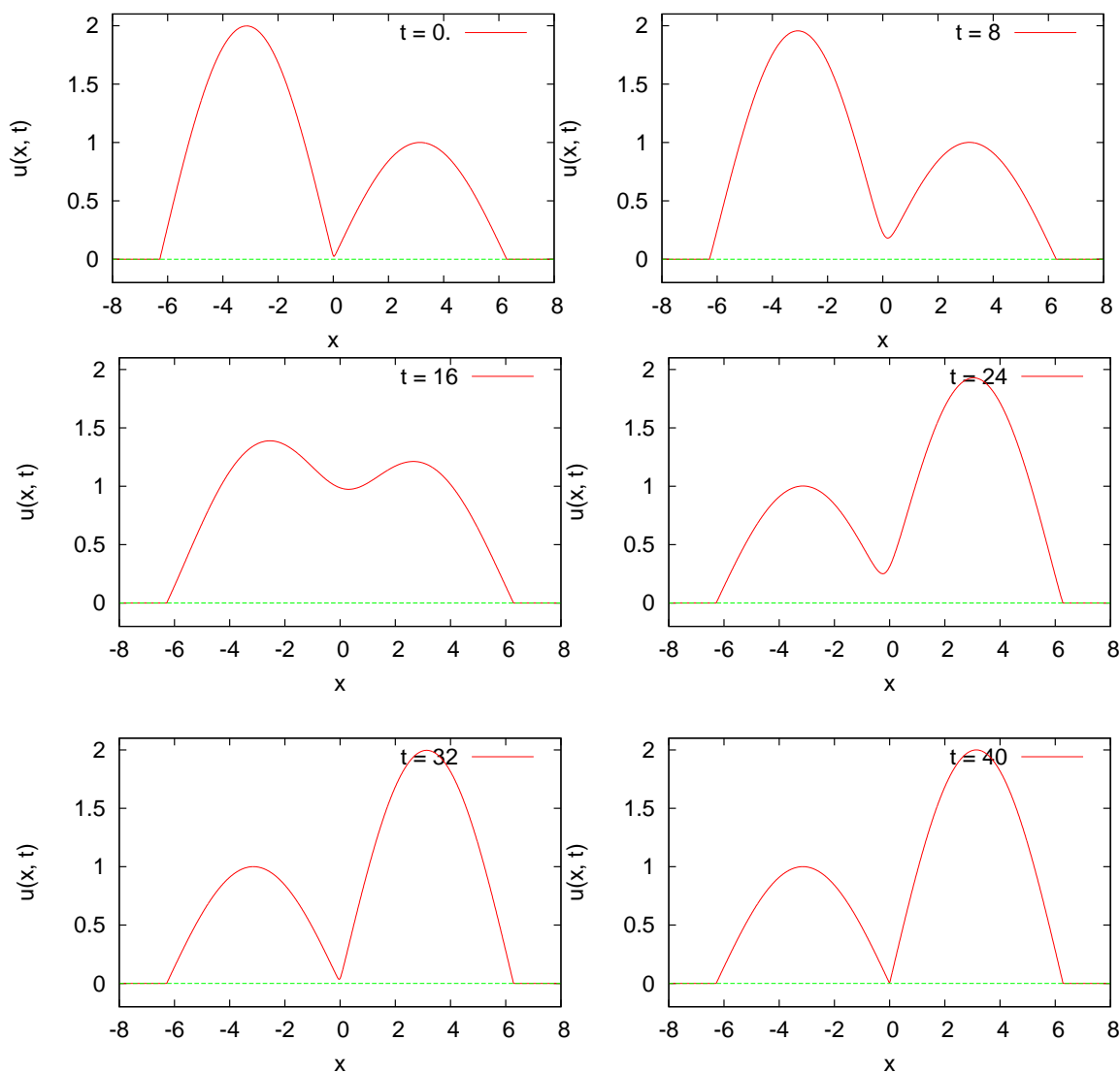


Figure 4.2: Snapshots of an asymptotically stationary two-compacton solution. The two constituent solitons in the related solution to MKdV have momenta $k_1 = 2$, $k_2 = 1$.

solution:

$$u(x, t) = \begin{cases} A \cos\left(\frac{x-x_0}{2}\right) & |x - x_0| < \pi \\ 0 & |x - x_0| > \pi \end{cases}, \quad (4.20)$$

with $x_0, A \in \mathbb{R}$. This is the image of the one-soliton solution of the MKdV equation under the Lagrange map.

Secondly, since multi-soliton solutions of the MKdV equation are everywhere

4. Studies of stability for an integrable compacton equation

positive, one can similarly apply the Lagrange map obtaining multi-compacton solutions. The form of these solutions can be found in Rosenau [1996]. The evolution of this asymptotically static N -compacton solution has been described in Rosenau [1996] and is illustrated in Figure 4.2. The dynamics consists uniquely in the rearranging of the maxima of the solution. As $t \rightarrow \pm\infty$, the solution approaches a train of N stationary compactons of the form (4.20), ordered according to their heights, increasing from left to right (from right to left) for $t \rightarrow +\infty$ ($t \rightarrow -\infty$, respectively). Notice that the support of the solution remains fixed during the whole evolution and is precisely equal to

$$I_N = 2N\pi. \tag{4.21}$$

Finally, in Rosenau [1996] is shown that (4.10) admits the following travelling compacton solution:

$$u(x, t) = \begin{cases} 2(-c)^{\frac{1}{3}} \cos^{\frac{2}{3}}\left(\frac{3}{4}(x - x_0 - ct)\right) & \left| \frac{3}{2}(x - x_0 - ct) \right| < \pi \\ 0 & \left| \frac{3}{2}(x - x_0 - ct) \right| > \pi \end{cases}, \tag{4.22}$$

where $x_0 \in \mathbb{R}$ is an arbitrary displacement and $c \in \mathbb{R}$ is the speed. This solution is the image, under the Lagrange map, of a single period of a stationary and spatially periodic solution to (4.11). Notice that the travelling compacton solution with positive amplitude has a negative speed: therefore it moves in the opposite direction with respect to the component compactons in the asymptotically stationary solution of Figure 4.2, which rearrange themselves shifting from left to right.

Instability of travelling compactons The numerical observations discussed in Section 4.3 confirm that – as was already reported in Rosenau [2006] – travelling wave compacton solutions (4.22) do not appear to play any role in the evolution of generic initial data. This points out that they are not stable (see Tao [2009] for different definitions of stability). On the contrary, as discussed in the previous chapter, compacton solutions of the $K(m, n)$ equations appear to resolve arbitrary initial conditions, akin to the behaviour expected from stable solitary wave solutions in semilinear equations (a discussion of the last statement,

4. Studies of stability for an integrable compacton equation

which is sometimes referred to as the *soliton resolution conjecture*, can be found in Tao [2009]).

Let us remark that the high degree of singularity of (4.22) at the endpoints of the support is not sufficient to explain this instability. In fact, the singularity of (4.22) is the same as that of travelling compacton solutions of the K(4, 4) equation, which certainly appear to be stable in all numerical studies (see Dey & Khare [1998] for arguments towards a proof of stability of the K(n, n) compactons). Besides, in Section 4.3 we do find examples of stable – but not travelling – solutions with the same degree of singularity as (4.22) at one of the edges of their support. In the next section we present a heuristic explanation for the instability of (4.22). This observation was made in Rosenau [2006], although it was not directly linked to instability.

4.2.2 A heuristic argument for the instability of travelling compactons

Let us consider a general travelling wave solution to (4.10). Making the substitution $u(x, t) \equiv v(x - ct)$ in (4.10) one finds:

$$c v_x = \partial_x \left(v^3 v_{xx} + \frac{1}{4} v^4 \right), \quad (4.23)$$

and integrating the equation twice yields:

$$(v_x)^2 = \frac{1}{v^2} \left(\frac{a_1}{2} - 2 c v + a_2 v^2 - \frac{1}{8} v^4 \right), \quad (4.24)$$

where a_1, a_2 are two arbitrary constants. The solution (4.22) is found after setting $a_1 = a_2 = 0$. However, notice that, a priori, for a fixed value of $c \neq 0$ equation (4.24) has an infinite family of solutions depending on a_1 and a_2 , and it can be proved that they are all supported on an interval. For the details of this proof see Appendix C. Let us consider the behaviour close to the edge points of the support where $v \rightarrow 0$:

$$v_x \sim \pm \frac{1}{v} \sqrt{\frac{a_1}{2} - 2 c v + a_2 v^2}. \quad (4.25)$$

4. Studies of stability for an integrable compacton equation

Clearly, the singularity is strongest for solutions with $a_1 \neq 0$, and this justifies setting this constant to zero (while we do not address this question rigorously, we point out that solutions to (4.24) with $a_1 \neq 0$ are very singular and may not be well-defined even in the weak sense). On the contrary, as long as $c \neq 0$, the leading singular behaviour is independent of a_2 , and the infinitely many solutions labelled by a_2 are all equally acceptable. These solutions have all the same singular edge behaviour as (4.22).

We can contrast this situation with the case of the K(4, 4) equation. In this case, the equation determining the shape of travelling waves is:

$$(v_x)^2 = \frac{1}{v^2} \left(K_1 + \frac{K_2}{v^4} + \frac{c v}{10} - \frac{v^4}{16} \right), \quad (4.26)$$

where $u(x, t) = v(x - c t)$ is a solution to $0 = u_t + (\partial_{xxx} + \partial_x) u^4$ and K_1, K_2 are integration constants. It is easy to see that the structure of (4.26) forces us to take $K_1 = K_2 = 0$ in order to avoid exceedingly strong singularities, therefore the solution is uniquely defined.

Hence, in the case of the K(4, 4) equation we find that travelling compacton solutions are uniquely determined by their speed, in analogy to the familiar case of solitons in semilinear equations (equivalently, there is a one-to-one relation between the speed and amplitude of travelling waves). On the contrary, in the case (4.10) there are infinitely many distinct travelling wave solutions with the same speed, which appears to be a clear sign of instability.

4.2.2.1 A family of deformations

In order to test this idea, let us consider a family of equations defined as follows:

$$0 = u_t + \partial_x \left(u^3 u_{xx} + \delta u^2 u_x^2 + \frac{1}{4} u^4 \right), \quad (4.27)$$

where δ is a parameter that interpolates between the two case studies we have just presented, i.e. the integrable equation (4.10) for $\delta = 0$ and the K(4, 4) equation for $\delta = 3$.

In Appendix C we study the travelling wave solutions of (4.27), and find that the separation between these two cases appears to be at $\delta = \frac{1}{2}$. Denoting a

4. Studies of stability for an integrable compacton equation

travelling solution as $u(x, t) = v(x - ct)$, we find that:

- a) For $\delta > \frac{1}{2}$ and a fixed value of $c \neq 0$, there is one and only one ¹ compactly supported solution with the scaling behaviour:

$$v(z) \sim L|z - e_{\pm}|^{\frac{2}{3}} \quad \text{as } z \sim e_{\pm}, \quad z \in \text{supp}, \quad (4.28)$$

where $L \in \mathbb{R}$ and e_{\pm} denote the two endpoints of the support. This solution satisfies

$$L = \left(\frac{9c}{4\delta - 2} \right)^{\frac{1}{3}}, \quad (4.29)$$

and its amplitude \bar{U} is given by

$$\bar{U} = + \left(c \frac{(\delta + 1)}{(\delta - 1/2)} \right)^{\frac{1}{3}}. \quad (4.30)$$

Moreover this orbit can be obtained as the limit of a family of smooth periodic orbits as their minimal distance from the line $v = 0$ vanishes.

- b) For $\delta = \frac{1}{2}$, the equation does not admit any compactly supported travelling solutions with $c \neq 0$.
- c) For all values of $\delta < \frac{1}{2}$ and $c \neq 0$, there are infinitely many compactly supported solutions with the same speed c and with the same edge behaviour specified by (4.28) and (4.29).

The proof of these properties can be found in Appendix C. Based on the qualitative difference between these two phases, it is natural to make the following conjecture:

- 1) For $\delta < \frac{1}{2}$, travelling compacton solutions are unstable, while the dynamics is dominated by stationary compacton solutions.
- 2) For $\delta > \frac{1}{2}$ the behaviour is more similar to the $K(m, n)$ equations and travelling compactons dominate the initial value problem. We expect stationary compactons to be unstable in this region.

¹ modulo translations $v(z) \rightarrow v(z + z_0)$, $z_0 \in \mathbb{R}$

4. Studies of stability for an integrable compacton equation

Notice that the stable stationary solution of (4.27) for $\delta < \frac{1}{2}$ can be found explicitly:

$$u(x, t) = \begin{cases} A \cos^{\frac{1}{1+\delta}}\left(\frac{\sqrt{1+\delta}}{2}(x - x_0)\right) & |x - x_0| < \frac{\pi}{\sqrt{1+\delta}} \\ 0 & |x - x_0| > \frac{\pi}{\sqrt{1+\delta}} \end{cases}, \quad (4.31)$$

with $x_0, A \in \mathbb{R}$. Notice that, for $\delta > \frac{1}{2}$, (4.31) is still formally a solution; however, its edge behaviour is more singular than (4.28).

We point out that in Rosenau [2006], Rosenau already arrived at the conclusions of this section considering a slightly more general family of models ¹.

4.2.3 Conservation laws and behaviour at the edge of the support

In this section, we make some further observations on the integrable structure of the equation and on its infinite hierarchy of conservation laws. In particular, we show that these classical conservation laws are not necessarily true for a generic weak solutions of the equation, and in particular that an infinite number of conservation laws is violated by any solution with a dynamic support.

In the case of (4.10), there is an infinite family of polynomial conservation laws, which can be constructed, for instance, exploiting the existence of a bi-Hamiltonian structure Magri [1978]. Let us review the bi-Hamiltonian formulation of (4.10), discussed in Olver & Rosenau [1996]. Making the substitution $u = 1/q$, (4.10) can be written as

$$q_t = \frac{1}{2}(\partial_x + \partial_{xxx})(1/q^2), \quad (4.32)$$

¹ Rosenau considered the family of equations

$$u_t + (u^m)_x + \frac{1}{b}(u^a(u^b)_{xx})_x = 0,$$

and, by a reasoning very similar to that described above, concluded that travelling (stationary) compactons dominate the dynamics for $\omega \equiv 1 + b - a > 0$ ($\omega \leq 0$, respectively).

4. Studies of stability for an integrable compacton equation

which can be presented in Hamiltonian form in two equivalent ways:

$$q_t = \mathcal{J}_i \frac{\delta}{\delta q} H_i, \quad i = 0, 1, \quad (4.33)$$

where $\frac{\delta}{\delta q}$ denotes functional differentiation, the two Hamiltonians are

$$H_0 = \int dx \, 1/q, \quad H_1 = \int dx \, \frac{1}{4} \left(\frac{q_{xx}}{q^4} - \frac{1}{q^3} \right), \quad (4.34)$$

and the two skew-symmetric operators \mathcal{J}_i ($i = 1, 2$) defining two compatible Hamiltonian structures are given by ¹

$$\mathcal{J}_0 = -\frac{1}{2}(\partial_x + \partial_{xxx}), \quad \mathcal{J}_1 = -\frac{1}{2}\partial_x q \, \partial_x^{-1} q \partial_x. \quad (4.35)$$

As explained in Magri [1978], one then has a semi-infinite sequence of local conserved quantities H_i , $i \in \mathbb{N}$ of the form

$$H_i = \int dx \, h_i, \quad (4.36)$$

where h_i is a function of q and its space derivatives, defined by the recursion

$$\frac{\delta}{\delta q} H_i = (\mathcal{J}_1)^{-1} \mathcal{J}_0 \frac{\delta}{\delta q} H_{i-1} \quad i \geq 0, \quad (4.37)$$

and satisfies a local conservation law of the form

$$\partial_t h_i = \partial_x j_i, \quad i \geq 0, \quad (4.38)$$

where the currents j_i can be computed by solving the relation

$$\left(\frac{\delta}{\delta u} H_i \right) u_t = \left(\frac{\delta}{\delta u} H_i \right) (u^3 u_{xx} + \frac{1}{4} u^4)_x = \partial_x j_i, \quad (4.39)$$

¹Notice that the bi-Hamiltonian structure defined by (4.35) is the same, after rescaling and sending $x \rightarrow ix$, as the one for the Fokas-Olver-Rosenau-Qiao (FORQ) equation, a non-evolutionary integrable equation with cubic nonlinearity derived in Fokas [1995]; Olver & Rosenau [1996]; Qiao [2006]. See Hone & Wang [2008] for a precise formulation of the bi-Hamiltonian structure for this model. This imaginary- x version of the FORQ equation is therefore a symmetry of (4.10). More precisely, it can be associated with the first of its nonvanishing negative flows, namely $q_t = \mathcal{J}_1 \frac{\delta}{\delta q} H_{-1}$, with H_{-1} given in (4.42).

4. Studies of stability for an integrable compacton equation

and are, in turn, polynomials in u and its derivatives.

Written in terms of the original variables of (4.10), the first two local conserved quantities are

$$H_0 = \int dx u, \tag{4.40}$$

$$H_1 = \int dx \left(uu_x^2 - \frac{1}{2}u^2 u_{xx} - \frac{1}{2}u^3 \right), \tag{4.41}$$

\vdots

Equation (4.37) defines also a sequence of non-local charges for $i < 0$, which can be generated starting from

$$H_{-1} = \int dx' dx'' q(x') \sin(|x' - x''|) q(x''). \tag{4.42}$$

However, the conserved charges with $i < 0$ appear irrelevant for our discussion, since we are mainly interested in vanishing boundary conditions for $u = 1/q$ and in particular in u compactly supported, and integrals such as the one defining H_{-1} above would be divergent.

Let us make an additional observation on the local conservation laws. Equations (4.38) imply that the quantities H_i are conserved for any smooth classical solution decaying fast enough at infinity. However we must be cautious when considering compactly-supported solutions, which are potentially singular at the endpoints of the support. To understand this issue, let us consider a solution that, as is the typical case in compacton equations, is supported on the interval $[e_-(t), e_+(t)]$ smooth in the interior of its support and continuous, so that $u \rightarrow 0$ as $x \rightarrow e_{\pm}(t)$. Then we find

$$\frac{d}{dt} H_i = j_i|_{x=e_+(t)} - j_i|_{x=e_-(t)}. \tag{4.43}$$

This shows that the invariance of H_i depends crucially on the edge behaviour of the solution.

It is useful to make some dimensional considerations. The quantities h_i and j_i can be seen as polynomials in u and in the derivative operator ∂_x . From (4.37)

4. Studies of stability for an integrable compacton equation

and (4.38), we see that

- h_i is homogeneous of degree $1 + 2i$ in u and has a maximum degree $2i$ in ∂_x .
- j_i has a homogeneous degree $4 + 2i$ in u and has a maximum degree $2(i + 1)$ in ∂_x .

These relations show that, if u vanishes and all its derivatives remain bounded at the edge points, as is the case for the asymptotically stationary multi-compacton solution described in Section 4.2.1, then the right hand side of (4.43) vanishes, simultaneously, for all $i \in \mathbb{N}^+$. This guarantees that the local conservation laws are all simultaneously satisfied.

However, we expect that, in the case of an equation with a nonlinear dispersive term which has a fourth-order non-linearity, more singular fronts can be formed. If the space derivatives of u diverge at the edge points, then dimensional considerations above show that, for higher values of i , it is increasingly difficult that the quantities h_i and j_i will be well defined.

The first currents in particular are

$$j_0(u, u_x, u_{xx}) = -u^3 u_{xx} - \frac{1}{4}u^4, \quad (4.44)$$

$$j_1(u, u_x, u_{xx}) = 2u^3 \left(u_{xx} + \frac{1}{4}u \right) \left(uu_{xx} + u_x^2 + \frac{1}{2}u^2 \right), \quad (4.45)$$

⋮

Requiring that j_0 vanish at the edge points, we obtain the condition

$$\lim_{x \rightarrow e_{\pm}(t)} u^3 u_{xx} = 0. \quad (4.46)$$

Under the assumptions we made on the solution, this is equivalent to

$$u(x, t) = o\left(|x - e_{\pm}(t)|^{\frac{1}{2}}\right), \quad x \sim e_{\pm}(t). \quad (4.47)$$

4. Studies of stability for an integrable compacton equation

However, the vanishing of j_1 requires that

$$\lim_{x \rightarrow e_{\pm}(t)} u^2 u_{xx} = 0.$$

The heuristic arguments presented in Section 3.2.0.1 and Section 3.3.2.1 show the same term should be related to the speed of motion of the interface. Following the same reasoning we conjecture the relation:

$$\frac{d}{dt} e_{\pm}(t) = \lim_{\substack{x \rightarrow e_{\pm}(t) \\ x \in \text{supp}}} u^2(x, t) u_{xx}(x, t), \quad (4.48)$$

which implies that an interface sufficiently regular close to the edge of its support should have, locally, the shape

$$u(z, t) \sim \left(-\frac{9}{2} \frac{d}{dt} e(t) \right)^{\frac{1}{3}} |z - e(t)|^{\frac{2}{3}}, \quad (4.49)$$

as $z \sim e(t)$, $z \in \text{supp}(u(\cdot, t))$. This is indeed the scaling behaviour of the travelling solution (4.22). Although this solution appears to be unstable, our numerical results show the existence of stable solutions with movable fronts. We conclude that for such solutions H_1 is not a conserved quantity, but instead satisfies the differential equation

$$\frac{d}{dt} H_1 = -2 \left(\left(\frac{d}{dt} e_+(t) \right)^2 - \left(\frac{d}{dt} e_-(t) \right)^2 \right). \quad (4.50)$$

This equation can be obtained from (4.43) plugging in (4.49). In the next section we evolve numerically different initial conditions and find several examples of stable solutions with a dynamic support. For positive initial data supported on an interval, we find that in general $\frac{d}{dt} e_-(t) < 0$, while $\frac{d}{dt} e_+(t) = 0$. In all these cases (4.50) can be verified numerically.

In the presence of interfaces with the scaling (4.49), the other local conserved charges H_i , $i \geq 2$ are ill-defined.

4.3 Numerical study

Numerical method To solve (4.10) and its deformations (4.27) numerically, we used a 4th order Padè numerical method, similar to the one used in the previous chapter to study the K(2, 2) and K(4, 4) equations. We refer the reader to Section 3.4.1 for a general description of the method, and to Appendix B for details. The errors in reproducing the exact asymptotically stationary two-compacton solution are reported in Table 4.2 for different values of the step size.

	$t = 1.6$	$t = 8.$	$t = 16.$	$t = 32.$	$t = 48.$
$\Delta x = 16./1024$	8.4×10^{-4}	9.9×10^{-3}	7.7×10^{-3}	8.9×10^{-3}	9.0×10^{-2}

Table 4.2: Values of the error estimate $\text{err}(t) = \sum_i |u_i(t) - u(x_i, t)| \Delta x$ for the numerical computation of the two-compacton solution of Figure 4.2.

As explained in the previous chapter, numerical schemes based on finite differences usually require the addition of a small dissipative term $\eta_2 u_{xx} - \eta_4 u_{xxxx}$ to prevent against numerical instabilities. We observe that, for the same Δx and initial condition, the values of η_4 and η_2 required for stability are much less in the case of (4.10) than for the K(4, 4) equation, by a factor of at least 10^3 . This reflects the fact that (4.10) is less singular and does not seem to develop any shock-type singularities. However, we observe that the addition of dissipation has the undesirable effect of distorting the stationary solutions (4.20) and induce them to slowly drift away from their stationary position. The magnitude of the dissipation-induced speed is listed in Table 4.3 for different choices of η_2, η_4 .

η_2	0.5×10^{-3}	0.5×10^{-4}	0.5×10^{-5}
speed	0.005	0.002	0.0005
η_4	2×10^{-5}	2×10^{-6}	2×10^{-7}
speed	0.004	0.002	0.001

Table 4.3: Magnitude of the dissipation-induced speed of a initial profile $u(x, 0) = \cos(\frac{x}{2})$ for different values of η_2, η_4 .

Notice that this speed is positive for positive-amplitude solutions. This makes its numerical origin clear, since genuine travelling compacton solutions have the

4. Studies of stability for an integrable compacton equation

opposite direction. This motion is very small, but is however an undesirable feature of the numerical scheme, which becomes particularly visible for long-time simulations.

To avoid this effect, our simulations of (4.10) were performed with $\eta_2 = \eta_4 = 0$. To ensure stability, we applied a smoothing filter in Fourier space. Moreover, in order to be completely confident on our numerical results, we limited our simulations to positive initial data and to rather short times.

4.3.1 Decomposition of positive initial data

We have performed several numerical experiments on the evolution of positive compactly-supported initial data. Before describing in more detail our results, let us list our main observations:

- The long-time outcome of every simulation is a stationary configuration, consisting of a train of stationary compactons, analogous to the $t \rightarrow \infty$ limit of the multi-compacton solutions presented in Section 4.2.1.
- The support appears to remain connected for all times, but, when it is not an exact multiple of 2π (the width of a stationary compacton solution) it can expand at its left edge, forming a sharp front obeying equation (4.49). The transition from the initial condition to this expanding profile appears to be non-smooth in some cases due to oscillations formed close to the left edge, and we suspect that this process is essentially of numerical origin.
- We did not observe any coherent travelling solution emerging from the initial data.
- When the exact solution (4.22) is used as an initial condition, then the addition of even a very small amount of smoothing causes the profile to relax, also in this case, towards an asymptotically static solution. On the contrary, if no smoothing is applied, the numerical solution appears wobbly and unstable.

We believe these observations are a strong indication that (4.10) has no stable travelling compacton solution. Let us now discuss some examples in more detail.

4. Studies of stability for an integrable compacton equation

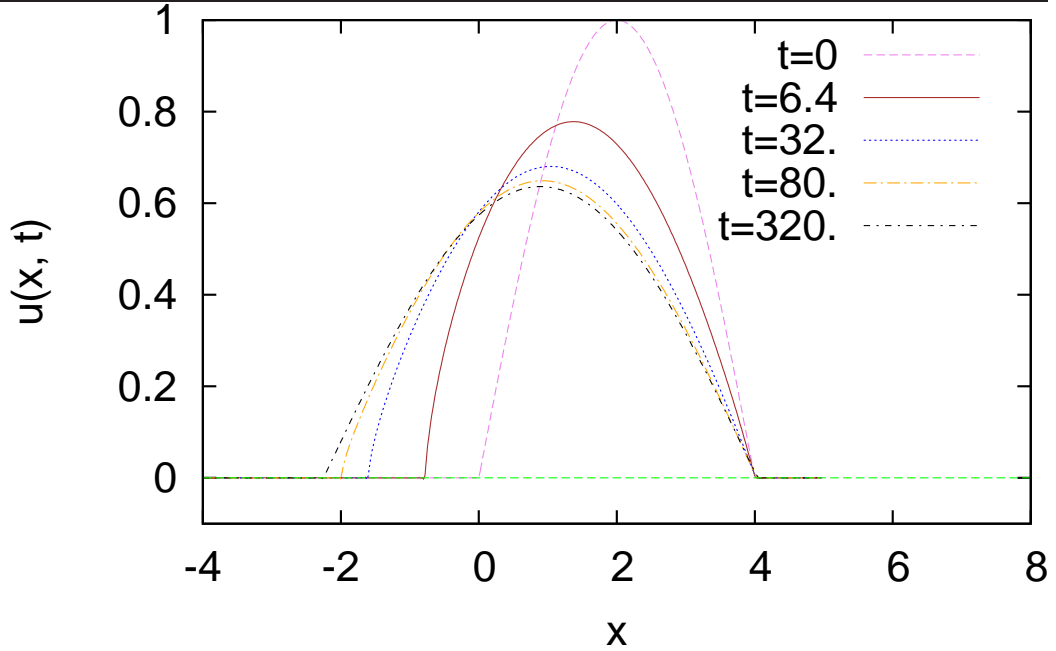


Figure 4.3: Decomposition of the initial condition $u(x, 0) = \cos(\frac{\pi}{4}(x-2))\chi_{[0,4]}(x)$. The solution develops a moving interface expanding leftwards and approaches a stationary compacton solution (4.20) as $t \rightarrow \infty$.

We have considered several profiles of the form:

$$u(x, t) = \begin{cases} \cos(\frac{\pi x}{W}) & |x| < W \\ 0 & |x| > W \end{cases}, \quad (4.51)$$

with different values of the parameter W . When the initial support is an exact multiple of the width 2π of the stationary compacton solution (4.20), we observed that none of its two edges moves in the evolution. For a generic value of W , the support readjusts itself with a characteristic mechanism, illustrated in two examples in Figures 4.3 and 4.4. First, there is a relatively quick transition during which the profile acquires the shape

$$u(x) \sim |x - \zeta_0|^{\frac{2}{3}} \quad (4.52)$$

at the left endpoint of the support (denoted by ζ_0). We argue that this transition is essentially numerical, as we will explain more precisely below. However, once the interface (4.52) is formed, the solution appears to be stable. The left endpoint of the support starts moving leftwards, following (4.48). The trajectories traced

4. Studies of stability for an integrable compacton equation

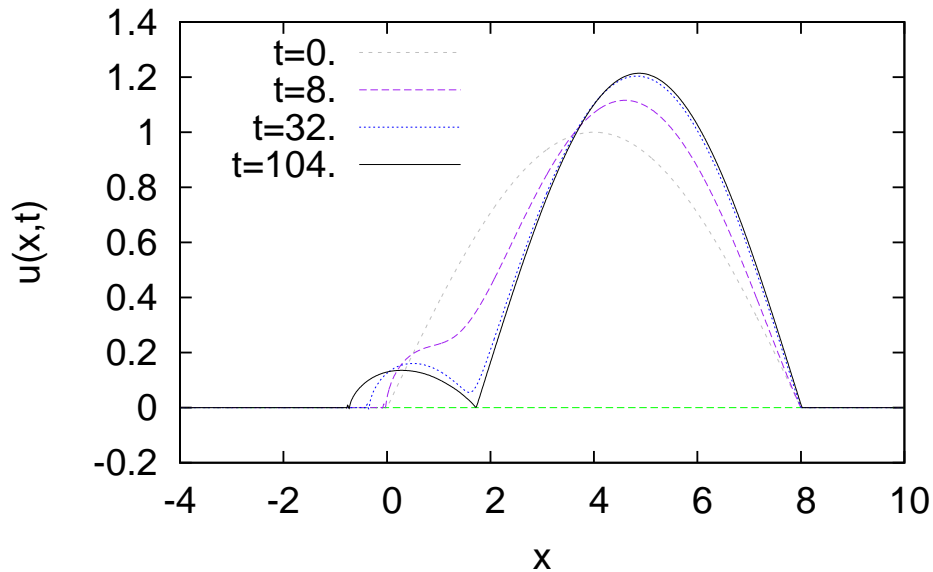


Figure 4.4: Decomposition of the initial condition $u(x, 0) = \cos(\frac{\pi}{8}(x-4))\chi_{[0,8]}(x)$. The solution appears to approach a train of two stationary compacton solutions for large times.

by the left edge of the support and by the maximum of the solution are illustrated in Figure 4.5 for the same data of Figure 4.3. Eventually, this motion slows down as the length of the support approaches the closest greater integer multiple of 2π , and the solution relaxes towards a sequence of stationary compactons. Notice that, as can be seen in Figures 4.3 and 4.4, the right edge of the support does not move during the entire evolution.

Let us make a comment on the formation of the interface for initial conditions of the form (4.51). This steepening process is not smooth, due to the presence of small oscillations close to the left edge. Viewed through the lens of the Lagrange map, these oscillations correspond to the radiation formed in the corresponding solution of the MKdV equation¹. In practice, these oscillations occur on a very small scale and accumulate towards the endpoint, and are not resolved by our program, which transitions to a solution with the interface (4.52) and no oscillations. The only remnant of the original oscillations is sometimes visible in the simulations as a very tiny irregularity close to the interface, barely visible in Figures 4.3 and 4.4. In conclusion, we do not know if the initial problem with initial

¹ Notice that, since this radiation usually develops a negative part, they are potentially singular when transformed to the variables of equation (4.10).

4. Studies of stability for an integrable compacton equation

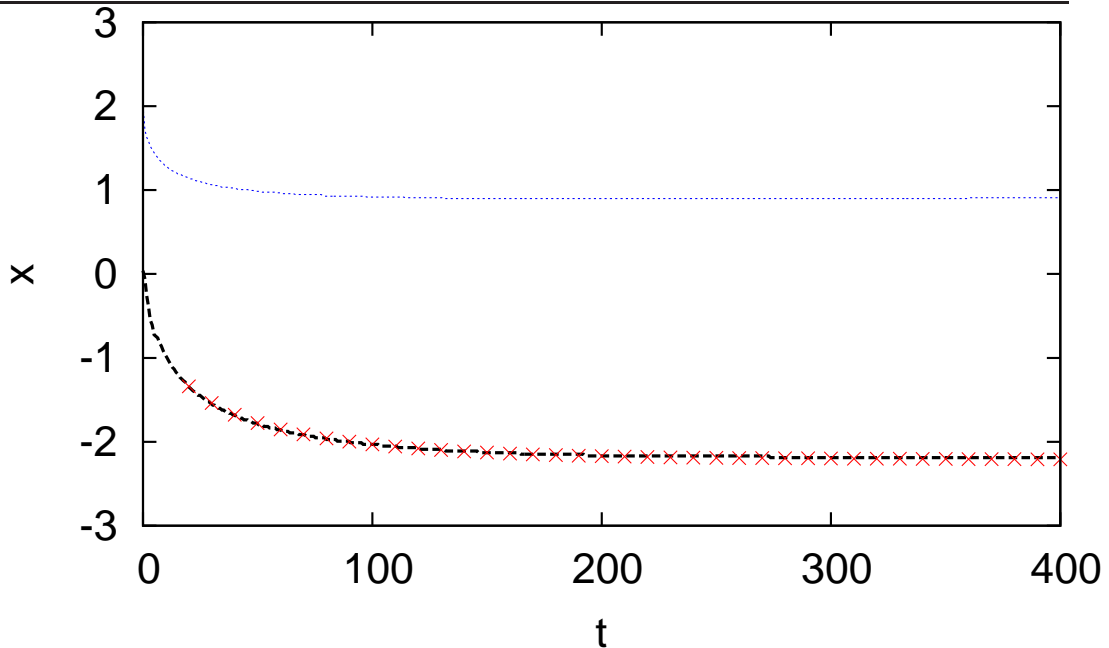


Figure 4.5: Space-time trajectories of the maximum of the solution (blue, dotted line) and of the left edge point of the support (black, dashed line) for the solution represented in Figure 4.3. The trajectory traced by the edge point matches precisely the prediction of (4.50) (represented by red crosses).

data (4.51) is well-posed and whether our numerical data reflect the solution of this problem rather than another, stable solution. However, we remark that the shape of the interface and its subsequent evolution is independent on any details of the numerical method. In Figure 4.5 is also shown a non-trivial test of our numerics. We have measured numerically the quantity H_2 at every time step of the simulation, and computed the left hand side of equation (4.50). The resulting prediction for the trajectory of the endpoint matches very well the one measured from our simulation.

We also have tested the evolution of initial profiles of the form:

$$u(x, 0) = \begin{cases} (x - a)^{\frac{2}{3}}(b - x), & x \in [a, b] \\ 0, & x \notin (a, b) \end{cases}. \quad (4.53)$$

In this case no oscillations were seen forming close to the left edge, and the evolution is similar to that of the profiles displayed in Figures 4.3 and 4.4.

4. Studies of stability for an integrable compacton equation

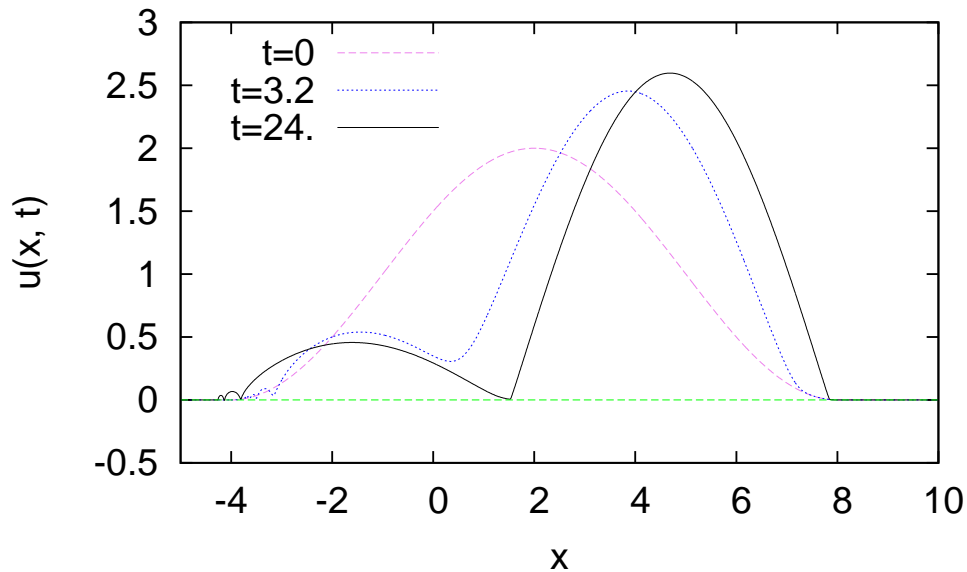


Figure 4.6: Numerical solution of the integrable $\delta = 0$ equation with initial condition $u(x, 0) = 2 \cos^2((x - 2)\frac{\pi}{12})\chi_{[-4,8]}(x)$.

Finally, we have considered the case of positive initial data with the scaling

$$u(x, 0) = \begin{cases} \cos^{\frac{2}{3}}(Wx), & x \in [-\frac{\pi}{2W}, +\frac{\pi}{2W}] \\ 0, & x \notin [-\frac{\pi}{2W}, +\frac{\pi}{2W}] \end{cases}, \quad (4.54)$$

and we find that, as soon as any amount of smoothing is added, the gradient u_x instantly becomes finite at the right interface, so that this endpoint of the support never moves and the evolution is very similar to that of Figure 4.3. Notice that this relaxation happens, in the presence of smoothing, even when the initial condition is the exact solution (4.22).

4.3.2 Comparison with other equations with $\delta \neq 0$

Finally, we have tested other equations in the family (4.27). Figures 4.6, 4.7 and 4.8 present the decomposition of an initial condition $u(x, 0) = 2 \cos^2(\frac{\pi}{6}x)$ for $\delta = 0, 1/4$ and $3/4$, respectively. The resulting evolution is very similar in the three cases. A solitonic structure is formed on the right part of the support. We stopped the simulation when this structure was well-resolved, and checked that it matches very well the stationary compacton solution (4.31) for $\delta = 0$ and $\delta = \frac{1}{4}$, and the travelling solution described by (4.28-4.29, 4.30) for $\delta = \frac{3}{4}$, confirming our

4. Studies of stability for an integrable compacton equation

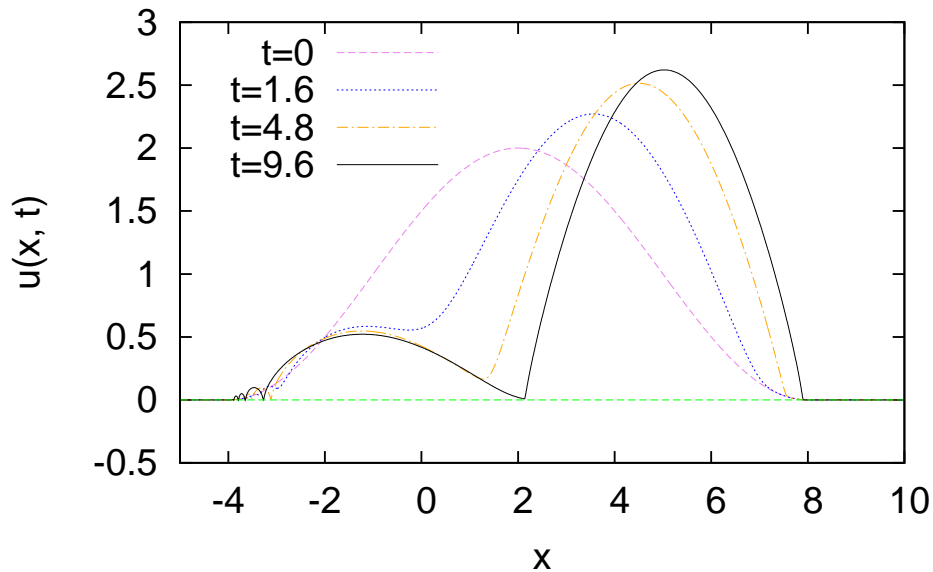


Figure 4.7: Numerical solution of the deformed $\delta = 1/4$ equation with initial condition $u(x, 0) = 2 \cos^2((x - 2)\frac{\pi}{12})\chi_{[-4,8]}(x)$. The structure emerging on the right fits very well with the shape of a stationary compacton solution.

expectation. The steepening appears to be smooth, with the solution remaining monotonic in a fixed neighbourhood of the edge point. In the case $\delta = 0$, u_x reaches a finite value at the right endpoint, while it diverges in the remaining two cases. For $\delta = 0$, the right edge of the support does not move from its initial position, while for $\delta = \frac{1}{4}$ we observed a small rightwards displacement. For $\delta = 3/4$, the solution approaches a constant speed, while in the remaining two cases it slows down and appears to come to rest asymptotically.

Notice that this structure cannot be mistaken for a travelling compacton. In fact, positive amplitude travelling compacton solutions for $\delta < \frac{1}{2}$ move with negative speed according to (4.28-4.29): therefore, if these solutions were stable, we would expect them to emerge from the *left* edge of the initial data. Instead, we observe that, in all three cases, oscillations are formed close to the left edge: compared to the case of a linear behaviour at the edge point (4.51), these oscillations occur on a much larger scale and appear to be stable, persisting for the duration of the simulation. In all cases we have considered, no travelling structure was seen emerging from the left endpoint.

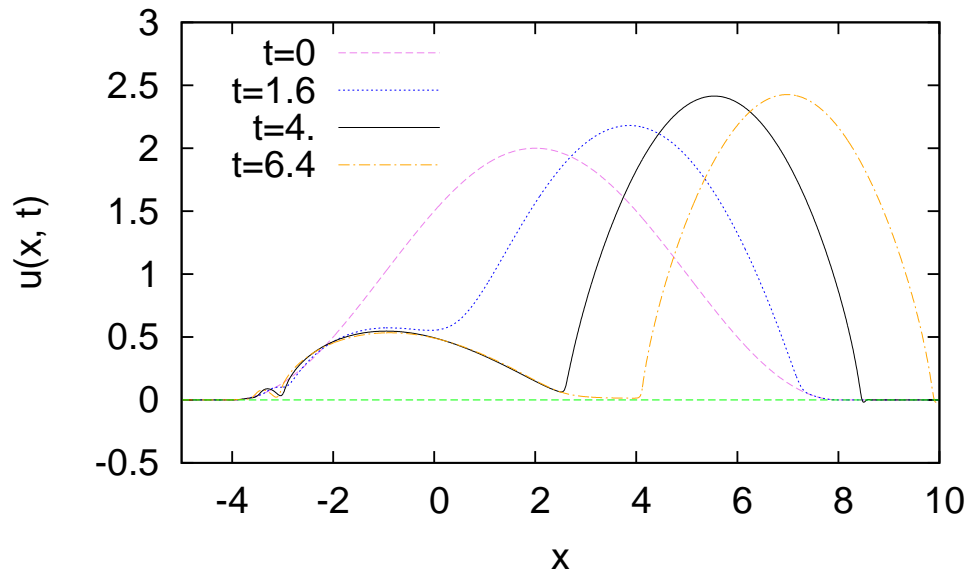


Figure 4.8: Numerical solution of the deformed $\delta = \frac{3}{4}$ equation with initial condition $u(x, 0) = 2 \cos^2((x - 2)\frac{\pi}{12})\chi_{[-4,8]}(x)$. The structure emerging from the right is a travelling compacton solution with speed approximately $c \sim 0.60$.

4.4 Summary of the results of this chapter

In this chapter we have discussed the integrable equation (4.10) and presented a numerical study of the evolution of compactly-supported initial data. The equation was also studied numerically in an unpublished work by Hyman and Rosenau, cited in Rosenau [2006]. Our results confirm the discovery made in the latter paper that the initial value problem is dominated by stationary compacton solutions of the shape (4.20). On the contrary, travelling compactons do not contribute to resolve generic initial conditions.

We described the fact that travelling compacton solutions to this model do not admit a unique relation between speed and amplitude, and we argued that this can be seen as a heuristic signal of instability. We discussed how, based on this criterion, one can recognize two phases in the one-parameter family of models (4.27), separated at the parameter value $\delta = \frac{1}{2}$.

In one sentence, this stability conjecture is as follows:

For $\delta \leq \frac{1}{2}$, the models (4.27) do not have stable travelling compacton solutions, while stationary compacton solutions are stable; for $\delta > \frac{1}{2}$, these stability properties are exchanged.

4. Studies of stability for an integrable compacton equation

This statement – apart from the different formulation – is not original, as it is implied by the results of Rosenau [2006], where a slightly more general parametric family of models is considered. Also the nonuniqueness of the relation between speed and amplitude of compactons was observed in that paper, see Section 3.2 therein.

However some of the results of the present work are new. They are listed below:

- In the work of Rosenau, it was observed that, in the parametric region where the evolution is dominated by stationary compactons, their edge behaviour is milder than that of travelling compactons, and vice versa.

Quoting from (Rosenau [2006], page 2):

“A selection principle seems to be at work: among different patterns for compactification, *the least singular pattern is the one to emerge*.(...) numerical simulations show that the only compactons to emerge are the ones with maximal smoothness (or, which amounts to the same, minimal singularity).” (italics in original)

However, since the numerical results are described very briefly, in Rosenau [2006] it is not clarified whether all solutions with the most singular scaling are necessarily forbidden.

Our data (see Section 4.3) clearly show that this is not the case, and that the instability is specific to exact travelling compacton solutions. In fact we showed that equation (4.10), despite not having stable travelling compacton solutions, admits stable solutions with the scaling $u \sim x^{\frac{2}{3}}$ – the same scaling as for travelling compactons – at the left edge of the support. These solutions are associated to the evolution of initial conditions with support not an exact multiple of 2π , and have a dynamic support.

- A second original observation of this chapter is that, for any solution of (4.10) with a dynamically evolving support, all the local conservation laws of this integrable equation are violated due to singular boundary terms across the edge of the support.

4. Studies of stability for an integrable compacton equation

Finally, we remark that the stability conjecture stated above is reminiscent of the exchange of stability between *peakons* and *leftons* studied in Holm & Staley [2003]; Hone & Laforune [2014] for a one-parameter family of equations arising in water wave theory.

Chapter 5

Conclusions

In the first part of the thesis, we have reported the content of the two papers Cavaglià *et al.* [2011], Cavaglià & Fring [2012]. In Chapter 1, we analysed several travelling solutions to the complex KdV equations and its \mathcal{PT} -symmetric deformations. These examples illustrate the rich behaviour displayed even by such simple solutions as a consequence of their extension to the complex domain. In Chapter 2, we have addressed more specifically the questions raised in Bender & Feinberg [2008] on the effect that a \mathcal{PT} -symmetric deformation has on the shock phenomenon in the inviscid Burgers equation. We were able to describe in detail how the properties of this singularity are altered by the deformation, contradicting some of the conclusions of Bender & Feinberg [2008].

In the second part of the thesis, we focused on the properties of compacton solutions to degenerate dispersive equations. Chapter 3 is an introduction to the subject, and presents original numerical investigations of the properties of two equations in the Rosenau-Hyman family, the K(2, 2) and K(4, 4) equations. These numerical experiments, on the one hand, confirmed the observations of other authors on the properties of these equations; on the other hand, they served as a term of comparison for the studies of the Chapter 4, where we investigated numerically one of the few known compacton-supporting integrable equations. This equation, which was introduced in Rosenau [1996] and shown to have both stationary and travelling compacton solutions, reads

$$0 = u_t + u^3 u_{xxx} + 3 u^2 u_x u_{xx} + u^3 u_x. \quad (5.1)$$

This model was studied numerically by Hyman and Rosenau in an unpublished work. As discovered in Rosenau [2006], it displays a radically different behaviour as compared to the $K(m, n)$ equations, and the initial value problem is dominated by asymptotically stationary solutions. We confirmed this claim with an independent numerical study, arguing that the underlying reason for this behaviour is the instability of travelling compacton solutions. This is signalled by the fact, already noticed by Rosenau, that the relation between speed and amplitude of travelling compacton solutions to this equation is not unique. We made some new observations: we demonstrated numerically the existence of solutions with an expanding support, and pointed out that, for such solutions, almost all the local conservation laws of this integrable model are spoiled due to singular boundary terms across the edges of the support.

Let us comment on some open directions of research related to this work.

First, it would be very desirable to establish rigorously the stability conjecture described above, which is still supported only by a limited amount of data.

Furthermore, the dynamics of equation (5.1) – which can be regarded as an interesting integrable model in itself – is far from completely understood. As we pointed out in Section 4.2, it is not even clear whether solutions can be globally defined in time, since the Lagrange map between this model and the MKdV equation indicates that singularities are formed for a very general class of initial conditions. On the numerical side, it would be very interesting to carry out a more detailed investigation. This may require adopting a different numerical method, in order to circumvent the limitations described in Section 4.3. In particular, the addition of dissipation required in all finite-difference-based schemes appears to yield drastic distortion effects. This has unfortunately prevented us from considering longer times in the simulations and explore all the regimes that were considered for the Rosenau-Hyman equations in Chapter 3. One could also try to study the initial value problem for (5.1) more directly using the inverse spectral method or exploiting more effectively the nonlocal transformation between this equation and the MKdV equation. The general initial value problem for initial conditions close to zero has not been studied, to the best of our knowledge, for any integrable equation that supports compacton solutions.

Most likely, since it describes a different dynamical phase, equation (5.1) is not directly relevant to the study of the most interesting properties of compactons in the Rosenau-Hyman equations and similar models. Establishing whether integrable equations with stable travelling compacton solutions exist is, in our opinion, an important open problem. For evolutionary equations, the most direct approach would be to study numerically other candidate models – such as the ones listed in Table 4.1. None of these equations have been thoroughly investigated in the literature; besides, there may be other, yet unknown, candidate equations, and it would be useful to complete the classification of Section 4.1. As a last note, we point out that the heuristic argument of Section 4.2.2, which we used to argue the instability in the case of (5.1), does not directly depend on the specific degree of the convective term of the equation. Therefore, the same reasoning would suggest that travelling compactons are not stable in any of the models with $\alpha = 3$ in Table 4.1.

Appendix A

Classification of two-dimensional stationary points

In this Appendix we recall the ten similarity classes characterizing the behaviour of the nondegenerate two-dimensional linear system:

$$\frac{d}{dt}v(t) = J.v(t), \quad (\text{A.1})$$

where $v(t)$ is a real 2-vector and J is a real 2×2 matrix with $\det(J) \neq 0$. Denoting by j_1 and j_2 the roots of the eigenvalue equation $\det(J - j_i) = 0$, the possible behaviours are classified as follows:

$j_i \in \mathbb{R}$	$j_1 > j_2 > 0$	unstable node
	$j_2 < j_1 < 0$	stable node
	$j_2 < 0 < j_1$	saddle point
$j_1 = j_2$, diagonal J	$j_i > 0$	unstable star node
	$j_i < 0$	stable star node
$j_1 = j_2$, nondiagonalizable J	$j_i > 0$	unstable improper node
	$j_i < 0$	stable improper node
$j_i \in \mathbb{C}$	$\text{Re}j_i > 0$	unstable focus
	$\text{Re}j_i = 0$	centre
	$\text{Re}j_i < 0$	stable focus

The system (A.1) arises from the linearisation of a nonlinear two-dimensional system around a stationary point, where J is the Jacobian at this point. Provided $\operatorname{Re}(j_1) \neq 0$ or $\operatorname{Re}(j_2) \neq 0$, the qualitative behaviour of the system around the stationary point is the same as that of its linearisation (see Theorem 7.1 in Hartman [1964]).

Appendix B

Details on the numerical schemes used to integrate compacton equations

In this Appendix we present the detailed form of the numerical schemes used for the integration of the K(2, 2) and K(4, 4) models and for equation (4.10) in Chapters 4 and 5. Let the interval I be the space domain. We discretize it by introducing a regular grid x_i , $i = 1, \dots, N$, with $x_{i+1} - x_i = \Delta x = |I|/N$. The numerical solution is represented as a N -dimensional vector $u_i(t) \simeq u(x_i, t)$, $i = 1, \dots, N$.

The method is based on the 4th order Padè approximant formulae introduced in Defrutos *et al.* [1995].

Padè approximant formulae Borrowing the notation of Mihaila *et al.* [2010a], we use the symbol E for the *shift operator* such that: $Ef(x) = f(x + \Delta x)$.

Let us introduce the finite difference operators:

$$\begin{aligned}
\mathcal{A}(\mathbf{E}) &= \frac{\mathbf{E}^{-2} + 26 \mathbf{E}^{-1} + 66 + 26 \mathbf{E}^1 + \mathbf{E}^2}{120}, & \mathcal{B}(\mathbf{E}) &= \frac{-\mathbf{E}^{-2} - 10 \mathbf{E}^{-1} + 10 \mathbf{E}^1 + \mathbf{E}^2}{24 \Delta x} \\
\tilde{\mathcal{B}}(\mathbf{E}) &= \frac{\mathbf{E}^{-2} - 8 \mathbf{E}^{-1} + 8 \mathbf{E}^1 - \mathbf{E}^2}{12 \Delta x}, & \mathcal{C}(\mathbf{E}) &= \frac{-\mathbf{E}^{-2} + 2 \mathbf{E}^{-1} - 2 \mathbf{E}^1 + \mathbf{E}^2}{2 \Delta x^3} \\
\mathcal{S}(\mathbf{E}) &= \frac{\mathbf{E}^{-2} + 2 \mathbf{E}^{-1} - 6 + 2 \mathbf{E}^1 + \mathbf{E}^2}{6 \Delta x^2}, & \tilde{\mathcal{S}}(\mathbf{E}) &= \frac{-\mathbf{E}^{-2} + 16 \mathbf{E}^{-1} - 30 + 16 \mathbf{E}^1 - \mathbf{E}^2}{12 \Delta x^2} \\
\mathcal{D}(\mathbf{E}) &= \frac{\mathbf{E}^{-2} - 4 \mathbf{E}^{-1} + 6 - 4 \mathbf{E}^1 + \mathbf{E}^2}{6 \Delta x^4}. & & \tag{B.1}
\end{aligned}$$

Then for $f(x) \in C^4$ we have the Padè approximant formulae:

$$\begin{aligned}
f_x(x) &= \tilde{\mathcal{B}}(\mathbf{E})f(x) + \mathcal{O}(\Delta x)^4, \\
\mathcal{A}(\mathbf{E})f_x(x) &= \mathcal{B}(\mathbf{E})f(x) + \mathcal{O}(\Delta x)^4, \\
f_{xx}(x) &= \tilde{\mathcal{S}}(\mathbf{E})f(x) + \mathcal{O}(\Delta x)^4, \\
\mathcal{A}(\mathbf{E})f_{xx}(x) &= \mathcal{S}(\mathbf{E})f(x) + \mathcal{O}(\Delta x)^4, \\
\mathcal{A}(\mathbf{E})f_{xxx}(x) &= \mathcal{C}(\mathbf{E})f(x) + \mathcal{O}(\Delta x)^4, \\
\mathcal{A}(\mathbf{E})f_{xxxx}(x) &= \mathcal{D}(\mathbf{E})f(x) + \mathcal{O}(\Delta x)^4.
\end{aligned}$$

Notice that, with a slightly different notation, these are the same formulae listed in Mihaila *et al.* [2010a]. However, we point out that there is a typo in this paper in the expression for $\tilde{\mathcal{B}}$.

Numerical scheme used for the $\mathbf{K}(m, n)$ equations To discretise the $\mathbf{K}(m, n)$ equation with the addition of two dissipative terms:

$$u_t + (u^n)_{xxx} + (u^m)_x - \eta_2 u_{xx} + \eta_4 u_{xxxx} = 0, \tag{B.2}$$

we use the finite-difference expression:

$$\mathcal{A}(\mathbf{E})\left(\frac{d}{dt}u_j(t)\right) - \mathcal{B}(\mathbf{E})(u_j^m) - \mathcal{C}(\mathbf{E})(u_j^n) - \eta_2 \mathcal{S}(\mathbf{E})(u_j) + \eta_4 \mathcal{D}(\mathbf{E})(u_j) = 0. \tag{B.3}$$

This is precisely the scheme denoted as $\mathcal{F}_{[444]}$ in Defrutos *et al.* [1995].

Numerical scheme used for equations (4.27) of Chapter 4 To represent the family of equations

$$u_t - \partial_x \left(u^3 u_{xx} + \delta u^2 u_x^2 + \frac{1}{4} u^4 \right) - \eta_2 u_{xx} + \eta_4 u_{xxxx} = 0, \quad (\text{B.4})$$

it is not possible to obtain a 4th order accurate scheme using only five points as in the case of the $K(m, n)$ equations.

A scheme based on nine points and fourth-order accurate in space is:

$$\begin{aligned} \mathcal{A}(\mathbf{E}) \left(\frac{d}{dt} u_j(t) \right) = & \mathcal{B}(\mathbf{E}) \left(\frac{1}{4} u_j^4 + p(\Delta x) u_j^3 \tilde{\mathcal{S}}(\mathbf{E})(u_j) + \delta u_j^2 (\tilde{\mathcal{B}}(\mathbf{E})(u_j))^2 \right) \\ & + \eta_2 \mathcal{S}(\mathbf{E})(u_j) - \eta_4 \mathcal{D}(\mathbf{E})(u_j). \end{aligned} \quad (\text{B.5})$$

This is the scheme used to obtain the results presented in Chapter 5. Notice that the formula contains a function $p(\Delta x) = -\frac{2}{3} \sin^2(\frac{\Delta x}{2})(\cos(\Delta x) - 7) = 1 + O(\Delta x)^4$, which is inserted in order to guarantee that, in the undeformed $\delta = 0$ case, the rhs is exactly zero when evaluated for the stationary solution $u(x) = \sin(x)$. This ensures that, at least to machine precision, the stationary solution is exactly preserved.

Time integration The system of ODEs presented above can be written schematically as

$$\mathcal{A}(\mathbf{E}) \left(\frac{d}{dt} u_i(t) \right) = Z(\mathbf{E})(u_i(t)) \quad (\text{B.6})$$

where $Z(\mathbf{E})$ is a symbol for the finite difference operators appearing on the rhs of equations (B.3) or (B.5).

Denoting a small time step as Δt the Crank-Nicolson integration scheme is

$$\mathcal{A}(\mathbf{E})(u_i(t + \Delta t) - u_i(t)) = \frac{\Delta t}{2} (Z(\mathbf{E})(u_i(t)) + Z(\mathbf{E})(u_i(t + \Delta t))) \quad (\text{B.7})$$

The computation of $u_i(t + \Delta t)$, $i = 1, \dots, N$ from the knowledge of $u_i(t)$ requires the solution of a system of algebraic equations at every time step. This can be achieved by applying Newton's iterative method. The numerical routines presented in Press *et al.* [1990] were extremely useful for this purpose.

Appendix C

Study of the compactly-supported travelling solutions of the equations (4.27)

In this Appendix we will analyze the traveling wave reduction of the family of equations (4.27), proving properties a), b) and c) stated in Section 4.2.2.1.

The equation for traveling waves $u(x, t) \equiv v(x - ct)$ becomes, after one integration:

$$c v = v^3 v_{zz} + \delta v^2 v_z^2 + \frac{1}{4}v^4, \quad (\text{C.1})$$

where $z \equiv x - ct$ and we have set one integration constant to zero. This excludes compactly supported solutions which would be too singular close to the edges of the support.

We will assume that $c < 0$, since the general case can be recovered using the symmetry $(v, c) \rightarrow (-v, -c)$. Equation (C.1) can be seen as a dynamical system in the $(v, \partial_z v)$ plane, where we have to pay special attention to the singular line $v = 0$. Therefore, we will consider the cases $v > 0$ and $v < 0$ separately. Finally,

using the translation invariance of (C.1), let us add a further boundary condition:

$$v_z(0) = 0. \tag{C.2}$$

We will see that every orbit crosses the line $v_z = 0$ at least once, so that we are not missing any solutions by imposing (C.2).

C.1 Case $v > 0$

Let us introduce a useful change of variables. We define:

$$\zeta(z) = \int_0^z v^{-\frac{1}{2}}(s) ds, \tag{C.3}$$

and denote

$$U(\zeta) \equiv v(z). \tag{C.4}$$

This change of variables is convenient because it allows to discriminate simply between compactly-supported orbits with the edge behaviour¹

$$v(z) \sim L|z - e_{\pm}|^{\frac{2}{3}}, \quad z \sim e_{\pm}, \quad L \in \mathbb{R}, \tag{C.5}$$

$$\text{(where } \text{supp}(v(z)) = [e_-, e_+]), \tag{C.6}$$

and more singular orbits. In fact, notice that

$$U_{\zeta}(\zeta) = v^{\frac{1}{2}}(z)v_z(z). \tag{C.7}$$

Due to l'Hôpital's theorem, if $v(z)$ is smooth within its support close to e_{\pm} ,

¹ As we have discussed in the rest of the thesis, the behaviour (C.5) has to be expected from traveling solutions to equations with a dispersive term of the form $u^3 u_{xxx} + \dots$

we have

$$\lim_{\substack{z \rightarrow e_{\pm} \\ z \in \text{supp}}} U_{\zeta}(\zeta(z)) = \lim_{\substack{z \rightarrow e_{\pm} \\ z \in \text{supp}}} v(z)^{\frac{1}{2}} v_z(z) = \frac{2}{3} \lim_{\substack{z \rightarrow e_{\pm} \\ z \in \text{supp}}} \frac{v(z)^{\frac{3}{2}}}{(z - e_{\pm})}. \quad (\text{C.8})$$

Therefore $v(z)$ has the behaviour (C.5) precisely if U_{ζ} remains finite as ζ approaches the endpoints, and we have

$$\lim_{\substack{z \rightarrow e_{\pm} \\ z \in \text{supp}}} U_{\zeta}(\zeta(z)) = \frac{2}{3} L^{\frac{3}{2}}. \quad (\text{C.9})$$

We refer to such solutions as “regular”, while “singular” compacton solutions will be the ones characterized by the divergence of U_{ζ} . In terms of the new variables, (C.1) can be rewritten as:

$$U \partial_{\zeta\zeta} U + \left(\delta - \frac{1}{2}\right) (\partial_{\zeta} U)^2 - c + U^3 = 0. \quad (\text{C.10})$$

It is useful to notice that the following quantity

$$G_+(U, U_{\zeta}) = \frac{1}{2} U^{2\delta-1} \left(U_{\zeta}^2 - \frac{c}{\left(\delta - \frac{1}{2}\right)} + \frac{U^3}{(\delta + 1)} \right), \quad (\text{C.11})$$

is constant along every solution of (C.10). Therefore, the orbits must lie on the level sets of $G_+(U, U_{\zeta})$. Moreover, because

$$\frac{\partial}{\partial U} G_+(U, 0) = (-c) U^{2\delta-2} (1 + U^3/(-c)) > 0, \quad (\text{C.12})$$

we have that every orbit crosses the $U_{\zeta} = 0$ axis at most once.

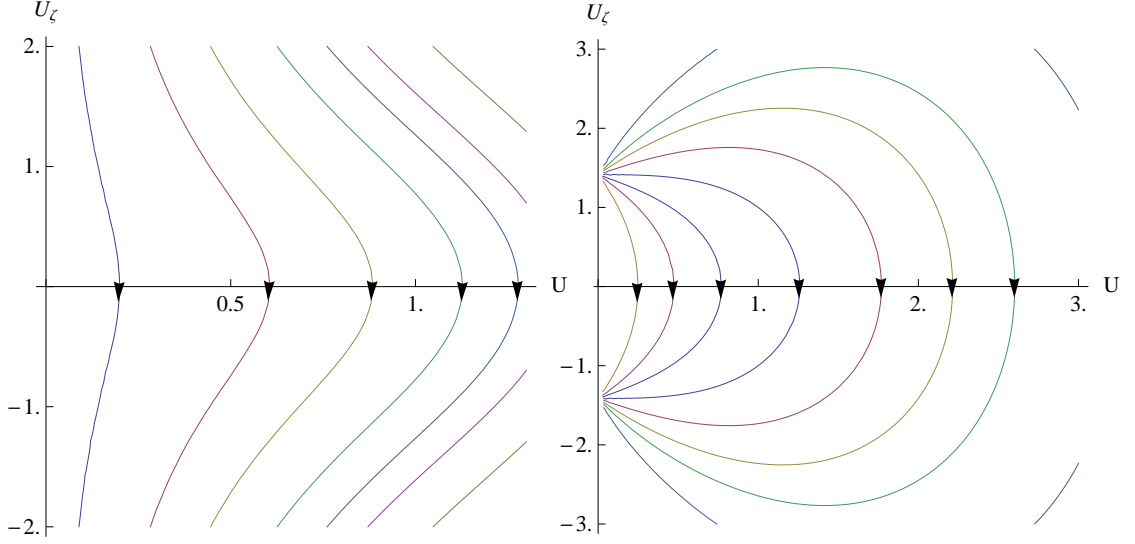


Figure C.1: Depiction of the orbits of equation (C.10) with $c = -1$, $U > 0$ for different values of δ . *Left:* $\delta = 1.5$, *Right:* $\delta = 0$.

$v > 0$ and $\delta \geq \frac{1}{2}$: singular compactons

Let us consider the case $\delta \geq \frac{1}{2}$ first. Then we have that $U_{\zeta\zeta} < -U^2 < 0$ in the whole half-plane $U > 0$. This shows that every orbit crosses the line $U_{\zeta} = 0$. Moreover, from (C.10) we also see that

$$\partial_{\zeta\zeta}U < +\frac{c}{U}, \quad (\text{C.13})$$

and this shows that every orbit flows from $(0, \infty)$ to $(0, -\infty)$ in the $(U, \partial_{\zeta}U)$ plane. The phase space is depicted in the left panel of Figure C.1. Using the previous estimates one could also show that these orbits have compact support. Because the limit (C.8) is infinite, we have found that all these orbits are more singular than (C.5).

Summarizing, we have shown that *For $\delta \geq \frac{1}{2}$, $c > 0$, all the positive solutions to (C.1) are compactly supported and the behaviour of the solutions at the edge of their support is more singular than (C.5).*

$v > 0$ and $\delta < \frac{1}{2}$: degenerate family of regular compactons

Now, suppose $\delta < \frac{1}{2}$. We consider a solution crossing the $U_\zeta = 0$ axis at $\zeta = 0$. The orbit cannot cross the $U_\zeta = 0$ axis at any other point, because of (C.12). From (C.10) we see that $U_{\zeta\zeta} < 0$ on the $U_\zeta = 0$ axis, and therefore $U_\zeta < 0$ for $\zeta > 0$ and $U_\zeta > 0$ for $\zeta < 0$. Moreover, from (C.10) we see that, as long as the solution is in the region $U_\zeta^2 < \frac{c}{\delta - \frac{1}{2}}$, $U_{\zeta\zeta}$ is strictly negative. Therefore the orbits move out of this strip in a finite “time”, and $|U_\zeta|$ is bounded from below for sufficiently large $|\zeta|$. This shows that the solution must have a maximal domain of existence $[-\zeta_*, \zeta_*]$ (where $0 < \zeta_* < \infty$ is a parameter that can depend on the orbit), and

$$\lim_{\zeta \rightarrow \pm\zeta_*} U(\zeta) = 0.$$

Requiring that $G_+(U, U_\zeta)$ remains constant in the $U \rightarrow 0$ limit, we immediately find that

$$\lim_{\zeta \rightarrow \pm\zeta_*} \partial_\zeta U(\zeta) = \sqrt{\frac{-c}{\frac{1}{2} - \delta}}. \quad (\text{C.14})$$

This case is depicted in the right panel of Figure C.1 for $\delta = 0$.

Translating this result in terms of the original variables we have found that *For $\delta < \frac{1}{2}$, $c < 0$, all the positive solutions to (C.1) are compactly supported, and they have the scaling behaviour (C.5) at the edge of their support, with*

$$L \equiv \left(\frac{9c}{4\delta - 2} \right)^{\frac{1}{3}}. \quad (\text{C.15})$$

C.2 Case $v < 0$

In the case $v < 0$, we make a change of variable similar to (C.3):

$$\zeta(z) = \int_0^z (-v)^{-\frac{1}{2}}(s) ds, \quad (\text{C.16})$$

and equation (C.1) becomes:

$$U \partial_{\zeta\zeta} U + \left(\delta - \frac{1}{2}\right)(\partial_{\zeta} U)^2 + c - U^3 = 0, \quad (\text{C.17})$$

with $U(\zeta) \equiv v(z)$. This dynamical system is characterised by the presence of a centre at $(U_c U_0, 0)$, where

$$U_c = +c^{\frac{1}{3}} < 0. \quad (\text{C.18})$$

The quantity

$$G_-(U, U_{\zeta}) = \frac{1}{2}(-U)^{2\delta-1} \left(U_{\zeta}^2 + \frac{c}{(\delta - 1/2)} - \frac{1}{(\delta + 1)} U^3 \right), \quad (\text{C.19})$$

is constant along every solution to (C.17).

$v < 0$ and $\delta > \frac{1}{2}$: unique regular compacton solution

Let us start by considering $\delta > \frac{1}{2}$. In this case, every initial condition of the form

$$U(0) = u_0, \quad \partial_{\zeta} U(0) = 0, \quad \text{with } U_c < u_0 < 0, \quad (\text{C.20})$$

defines a periodic orbit encircling the center. Let us now prove that this family of orbits has a well-defined limit as $u_0 \rightarrow 0^-$, and that this limit orbit defines a compacton solution. The limit exists because all periodic orbits are non-intersecting and are confined to a rectangle, therefore the limit exists pointwise by

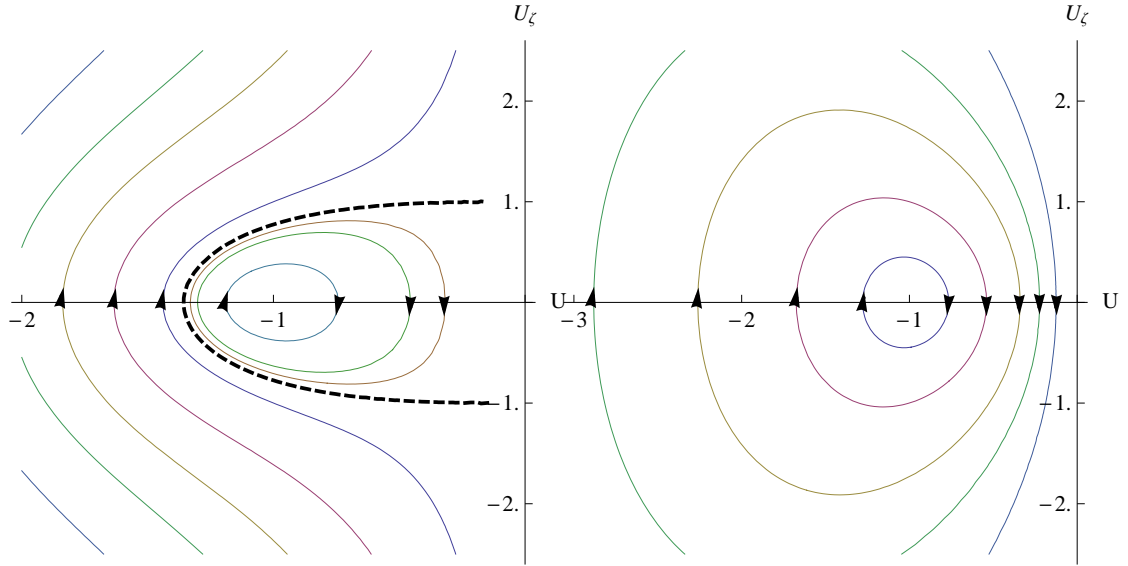


Figure C.2: The orbits of (C.10) with $c = -1$, $U < 0$, for different values of δ . *Left:* $\delta = 1.5$, *Right:* $\delta = 0$. The black dashed curve on the left is the stable compacton orbit obtained as a limit of a family of periodic orbits.

compactness. To see this notice that, for all initial conditions (C.20), $G_-(u_0, 0) < 0$, and (C.19) immediately implies $|U_\zeta| < \frac{2}{3}|L|^{\frac{3}{2}}$ (with L as in (C.15)). Moreover, let us define $U_{min} = U_{min}(u_0)$ as the lowest value of U reached along a solution defined by the initial condition (C.20). It is easy to see that $\lim_{u_0 \rightarrow 0} G_-(u_0, 0) = 0$. Evaluating this expression at the second inflection point of the orbit where $U_\zeta = 0$ and $U = U_{min}(u_0)$, we have

$$G_-(u_0, 0) = -\frac{1}{2}|U_{min}(u_0)|^{2\delta-1} \left(\frac{-c}{(\delta-1/2)} + \frac{1}{(\delta+1)}U_{min}^3(u_0) \right), \quad (\text{C.21})$$

and therefore

$$\lim_{u_0 \rightarrow 0^-} U_{min}(u_0) = -|c|^{\frac{1}{3}} \left(\frac{\delta+1}{\delta-\frac{1}{2}} \right)^{\frac{1}{3}} \equiv \bar{U}. \quad (\text{C.22})$$

This proves that the limit orbit exists and has a negative amplitude given by \bar{U} . Clearly, it must be made of two pieces: a vertical segment running from $(0, +\frac{2}{3}|L|^{\frac{3}{2}})$ to $(-\frac{2}{3}|L|^{\frac{3}{2}}, 0)$, which we can discard, and an arc connecting the

points $(0, -\frac{2}{3}|L|^{\frac{3}{2}})$ and $(0, +\frac{2}{3}|L|^{\frac{3}{2}})$, where L is given by (C.15). Therefore, this limit defines precisely a compacton solution with the edge behaviour (C.5), (C.15). The amplitude of this solution is given by \bar{U} in (C.22).

Finally, notice that all solutions defined by an initial condition of the form

$$U(0) = u', \quad \partial_\zeta U(0) = 0, \quad \text{with} \quad u' < \bar{U} < 0, \quad (\text{C.23})$$

must have $G_- > 0$, and considering (C.19) we see that they must satisfy $U_\zeta \rightarrow \pm\infty$ as $U \rightarrow 0$. Therefore by the same arguments of section C.1, we know that their edge behaviour is more singular than (C.5).

Summarizing, we have proved: *For $\delta > \frac{1}{2}$, $c < 0$, the negative solutions to (C.1) can be either periodic and smooth or compactly supported. There is a unique regular compactly supported solution with the edge behaviour (C.5), and this orbit can be seen as the limit of a family of periodic solutions as their amplitudes approach a critical value. All other compactly supported solutions have a more singular behaviour at the edge of their support.*

$v < 0$ and $\delta \leq \frac{1}{2}$: periodic solutions

Finally, in the case $\delta \leq \frac{1}{2}$, $U < 0$, the level sets $G_-(U, U_\zeta)$ are closed curves circling around the centre as shown in Figure C.2:

For $\delta \leq \frac{1}{2}$, $c < 0$, all negative solutions to (C.1) are smooth periodic orbits bounded away from zero.

References

- ABASSY, T.A., EL ZOHEIRY, H. & EL-TAWIL, M.A. (2009). A numerical study of adding an artificial dissipation term for solving the nonlinear dispersive equations $K(n, n)$. *Journal of computational and applied mathematics*, **232**, 388–401. 79
- ABLOWITZ, M.J. & SEGUR, H. (1981). *Solitons and the inverse scattering transform*, vol. 4. SIAM. 9, 103
- ABLOWITZ, M.J., RAMANI, A. & SEGUR, H. (1978). Nonlinear evolution equations and ordinary differential equations of Painlevé type. *Lettere Al Nuovo Cimento (1971–1985)*, **23**, 333–338. 1
- AMBROSE, D.M. & WRIGHT, J.D. (2010). Preservation of support and positivity for solutions of degenerate evolution equations. *Nonlinearity*, **23**, 607–620. 76, 95
- AMBROSE, D.M., SIMPSON, G., WRIGHT, J.D. & YANG, D.G. (2012). Ill-posedness of degenerate dispersive equations. *Nonlinearity*, **25**, 2655–2680. 72, 73, 76
- ANDERSON, A.G., BENDER, C.M. & MORONE, U.I. (2011). Periodic orbits for classical particles having complex energy. *Physics Letters A*, **375**, 3399–3404. 8, 24, 25, 42
- ARNOL'D, V.I. (1989). *Mathematical methods of classical mechanics*, vol. 60. Springer. 24

REFERENCES

- ARONSON, D.G. (1969). Regularity properties of flows through porous media. *SIAM Journal on Applied Mathematics*, **17**, 461–467. 65
- ARONSON, D.G. (1970a). Regularity properties of flows through porous media: A counterexample. *SIAM Journal on Applied Mathematics*, **19**, 299–307. 65
- ARONSON, D.G. (1970b). Regularity properties of flows through porous media: The interface. *Archive for Rational Mechanics and Analysis*, **37**, 1–10. 65
- ASSIS, P.E.G. & FRING, A. (2009a). From real fields to complex Calogero particles. *Journal of Physics A: Mathematical and Theoretical*, **42**, 425206. 9
- ASSIS, P.E.G. & FRING, A. (2009b). Integrable models from \mathcal{PT} -symmetric deformations. *Journal of Physics A: Mathematical and Theoretical*, **42**, 105206. 9
- BAKER, G.R., LI, X. & MORLET, A.C. (1996). Analytic structure of two 1D-transport equations with nonlocal fluxes. *Physica D: Nonlinear Phenomena*, **91**, 349–375. 51
- BARENBLATT, G.I. (1953). On a class of exact solutions of the plane one-dimensional problem of unsteady filtration into a porous medium. *Prikl. Mat. Meh*, **17**, 739–742. 65
- BENDER, C.M. (2007). Making sense of non-Hermitian Hamiltonians. *Reports on Progress in Physics*, **70**, 947. 3
- BENDER, C.M. & BOETTCHER, S. (1998). Real spectra in non-Hermitian Hamiltonians having \mathcal{PT} -symmetry. *Physical Review Letters*, **80**, 5243–5246. ix, 1, 2, 3, 4
- BENDER, C.M. & DARG, D.W. (2007). Spontaneous breaking of classical \mathcal{PT} symmetry. *Journal of mathematical physics*, **48**, 042703. 7, 8
- BENDER, C.M. & FEINBERG, J. (2008). Does the complex deformation of the Riemann equation exhibit shocks? *Journal of Physics A: Mathematical and Theoretical*, **41**, 244004. iv, 9, 43, 50, 51, 60, 126

REFERENCES

- BENDER, C.M. & HOOK, D.W. (2014). Complex classical motion in potentials with poles and turning points. *arXiv preprint arXiv:1402.3852*. 28
- BENDER, C.M. & JONES, H.F. (2011). Quantum counterpart of spontaneously broken classical \mathcal{PT} symmetry. *Journal of Physics A: Mathematical and Theoretical*, **44**, 015301. 8
- BENDER, C.M. & TURBINER, A. (1993). Analytic continuation of eigenvalue problems. *Physics Letters A*, **173**, 442–446. 3
- BENDER, C.M., BOETTCHER, S. & MEISINGER, P.N. (1999). \mathcal{PT} -symmetric quantum mechanics. *Journal of Mathematical Physics*, **40**, 2201–2229. 1, 6, 20, 22
- BENDER, C.M., CHEN, J.H., DARG, D.W. & MILTON, K.A. (2006). Classical trajectories for complex Hamiltonians. *Journal of Physics A: Mathematical and General*, **39**, 4219–4238. 7, 8, 15
- BENDER, C.M., BRODY, D.C., CHEN, J.H. & FURLAN, E. (2007). \mathcal{PT} -symmetric extension of the Korteweg–deVries equation. *Journal of Physics A: Mathematical and Theoretical*, **40**, F153–F160. 9, 11, 13
- BENDER, C.M., BRODY, D.C. & HOOK, D.W. (2008). Quantum effects in classical systems having complex energy. *Journal of Physics A: Mathematical and Theoretical*, **41**, 352003. 8
- BENDER, C.M., FEINBERG, J., HOOK, D.W. & WEIR, D.J. (2009). Chaotic systems in complex phase space. *Pramana*, **73**, 453–470. 9
- BENDER, C.M., HOOK, D.W., MEISINGER, P.N. & WANG, Q.H. (2010a). Complex correspondence principle. *Physical review letters*, **104**, 061601. 8
- BENDER, C.M., HOOK, D.W., MEISINGER, P.N. & WANG, Q.H. (2010b). Probability density in the complex plane. *Annals of Physics*, **325**, 2332–2362. 8
- BERRY, M.V. (1994). Pancharatnam, virtuoso of the Poincaré sphere: an appreciation. *Curr. Sci.*, **67**, 220–223. 4, 6

REFERENCES

- BESSIS, D. & FOURNIER, J.D. (1984). Pole condensation and the Riemann surface associated with a shock in Burgers' equation. *Journal de Physique Lettres*, **45**, 833–841. 45
- BIRNIR, B. (1986). Singularities of the complex Korteweg-deVries flows. *Communications on pure and applied mathematics*, **39**, 283–305. 10
- BONA, J.L. & WEISSLER, F.B. (2009). Pole dynamics of interacting solitons and blowup of complex-valued solutions of KdV. *Nonlinearity*, **22**, 311. 10, 40
- CALOGERO, F., GÓMEZ-ULLATE, D., SANTINI, P.M. & SOMMACAL, M. (2005). The transition from regular to irregular motions, explained as travel on Riemann surfaces. *Journal of Physics A: Mathematical and General*, **38**, 8873. 1
- CAMASSA, R. & HOLM, D.D. (1993). An integrable shallow water equation with peaked solitons. *Physical Review Letters*, **71**, 1661–1664. 56, 62, 97
- CAMASSA, R., HOLM, D.D. & HYMAN, J.M. (1994). A new integrable shallow water equation. *Advances in Applied Mechanics*, **31**, 1–33. 95
- CARDENAS, A., MIHAILA, B., COOPER, F. & SAXENA, A. (2011). Properties of compacton-antcompacton collisions. *Physical Review E*, **83**, 066705. 75
- CAVAGLIÀ, A. & FRING, A. (2012). \mathcal{PT} -symmetrically deformed shock waves. *Journal of Physics A: Mathematical and Theoretical*, **45**, 444010. iii, iv, 43, 53, 126
- CAVAGLIÀ, A., FRING, A. & BAGCHI, B. (2011). \mathcal{PT} -symmetry breaking in complex nonlinear wave equations and their deformations. *Journal of Physics A: Mathematical and Theoretical*, **44**, 325201. iii, iv, 2, 12, 33, 41, 51, 126
- CHAE, D., CÓRDOBA, A., CÓRDOBA, D. & FONTELOS, M.A. (2005). Finite time singularities in a 1D model of the quasi-geostrophic equation. *Advances in Mathematics*, **194**, 203–223. 51
- CHERTOCK, A. & LEVY, D. (2001). Particle methods for dispersive equations. *Journal of Computational Physics*, **171**, 708–730. 78, 79

REFERENCES

- CLARKSON, P.A., FOKAS, A.S. & ABLOWITZ, M.J. (1989). Hodograph transformations of linearizable partial differential equations. *SIAM Journal on Applied Mathematics*, **49**, 1188–1209. 98, 99, 100, 101, 102
- COOPER, F., SHEPARD, H. & SODANO, P. (1993). Solitary waves in a class of generalized Korteweg-deVries equations. *Physical Review E*, **48**, 4027–4032. 74, 100
- COOPER, F., HYMAN, J.M. & KHARE, A. (2001). Compacton solutions in a class of generalized fifth-order Korteweg–de Vries equations. *Physical Review E-Statistical, Nonlinear and Soft Matter Physics*, **64**, 026608_1–026608_13. 74
- CURTRIGHT, T.L. & FAIRLIE, D.B. (2008). Euler incognito. *Journal of Physics A: Mathematical and Theoretical*, **43**, 244009. 50
- DARCY, H. (1856). *Les fontaines publiques de la ville de Dijon*. V. Dalmont, Paris. 61, 63
- DEFRUTOS, J., LÓPEZ-MARCOS, M.A. & SANZ-SERNA, J.M. (1995). A finite difference scheme for the $K(2, 2)$ compacton equation. *Journal of Computational Physics*, **120**, 248–252. 72, 73, 74, 76, 77, 78, 94, 95, 131, 133
- DEGASPERIS, A. & PROCESI, M. (1999). Asymptotic integrability. *Symmetry and perturbation theory*, **7**, 23–37. 97
- DEY, B. & KHARE, A. (1998). Stability of compacton solutions. *Physical Review E*, **58**, R2741. 108
- DEY, S. & FRING, A. (2013). Bohmian quantum trajectories from coherent states. *Physical Review A*, **88**, 022116. 7
- DIEUDONNÉ, J. (1961). Quasi-Hermitian operators. *Proc. Internat. Sympos. Linear Spaces (Jerusalem, 1960)*, Pergamon, Oxford, 115–122. 6
- DOREY, P., DUNNING, C. & TATEO, R. (2001). Spectral equivalences, Bethe ansatz equations, and reality properties in \mathcal{PT} -symmetric quantum mechanics. *Journal of Physics A*, **34**, 5679–5704. 4

REFERENCES

- DOREY, P., DUNNING, C. & TATEO, R. (2007). The ODE/IM correspondence. *Journal of Physics A: Mathematical and Theoretical*, **40**, R205. 4
- EVANS, L.C. (2010). *Partial Differential Equations*. Graduate studies in mathematics, American Mathematical Society. 62, 72
- FAGOTTI, M., BONATI, C., LOGOTETA, D., MARCONCINI, P. & MACUCCI, M. (2011). Armchair graphene nanoribbons: \mathcal{PT} -symmetry breaking and exceptional points without dissipation. *Physical Review B*, **83**, 241406. 6
- FISHER, M.E. (1978). Yang-Lee edge singularity and ϕ^3 field theory. *Physical Review Letters*, **40**, 1610. 2
- FOKAS, A.S. (1995). On a class of physically important integrable equations. *Physica D: Nonlinear Phenomena*, **87**, 145–150. 112
- FOKAS, A.S., OLVER, P.J. & ROSENAU, P. (1997). A plethora of integrable bi-Hamiltonian equations. *Algebraic Aspects of Integrable Systems: In Memory of Irene Dorfman, A.S. Fokas and I.M. Gel'fand, eds., Progress in Nonlinear Differential Equations*, **26**, 93–101. 98
- FRING, A. (2007). \mathcal{PT} -symmetric deformations of the Korteweg–de Vries equation. *Journal of Physics A: Mathematical and Theoretical*, **40**, 4215. 9, 12, 31, 35, 42
- FRING, A. & SMITH, M. (2010). Antilinear deformations of Coxeter groups, an application to Calogero models. *Journal of Physics A: Mathematical and Theoretical*, **43**, 325201. 9
- FRING, A. & ZNOJIL, M. (2008). \mathcal{PT} -symmetric deformations of Calogero models. *Journal of Physics A: Mathematical and Theoretical*, **41**, 194010. 9
- GARDNER, C.S., GREENE, J.M., KRUSKAL, M.D. & MIURA, R.M. (1967). Method for solving the Korteweg-deVries equation. *Physical Review Letters*, **19**, 1095. 39, 103

REFERENCES

- GARRALÓN, J., RUS, F. & VILLATORO, F.R. (2013). Removing trailing tails and delays induced by artificial dissipation in Padè numerical schemes for stable compacton collisions. *Applied Mathematics and Computation*, **220**, 185–192. 79
- GÜNTHER, U., ROTTER, I. & SAMSONOV, B.F. (2007). Projective Hilbert space structures at exceptional points. *Journal of Physics A: Mathematical and Theoretical*, **40**, 8815. 6
- HARTMAN, P. (1964). Ordinary differential equations. *Classics in Applied Mathematics*, **38**. 130
- HATANO, N. & NELSON, D.R. (1996). Localization transitions in non-Hermitian quantum mechanics. *Physical Review Letters*, **77**, 570. 6
- HEISS, W.D. (2012). The physics of exceptional points. *Journal of Physics A: Mathematical and Theoretical*, **45**, 444016. 4, 6
- HOLM, D.D. & STALEY, M.F. (2003). Nonlinear balance and exchange of stability in dynamics of solitons, peakons, ramps/cliffs and leftons in a $1+1$ nonlinear evolutionary PDE. *Physics Letters A*, **308**, 437–444. 98, 125
- HONE, A.N.W. (2009). Painlevé tests, singularity structure and integrability. In *Integrability*, 245–277. 99
- HONE, A.N.W. & LAFORTUNE, S. (2014). Stability of stationary solutions for nonintegrable peakon equations. *Physica D Nonlinear Phenomena*, **269**, 28–36. 98, 125
- HONE, A.N.W. & WANG, J.P. (2008). Integrable peakon equations with cubic nonlinearity. *Journal of Physics A: Mathematical and Theoretical*, **41**, 372002. 112
- ISERLES, A. (2009). *A first course in the numerical analysis of differential equations*. 44, Cambridge University Press. 78
- ISMAIL, M.S. & TAHA, T.R. (1998). A numerical study of compactons. *Mathematics and Computers in Simulation*, **47**, 519–530. 74, 78

REFERENCES

- KALASHNIKOV, A.S. (1967). Appearance of singularities in a solution of a non-stationary filtration equation. *Zh. Vychisl. Mat. Mat. Fiz*, **2**, 440–444. 65
- KLAIMAN, S., GÜNTHER, U. & MOISEYEV, N. (2008). Visualization of branch points in \mathcal{PT} -symmetric waveguides. *Physical review letters*, **101**, 080402. 6
- KNERR, B.F. (1977). The porous medium equation in one dimension. *Transactions of the American Mathematical Society*, **234**, 381–415. 65
- KORTEWEG, D. & DE VRIES, G. (1895). On the change of a form of long waves advancing in a rectangular canal and a new type of long stationary waves. *Phil. Mag., 5th Series*, 422–443. 9
- KOTTOS, T. (2010). Optical physics: Broken symmetry makes light work. *Nature Physics*, **6**, 166–167. 6
- KOWALEVSKI, S. (1889). Sur le probleme de la rotation d’un corps solide autour d’un point fixe. *Acta mathematica*, **12**, 177–232. 1
- KRUSKAL, M.D., JOSHI, N. & HALBURD, R. (1997). Analytic and asymptotic methods for nonlinear singularity analysis: a review and extensions of tests for the Painlevé property. In *Integrability of nonlinear systems*, 171–205, Springer. 99
- LEIBENZON, L.S. (1930). *The motion of a gas in a porous medium*. Complete Works, Vol. 2, Acad. Sciences URSS, Moscow, (Russian). 63
- LEVI, D. (1994). Levi-Civita theory for irrotational water waves in a one-dimensional channel and the complex Korteweg-de Vries equation. *Theoretical and Mathematical Physics*, **99**, 705–709. 10
- LEVI, D. & SANIELEVICI, M. (1996). Irrotational water waves and the complex Korteweg-de Vries equation. *Physica D: Nonlinear Phenomena*, **98**, 510–514. 10
- LEVY, D., SHU, C.W. & YAN, J. (2004). Local discontinuous Galerkin methods for nonlinear dispersive equations. *Journal of Computational Physics*, **196**, 751–772. 78, 79, 83, 94, 95

REFERENCES

- LI, Y.A. & OLVER, P.J. (1997). Convergence of solitary-wave solutions in a perturbed bi-Hamiltonian dynamical system: I. Compactons and peakons. *Discrete and Continuous Dynamical Systems*, **3**, 419–432. 72
- LI, Y.A. & OLVER, P.J. (1998). Convergence of solitary-wave solutions in a perturbed bi-Hamiltonian dynamical system: II. Complex analytic behavior. *Discrete and Continuous Dynamical systems*, **4**, 159–191. 72
- LI, Y.A., OLVER, P.J. & ROSENAU, P. (1999). Non-analytic solutions of non-linear wave models. *Chapman and Hall CRC Research Notes in Mathematics*, 129–146. 62, 72
- MAGRI, F. (1978). A simple model of the integrable Hamiltonian equation. *Journal of Mathematical Physics*, **19**, 1156–1162. 10, 111, 112
- MANDAL, B.P. & MAHAJAN, S.S. (2013). Complex classical mechanics of a QES potential. *arXiv preprint arXiv:1312.0757*. 7
- MATYTSIN, A. (1994). On the large-N limit of the Itzykson-Zuber integral. *Nuclear Physics B*, **411**, 805–820. 51
- MIHAILA, B., CARDENAS, A., COOPER, F. & SAXENA, A. (2010a). Stability and dynamical properties of Cooper-Shepard-Sodano compactons. *Physical Review E*, **82**, 066702. 74, 75, 77, 78, 131, 132
- MIHAILA, B., CARDENAS, A., COOPER, F. & SAXENA, A. (2010b). Stability and dynamical properties of Rosenau–Hyman compactons using Padé approximants. *Physical Review E*, **81**, 056708. 74, 77, 78, 86, 94, 95
- MIKHAILOV, A.V. & SOKOLOV, V.V. (2009). Symmetries of differential equations and the problem of integrability. In *Integrability*, 19–88, Springer. 98
- MIKHAILOV, A.V., SHABAT, A.B. & YAMILOV, R.I. (1987). The symmetry approach to the classification of non-linear equations. Complete lists of integrable systems. *Russian Mathematical Surveys*, **42**, 1–63. 98

REFERENCES

- MIKHAILOV, A.V., SHABAT, A.V. & SOKOLOV, V.V. (1991). The symmetry approach to classification of integrable equations. In *What is integrability?*, 115–184. 99
- MILLICAN-SLATER, A. (2004). *Aspects of \mathcal{PT} -symmetric quantum mechanics*. Ph.D. thesis, Durham University. 7
- MOISEYEV, N. (2011). *Non-Hermitian quantum mechanics*. Cambridge University Press Cambridge. 5
- MOSTAFAZADEH, A. (2002). Pseudo-Hermiticity versus \mathcal{PT} symmetry: the necessary condition for the reality of the spectrum of a non-Hermitian Hamiltonian. *Journal of Mathematical Physics*, **43**, 205. 6
- MUSKAT, M. (1937). *The flow of homogeneous fluids through porous media*. McGraw-Hill. 63
- OLEINIK, O.A., KALASHNIKOV, A.S. & JUJ-LIN, C. (1958). The Cauchy problem and boundary problems for equations of the type of non-stationary filtration. *Izvestiya Rossiiskoi Akademii Nauk. Seriya Matematicheskaya*, **22**, 667–704. 65
- OLVER, P. & ROSENAU, P. (1996). Tri-Hamiltonian duality between solitons and solitary-wave solutions having compact support. *Physical Review E*, **53**, 1900–1906. 98, 111, 112
- OLVER, P.J. (2000). *Applications of Lie groups to differential equations*, vol. 107 of *Graduate Texts in Mathematics*. Springer. 10
- PRESS, W.H., TEUKOLSKY, S.A., VETTERLING, W.T. & FLANNERY, B.P. (1990). *Numerical recipes*. Cambridge University Press. 78, 134
- QIAO, Z. (2006). A new integrable equation with cuspons and W/M-shape-peaks solitons. *Journal of mathematical physics*, **47**, 112701–112900. 112
- ROSENAU, P. (1996). On solitons, compactons, and Lagrange maps. *Physics Letters A*, **211**, 265–275. iv, 97, 98, 102, 103, 105, 107, 126

REFERENCES

- ROSENAU, P. (2005). What is a compacton? *Notices of the AMS*, **82**, 738–739. 68
- ROSENAU, P. (2006). On a model equation of traveling and stationary compactons. *Physics Letters A*, **356**, 44–50. iv, 97, 98, 107, 108, 111, 123, 124, 127
- ROSENAU, P. & HYMAN, J.M. (1993). Compactons: Solitons with finite wavelength. *Physical Review Letters*, **70**, 564–567. iv, 61, 68, 73, 75, 77, 78, 86, 94, 95, 97
- RUS, F. & VILLATORO, F.R. (2007a). Padè numerical method for the Rosenau-Hyman compacton equation. *Mathematics and Computers in Simulation*, **76**, 188–192. 77, 78, 94
- RUS, F. & VILLATORO, F.R. (2007b). Self-similar radiation from numerical Rosenau-Hyman compactons. *Journal of Computational Physics*, **227**, 440–454. 79
- RÜTER, C.E., MAKRIS, K.G., EL-GANAINY, R., CHRISTODOULIDES, D.N., SEGEV, M. & KIP, D. (2010). Observation of parity–time symmetry in optics. *Nature Physics*, **6**, 192–195. 6
- SAKOVICH, S.Y. (2003). On integrability of one third-order nonlinear evolution equation. *Physics Letters A*, **314**, 232–238. 98, 104
- SAUCEZ, P., VANDE WOUWER, A., SCHIESSER, W.E. & ZEGELING, P. (2004). Method of lines study of nonlinear dispersive waves. *Journal of Computational and Applied Mathematics*, **168**, 413–423. 78, 79
- SCHOLTZ, F., GEYER, H. & HAHNE, F. (1992). Quasi-Hermitian operators in quantum mechanics and the variational principle. *Annals of Physics*, **213**, 74–101. 6
- SIEGL, P. & KREJČIŘÍK, D. (2012). On the metric operator for the imaginary cubic oscillator. *Physical Review D*, **86**, 121702. 6

REFERENCES

- SIMPSON, G., SPIEGELMAN, M. & WEINSTEIN, M.I. (2007). Degenerate dispersive equations arising in the study of magma dynamics. *Nonlinearity*, **20**, 21. 71
- SVINOLUPOV, S.I. & SOKOLOV, V.V. (1982). Evolution equations with nontrivial conservative laws. *Functional Analysis and Its Applications*, **16**, 317–319. 99
- SVINOLUPOV, S.I., SOKOLOV, V.V. & YAMILOV, R.I. (1983). Bäcklund transformations for integrable evolution equations. In *Soviet Math. Dokl*, vol. 28, 165–168. 99
- TAO, T. (2009). Why are solitons stable? *Bulletin of the American Mathematical Society*, **46**, 1–33. 69, 107, 108
- UZDIN, R., MAILYBAEV, A. & MOISEYEV, N. (2011). On the observability and asymmetry of adiabatic state flips generated by exceptional points. *Journal of Physics A: Mathematical and Theoretical*, **44**, 435302. 6
- VÁZQUEZ, J.L. (2006). *The Porous Medium Equation: Mathematical Theory*. Oxford University Press. 64, 65
- VODOVA, J. (2013). A complete list of conservation laws for non-integrable compacton equations of $K(m, m)$ type. *Nonlinearity*, **26**, 1900. 74
- WHITHAM, G.B. (2011). *Linear and nonlinear waves*, vol. 42. John Wiley & Sons. 49
- WIGNER, E.P. (1960). Normal form of antiunitary operators. *Journal of Mathematical Physics*, **1**, 409. 5
- WRIGHT, J.D. & AMBROSE, D.M. (2012). Dispersion vs. anti-diffusion: well-posedness in variable coefficient and quasilinear equations of KdV-type. *arXiv preprint arXiv:1205.2710*. 76, 95